

# NIKA2 research note

## NIKA2 COMMISSIONING RESULTS V1.0

NIKA2 team  
*NIKA2 collaboration*  
June 20, 2018

## Contents

<b>1</b>	<b>Introduction</b>	<b>5</b>
1.1	Commissioning goals . . . . .	5
1.2	Commissioning runs . . . . .	5
<b>2</b>	<b>Bandpasses</b>	<b>7</b>
<b>3</b>	<b>Opacity derivation</b>	<b>11</b>
3.1	Methodology . . . . .	11
3.2	Opacity measurement consistency tests . . . . .	11
<b>4</b>	<b>Focal Plane Reconstruction</b>	<b>22</b>
4.1	Methodology . . . . .	22
4.2	Average Focal Plane Reconstruction . . . . .	24
4.3	FOV grid distortion . . . . .	28
<b>5</b>	<b>Pointing accuracy</b>	<b>30</b>
<b>6</b>	<b>Beam pattern</b>	<b>32</b>
6.1	Optimal focus . . . . .	32
6.1.1	Focus estimation . . . . .	32
6.1.2	Focus consistency between arrays . . . . .	32
6.1.3	Reconstruction of the focus surfaces . . . . .	32
6.1.4	Constraints on the X and Y foci . . . . .	35
6.2	Full beam pattern . . . . .	39
6.2.1	Data sets . . . . .	39
6.2.2	Deep beam maps . . . . .	40
6.2.3	Beam profile . . . . .	42
6.3	Main beam . . . . .	42
6.3.1	Sidelobe-masked Profile-based analysis . . . . .	42
6.3.2	Sidelobe-masked Map-based analysis . . . . .	43
6.3.3	FWHM distribution across the FoV . . . . .	44
6.4	Beam efficiency . . . . .	44

6.5	Stability of the beam pattern . . . . .	44
6.5.1	Individual scan beam profiles . . . . .	44
6.5.2	Main beam FWHM stability . . . . .	45
<b>7</b>	<b>Calibration</b>	<b>51</b>
7.1	NIKA2 Photometric System . . . . .	51
7.1.1	Response of a detector to astronomical source . . . . .	51
7.1.2	Effect of the atmosphere . . . . .	52
7.1.3	Beammap of a calibrator . . . . .	54
7.1.4	Calibration in $\text{FWHM}_0$ beam . . . . .	54
7.1.5	Color correction for point sources measured with fixed gaussian fit . . . . .	55
7.1.6	Calibration for aperture photometry . . . . .	56
7.1.7	Calibration in surface brightness . . . . .	56
7.2	Reference flux densities of the calibrators . . . . .	56
7.2.1	Uranus and Neptune . . . . .	56
7.2.2	Mars . . . . .	57
7.2.3	Secondary calibrators . . . . .	57
7.3	Aperture photometry . . . . .	59
7.4	Determination of the solid angle of the total beam with Uranus and Neptune : . .	61
7.5	Stability of calibration with the primary calibrators Uranus and Neptune . . . . .	62
7.6	Calibration of the secondary calibrators MWC349A, NGC7027 and CRL2688 . . . . .	71
7.7	Tentative gain-elevation curve . . . . .	73
7.8	Calibration stability across the run . . . . .	73
7.9	Flat fielding: calibration stability across the FOV . . . . .	73
<b>8</b>	<b>Noise description: TOI and maps</b>	<b>85</b>
8.1	Dark detectors at 1 mm . . . . .	85
8.2	Dark tests . . . . .	86
<b>9</b>	<b>Detector-Detector correlation matrix</b>	<b>86</b>
9.1	RMS of the noise . . . . .	87
9.2	Discussion . . . . .	87
<b>10</b>	<b>Sensitivities</b>	<b>88</b>
10.1	Observations . . . . .	88
10.1.1	Time of integration from the density of samples . . . . .	88
10.1.2	Time of integration from the matrix footprint . . . . .	89
10.1.3	Time of integration from the flux estimator . . . . .	90
10.2	History and confusions . . . . .	90
10.3	Data processing . . . . .	90
10.4	NEFD Methods 1 and 2: deep integration . . . . .	91
<b>11</b>	<b>Total effective error budget</b>	<b>93</b>
11.1	Systematic impact of effective beam corrections . . . . .	93
11.2	Systematic impact of opacity correction . . . . .	94
<b>12</b>	<b>Summary of performance</b>	<b>108</b>

<b>A Synchronization with the telescope</b>	<b>110</b>
<b>B Reference to technical documentation</b>	<b>110</b>
B.1 Consortium-lead documentation . . . . .	110
B.2 IRAM-lead documentation . . . . .	110

### **Abstract**

This notes describe the main results of the NIKA2 commissioning campaigns.

# 1 Introduction

## 1.1 Commissioning goals

The main goal of the NIKA2 commissioning runs, described below, is to characterize the instrument and check its performance with respect to the specifications described in Table 1. We also characterize the performance stability against various observing conditions and assess the methods and the precision with which the performance parameter are measured.

Reference Wavelength [mm]	1.2	2.0
Reference Frequency [GHz]	260	150
FOV diameter [arcmin]	5 (6.5)	5 (6.5)
Pixel size in beam sampling unit [ $F\lambda$ ]	0.9 (0.6)	0.9 (0.6)
FWHM [arcsec]	12 (10)	18 (16)
Fraction of valid detectors [%]	50 (90)	50 (90)
NEFD <sup>a</sup> [ $\text{mJy} \cdot \text{s}^{1/2}/\text{beam}$ ]	30 (15)	20 (10)
NEFD [ $\text{mJy} \cdot \text{s}^{1/2}/\text{beam}$ ] goal on 90% of the pixels	15	10
NEFD [ $\text{mJy} \cdot \text{s}^{1/2}/\text{beam}$ ] specification on 50% of the pixels	30	20

<sup>(a)</sup> NEFD in typical IRAM good sky opacity condition: 2 mm pwv, 60° elevation

Table 1: Main characteristics defining the expected performances of NIKA2. Each parameter is associated with two values: the first one indicates the *specifications*, i.e. the requirements to be met by the instrument, while the second bracketed one gives the *goals*, i. e. the values targeted by the collaboration.

## 1.2 Commissioning runs

We had 10 commissioning runs for NIKA2 as described in Table 2.

RUN	NIKA Run	Starting date	End date	General comments
N2R1	13	29-October-2015	10-November-2015	Not full instrumentation
N2R2	14	24-November-2015	02-December-2015	13 NIKEL boards working
N2R3	15	12-January-2016	01-February-2016	20 NIKEL boards
N2R4	16	1-March-2016	15-March-2016	
Dark run	17	4-May-2016	4-May-2016	Dark tests with N2R4 conditions
N2R5	18	16-September-2016	11-October-2016	New dichroic, corrugated lenses, new array 2 mm, new electronics
N2R6	19	25-October-2016	1-November-2016	
N2R7	20	6-December-2016	13-December-2016	Test external calibrator
N2R8	21	9-January-2017	13-January-2017	Replace array 1 lens by smooth one, adjust the alignment of internal optics
		24-January-2017	25-January-2017	Tests on the sky
N2R9	22	21-February-2017	28-February-2017	
N2R10	23	18-April-2017	25-April-2017	End of commissioning phase 1, Science verification
N2R11	24	8-June-2017	13-June-2017	polarization commissioning

Table 2: Commissioning campaigns, dates and general comments.

## 2 Bandpasses

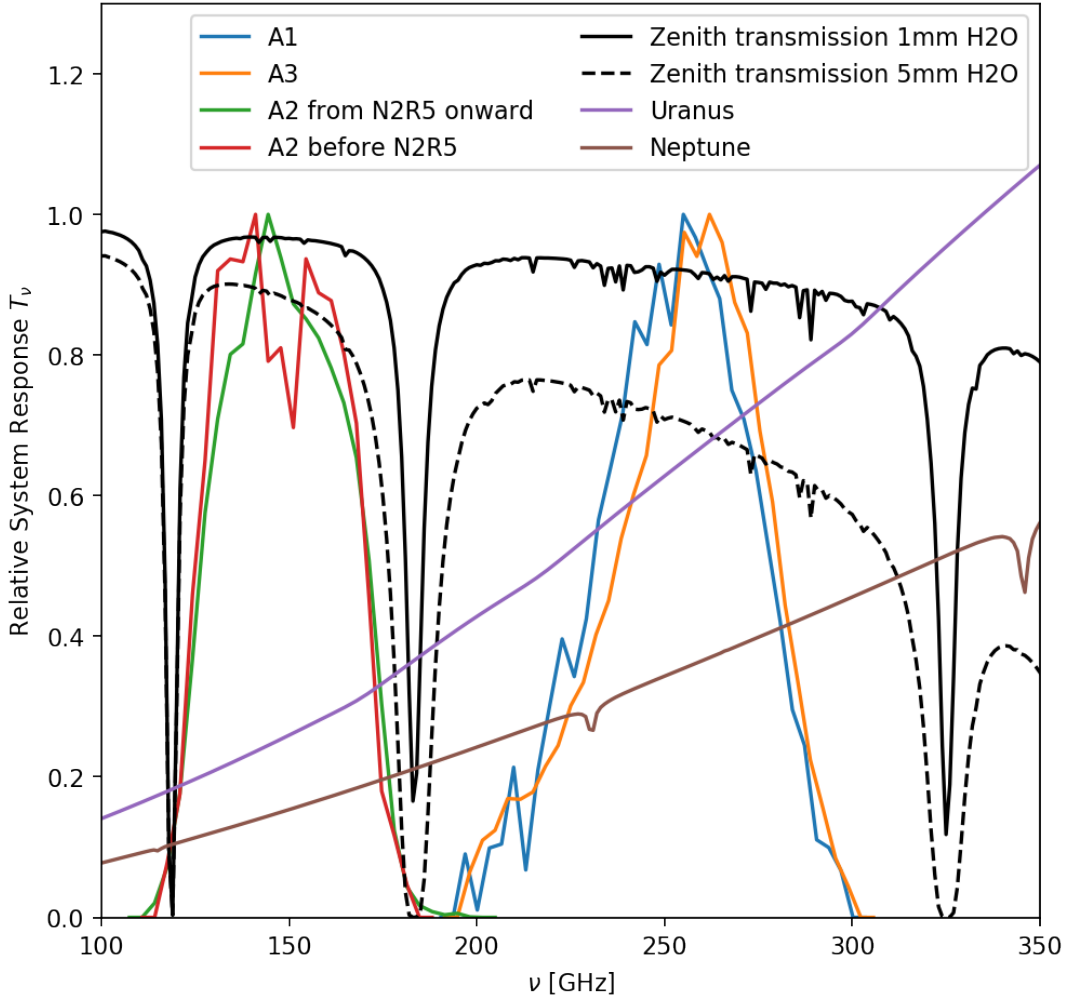


Figure 1: Relative system response of the three NIKA2 arrays as a function of frequency. For illustration we also plot atmospheric transmission obtained with the ATM model [1] for different values of precipitable water vapor. The spectra of ESA4 model of Uranus and ESA5 model of Neptune [10] in the frequency range are overplotted with arbitrary normalization. **FM: please provide Ref. for ATM, ESA4 and ESA5- DONE**

NIKA2 is a millimeter camera able to simultaneously image a field-of-view of 6.5arcmin at 150 and 260 GHz, with polarimetric capabilities at 260 GHz using KIDS. A 30-centimeters diameter air-gap dichroic splits the 150 GHz (reflection) from the 260 GHz (transmission) beams. A grid polarizer ensures then the separation of the two linear polarisations on the 260 GHz channel. There are therefore three KIDS array in NIKA2, one at 2mm, two at 1mm.

The 2mm array (150 GHz) consist of 616 pixels (KIDS), disposed to cover a circle with a 78 mm diameter. Each pixel has a size of  $2.82.8\text{mm}^2$ . This is the maximum pixel size that can be adopted without significantly degrading the telescope resolution, as it corresponds roughly to a

$1F\lambda$  sampling of the focal plane. The array is labelled A2 in all the following.

At 1mm, there are two arrays, labelled A1 and A3, consisting of 1140 KIDS with a size of  $22mm^2$  to ensure a comparable  $1F\lambda$  sampling.

Further technical details on the NIKA2 instrument can be found in the technical paper [REF !](#)

The NIKA2 spectral bands were measured in the laboratory using a Martin-Puplett interferometer built in-house [13]. Both arrays and filter bands were considered in the measurements. These were obtained from the difference of two black bodies, hence they include a  $\nu^2$  Rayleigh-Jeans (RJ) spectral term. Figure 1 shows the relative spectral response for the three arrays (corrected of the RJ term). Notice that array A2 was replaced by a new one in N2R5 and that the spectral transmissions are not the same (green and red lines in the figure).

The two arrays operating at 260 GHz, mapping different polarisations, exhibit a slightly different spectral behaviour probably as can be seen on figure 1. This may be explained by a tiny difference in the silicon wafer and/or Aluminium film thicknesses. For instance, the observed shift of the peak frequency, 265 GHz for the V (A1) array versus 258 GHz for the H one (A3), can be explained by about 5 microns change in the substrate thickness. Hereafter, the peak frequencies are referred to as reference frequencies (150 and 260 GHz) to which correspond the reference wavelength (2.0 and 1.15 mm), see tab. 20.

**FM:V (A1) array is not defined. A short description of the instrument would be useful. - DONE**

The total system response is the multiplication of the atmospheric transmission with the relative system response. To derive the atmospheric transmission, we use GILDAS ATM 2009 model [1] [REF - DONE](#), computed for the IRAM 30-m telescope, with so called *midlatwinter* conditions. We select in the model grid an atmosphere with  $T = 268.3$  K and a pressure of 703.5 hPa. The effective frequency of the passband is defined by:

$$\nu_{eff}(\sec \delta, mm_{H_2O}) = \frac{\int_0^{+\infty} S_\nu T_\nu(\sec \delta, mm_{H_2O}) \nu d\nu}{\int_0^{+\infty} S_\nu T_\nu d\nu} \quad (1)$$

**FM : in section 3, we use  $\delta$  for the elevation. I think we should stick to a single convention. - DONE**

where  $T_\nu$  is the total system response, normalized between 0. and 1. (i.e. a relative response as a function of the frequency), hereafter referred to as RSR (Relative System Response),  $S_\nu$  is the source spectrum. Table 3 list this effective frequency, computed for Uranus spectrum (ESA4 model, [10]), for different atmospheric water vapor contents and different elevations. Table 3 also list the bandwidth, defined as:

$$\Delta\nu = \int_0^{+\infty} \frac{T_\nu}{Max(T_\nu)} d\nu \quad (2)$$

where the  $Max(T_\nu)$  ensure the RSR span the whole 0.0 to 1.0 range.

**FM: RSR is not defined. - Done**

**FM: well, it means this is the normalized system response... i think it would be better than ensure the RSR span the whole 0.0 to 1.0 range.**

**: Some of the files I have seen are not normalized to 1.0... better safe than sorry.**

From Table 3, we see that the 2 mm band is somewhat sensitive to the atmospheric conditions, especially at low elevation. Note that these effective frequencies are *not* the reference frequencies

Water vapor	Elevation	1 mm (H)		1 mm (V)		2 mm	
		$\nu_{eff}$ (GHz)	$\Delta\nu$ (GHz)	$\nu_{eff}$ (GHz)	$\Delta\nu$ (GHz)	$\nu_{eff}$ (GHz)	$\Delta\nu$ (GHz)
No atmosphere		254.71	49.21	257.39	48.05	150.93	40.72
$1 \text{ mm H}_2\text{O} \rightarrow \tau_{225} = 0.067$	90 deg	254.46	48.72	257.12	47.95	150.93	39.71
	60 deg	254.42	48.68	257.08	47.93	150.92	39.60
	40 deg	254.33	48.57	256.98	47.89	150.88	39.32
	20 deg	254.00	48.21	256.62	47.77	150.75	38.45
$2 \text{ mm H}_2\text{O} \rightarrow \tau_{225} = 0.120$	90 deg	254.26	48.74	256.91	48.06	150.64	39.34
	60 deg	254.20	48.70	256.84	48.07	150.60	39.19
	40 deg	254.02	48.60	256.65	48.08	150.48	38.80
	20 deg	253.43	48.30	256.01	47.93	150.13	37.62
$3 \text{ mm H}_2\text{O} \rightarrow \tau_{225} = 0.173$	90 deg	254.06	48.76	256.70	48.19	150.39	39.03
	60 deg	253.97	48.73	256.60	48.21	150.32	38.84
	40 deg	253.71	48.65	256.33	48.28	150.14	38.35
	20 deg	252.86	48.41	255.40	47.86	149.60	36.94
$5 \text{ mm H}_2\text{O} \rightarrow \tau_{225} = 0.278$	90 deg	253.67	48.82	256.28	48.45	149.96	38.47
	60 deg	253.51	48.81	256.11	48.44	149.84	38.22
	40 deg	253.10	48.77	255.68	48.26	149.54	37.58
	20 deg	251.74	48.67	254.20	47.75	148.68	35.82
$8 \text{ mm H}_2\text{O} \rightarrow \tau_{225} = 0.437$	90 deg	253.08	48.94	255.66	48.42	149.38	37.76
	60 deg	252.84	48.93	255.39	48.35	149.20	37.42
	40 deg	252.21	48.94	254.71	48.16	148.77	36.64
	20 deg	250.12	49.38	252.43	47.91	147.52	34.57
$10 \text{ mm H}_2\text{O} \rightarrow \tau_{225} = 0.542$	90 deg	252.70	49.00	255.24	48.38	149.04	37.34
	60 deg	252.39	49.01	254.92	48.29	148.82	36.97
	40 deg	251.62	49.11	254.08	48.13	148.31	36.12
	20 deg	249.07	49.75	251.28	48.24	146.85	33.93

Table 3: Effective frequencies (for Uranus) and bandwidth of the NIKA2 bands for various atmospheric conditions and elevation.

for the band, respectively 150 GHz and 260 GHz for the A2 and A1, A3 arrays. These reference frequencies are chosen arbitrarily to define NIKA2 photometric system as will be discussed in section 7.1.7.

**FM: we should link this discussion with the so called central frequency quoted in table 13 as none of these values are in agreement (even no atmosphere and IRAM standard conditions). - DONE**

**Can we be more specific about what was computed next ? Is it the opacity weighted by the band ? Or the resultant opacity ?**

**Still to be done.**

Using the NIKA2 bandpasses for N2R9, we can integrate the ATM atmospheric model to compute the expected ratio between the atmospheric opacity of the two NIKA2 channels. Figure 2 shows the atmospheric opacity ratio of the 2 and 1 mm channels as a function of the

opacity for the 1 mm one.

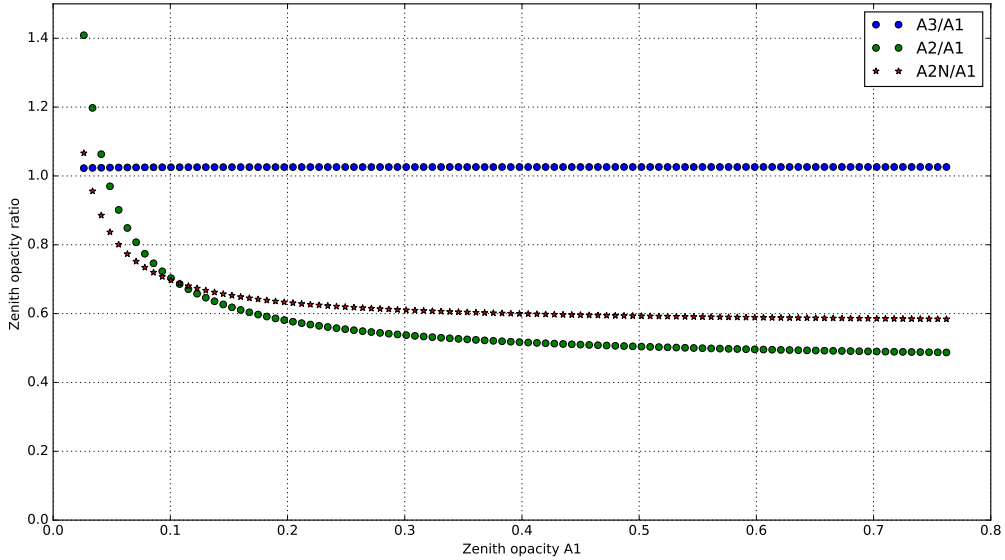


Figure 2: Expected atmospheric opacity ratio of the 2 and 1 mm channels as function of the opacity at 1 mm. FM: what is A2N/A1 ? FM: why is A3/A1=1 ?

FM: why the NIKA2 bandpasses for N2R9 ? From fig. 1 it seems there are bandpasses before R5 and after R5. i don't understand

FM: conclusion needed regarding Figure 2. so what ?

FM: it seems to me that Figure 2 would be better in sec. 3

### 3 Opacity derivation

In NIKA2, the opacity is measured via a total-power technique, which was successfully tested with NIKA. The details of this technique and its agreement with the Atmospheric Transmission at Microwaves (ATM) model ([?]) are described in [20]. The underlying idea is to replace the opacity, usually delivered by the resident IRAM tau-meter that performs elevation scans at a fixed azimuth and is operating at 225 GHz, by a measurement that uses the NIKA2 instrument itself as a tau-meter. Using this procedure we can directly derive an opacity integrated in the NIKA2 very bandpasses and in the same line-of-sight of the source in the considered map. For that purpose, we assume that the resonance frequency of each KID varies linearly with the total power. First, we have to calibrate the relationship between total power and opacity. Then we can use that calibration to measure the opacity during a given scan.

#### 3.1 Methodology

For each kid  $k$ , the absolute value of the resonance frequency  $f_{tone}^k$  moves with the atmospheric load according to

$$f_{tone}^k = C_0^k - C_1^k T_{atm} [1 - e^{-\tau / \sin \delta}] \quad (3)$$

where  $C_0^k$  is a constant equal to the resonance frequency at zero opacity,  $C_1^k$  is the calibration conversion factor in kHz/K,  $T_{atm}$  is the equivalent temperature of the atmosphere (taken as a constant at 270K),  $\tau$  the zenith opacity and  $\delta$  the average elevation of the telescope. By assuming a homogeneous plane-parallel atmosphere, the airmass  $x$  is defined from the elevation as  $x = \sin \delta$ .

The coefficients  $C_0^k$  and  $C_1^k$  are expected to be constant in time within at least a cooldown cycle, and are determined using a skydip procedure. This consists in moving the telescope in elevation step by step and monitoring, for each kid, the evolution of  $f_{tone}^k$  versus the air mass and to fit the zenith opacity  $\tau$  and  $C_0^k$  and  $C_1^k$ . During a skydip, the telescope performs eleven steps in the elevation range from 19 to 65 degrees, regularly spaced in airmass. For each step, we acquire about twenty seconds of time traces to reduce the error in the determination of  $f_{tone}^k$ .

All skydips, obtained under various opacity conditions, are analysed together to break the degeneracies between the opacity and the responsivity ( $C_1^k$ ). The procedure has two steps. First, all the skydips are analysed individually to simply extract  $f_{tone}^k$  for each stable elevation. Secondly, a simultaneous fit is done for all parameters ( $\tau$ ,  $C_0^k$  and  $C_1^k$ ). Error bars on  $\tau$  are estimated by doing this procedure on blocks of 40 kids only and getting a dispersion on the resulting  $\tau$  from the different blocks. Usually the dispersion comes out as  $4 \times 10^{-3}$  at 1 mm and  $1 \times 10^{-3}$  at 2 mm. Once the  $\tau$  values are estimated for each skydip (as the average over the blocks), we compute (while fixing  $\tau$ ) the  $C_0$  and  $C_1$  final values for each KID. We thus retrieve the coefficients of all the KIDs even though some of them could not contribute to the  $\tau$  determination.

#### 3.2 Opacity measurement consistency tests

We observe that the skydip-fitted  $\tau$  values are, as expected, common between different detectors of the same array (the two 1mm arrays show slightly different values). By comparing the results of different skydips, we have verified experimentally that the coefficients  $C_0$ ,  $C_1$  are stable,

within the fit errors, on very long time scales within a cooldown cycle. The coefficients can thus be applied to the whole observing campaign in order to recover the opacity of each scan.

In Fig. 6 (and Fig. 5 of ??) we present the evolution of the NIKA2 in-band opacities for all the ‘OTF’ scans (about 1300 scans per runs) of the N2R9 run held in February and the N2R10 run in April 2017. These are compared to the IRAM tau-meter values. We observe an agreement on the global trend between the IRAM tau-meter opacity (225 GHz) and the NIKA2 values. These latter show, however, a smaller dispersion (less than one percent).

We find an average ratio between the 150 GHz and the 260 GHz NIKA2 values of about 0.6, a bit higher than ATM model expectations. We notice however that the 150 GHz-to-260 GHz opacity ratio varies significantly for opacities (at 150 GHz) below 0.2. This effect is likely to be linked to an  $O_2$  atmospheric line which becomes saturated or to some spillover at 2mm. This point is, however, still under investigation.”

The ratios between the 150 GHz and the 260 GHz NIKA2 zenith opacity estimates, quoted  $\tau_{2mm}$  and  $\tau_{1mm}$ , and between the NIKA2  $\tau$  and the IRAM taumeter values are presented in Fig. ??, along with the expectation values derived for NIKA2 bands using the ATM model described in ???. Namely, these predicted values  $\tau^{th}$  are calculated from the ATM-model atmospheric zenith opacity  $\tau^{ATM}$  using:

$$\tau_{A_i}^{th} = -\ln \frac{\int e^{-\tau^{ATM}(\nu)} T_{A_i}(\nu) d\nu}{\int T_{A_i}(\nu) d\nu}, \quad (4)$$

where the NIKA2 bandpasses  $T_{A_i}$  for arrays  $A_i$ ,  $i = 1, 2, 3$ , are the Martin-Pupplet reference transmissions corrected by a Rayleigh-Jeans term  $T'_{A_i}(\nu) / \left(\frac{\nu}{\nu_0}\right)^2$ .

In Fig. 11, we show the ratio of the atmospheric emission in NIKA2 bands defined as:

$$R_{\text{atm}} = \frac{1 - e^{-\tau_{2mm}}}{1 - e^{-\tau_{1mm}}}. \quad (5)$$

It is compared with the ATM-model predicted ratio

$$R_{\text{atm}}^{th} = \frac{\int (1 - e^{-\tau^{ATM}}) T_{A_2}(\nu) d\nu}{\int T_{A_2}(\nu) d\nu} / \frac{\int (1 - e^{-\tau^{ATM}}) T_{A_1}(\nu) d\nu}{\int T_{A_1}(\nu) d\nu}. \quad (6)$$

In Fig. 10, we investigate different effects that can impact the precision with which the zenith opacities are determined: the upper panel shows the expected dispersion in the NIKA2  $\tau$  values coming from the transmission measurement uncertainties: to highlight this effect, we consider a very pessimistic relative uncertainty of 10% (whereas 1% would have been a more realistic value), and the lower panel shows the impact of the uncertainty on the fraction of oxygen in the atmosphere, which mainly translates in an uncertainty on the atmospheric absorption around 118 GHz: the nominal absorption predicted by the ATM model is modified by a factor from 0.5 to 2 in the 117 – 120 GHz frequency band, where the  $O_2$  contributions largely dominates the water vapor ones.

We have compared  $C_0$  values, the resonance frequency at zero atmosphere, between different runs. It appears to vary in a systematic manner. For example we have compared N2R6 and N2R7. The change of frequencies when converted to temperature (with  $c_1$ ) is of about 25 and 86 K at 1 and 2 mm. This cannot be a real change of the background. Translated back by a median value of  $c_1$  (= 2500 and 1500 Hz/K at 1 and 2 mm), we obtain a 62.5 and 128 kHz median downward shift of all resonant frequencies between N2R6 (October 2016) and N2R7 (December

2016). The likely explanation is that of a slight ageing of the KIDs. A single monolayer of oxyde could be enough to produce the downward shift.

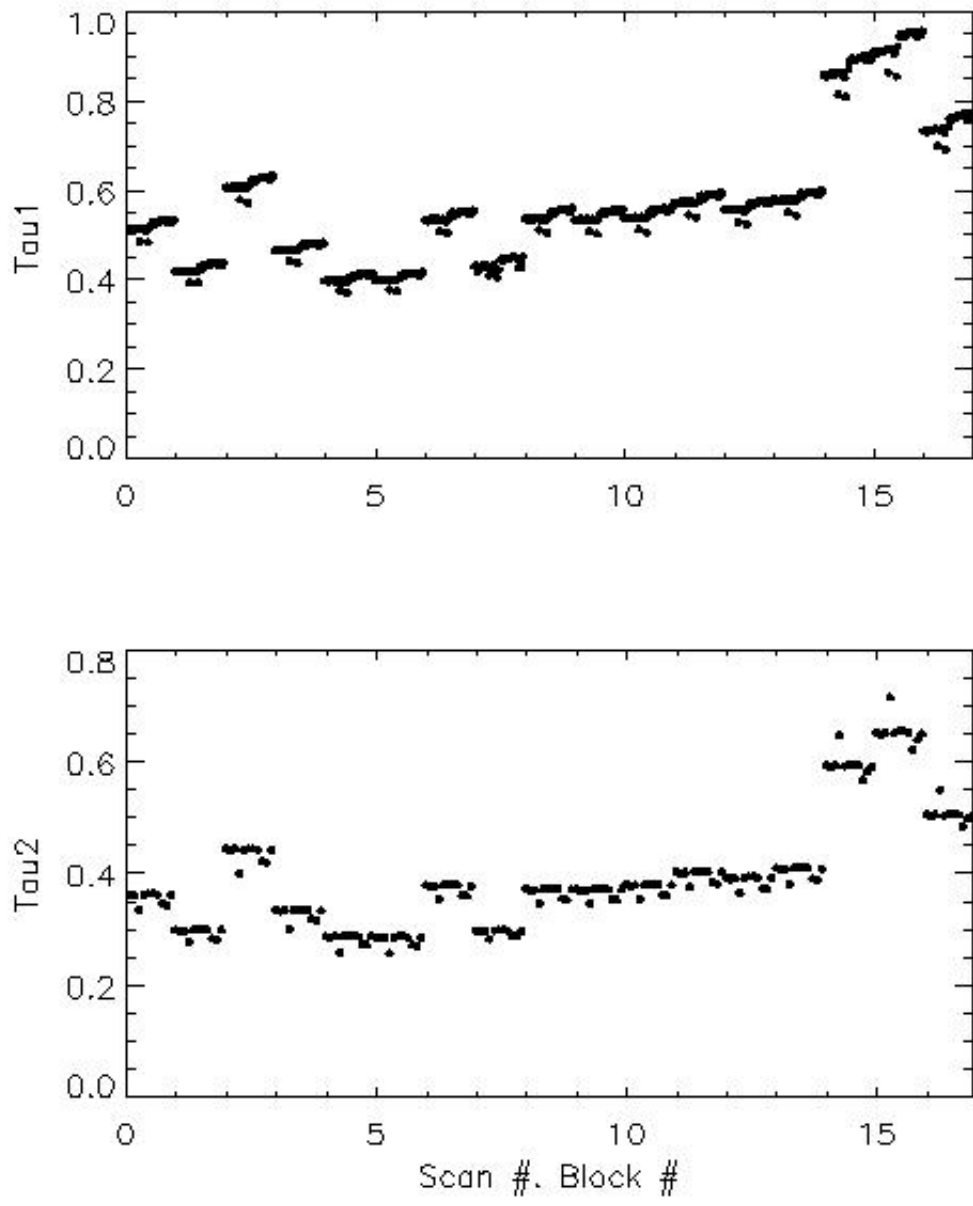


Figure 3: Atmospheric opacity as measured from the NIKA2 data at 260 (top) and 150 GHz (bottom) during N2R10 commissioning campaign. Each block of 40 KIDs gives an independent estimate of the opacity value for each skydip scan (the integer abscissae). The block number is the decimal value of the abscissae.

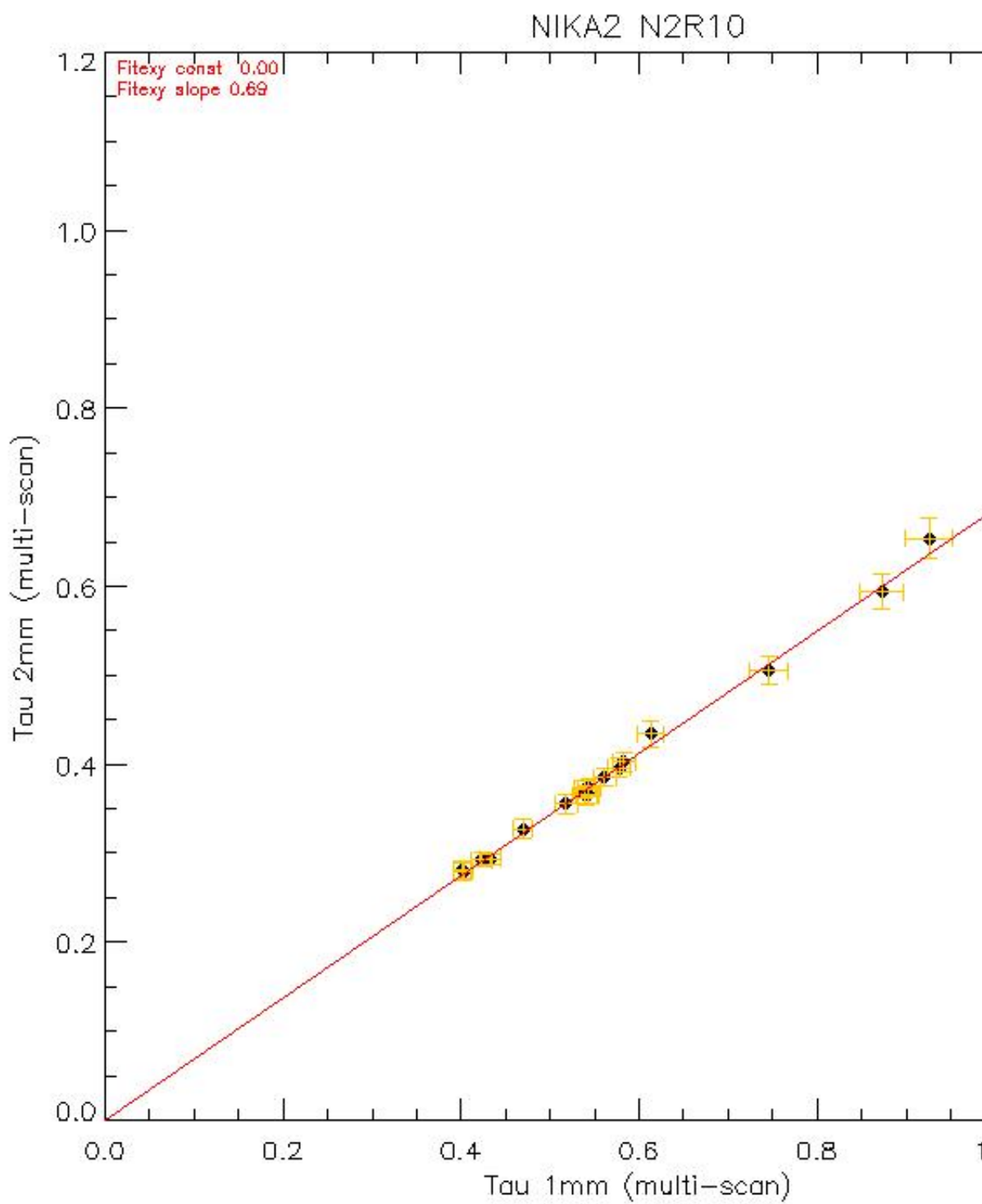


Figure 4: Atmospheric opacity as measured from the NIKA2 data at 260 and 150 GHz during N2R10 commissioning campaign. The error bars are in fact dispersion of the deduced opacities between blocks of 40 KIDs.

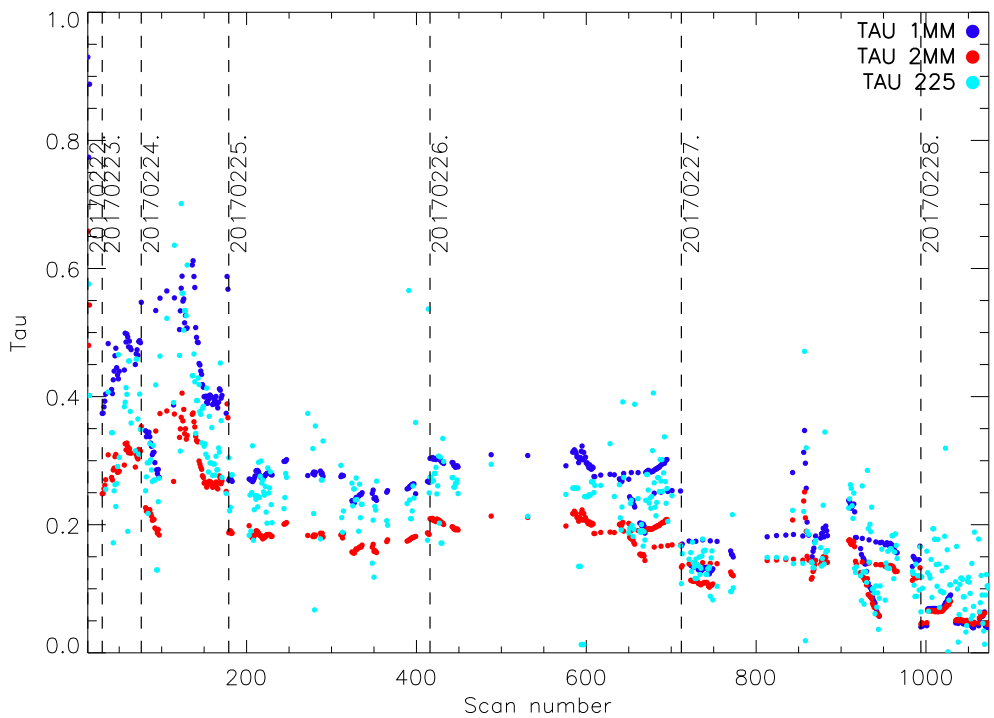


Figure 5: Atmospheric opacity as measured from the IRAM 225 GHz taumeter (cyan), and from the NIKA2 data at 150 (red) and 260 GHz (blue) during N2R9 commissioning campaign (Feb. 2017). We stress the fact that the IRAM 225 GHz taumeter data is not used for the atmospheric correction and is plotted here just for comparison.

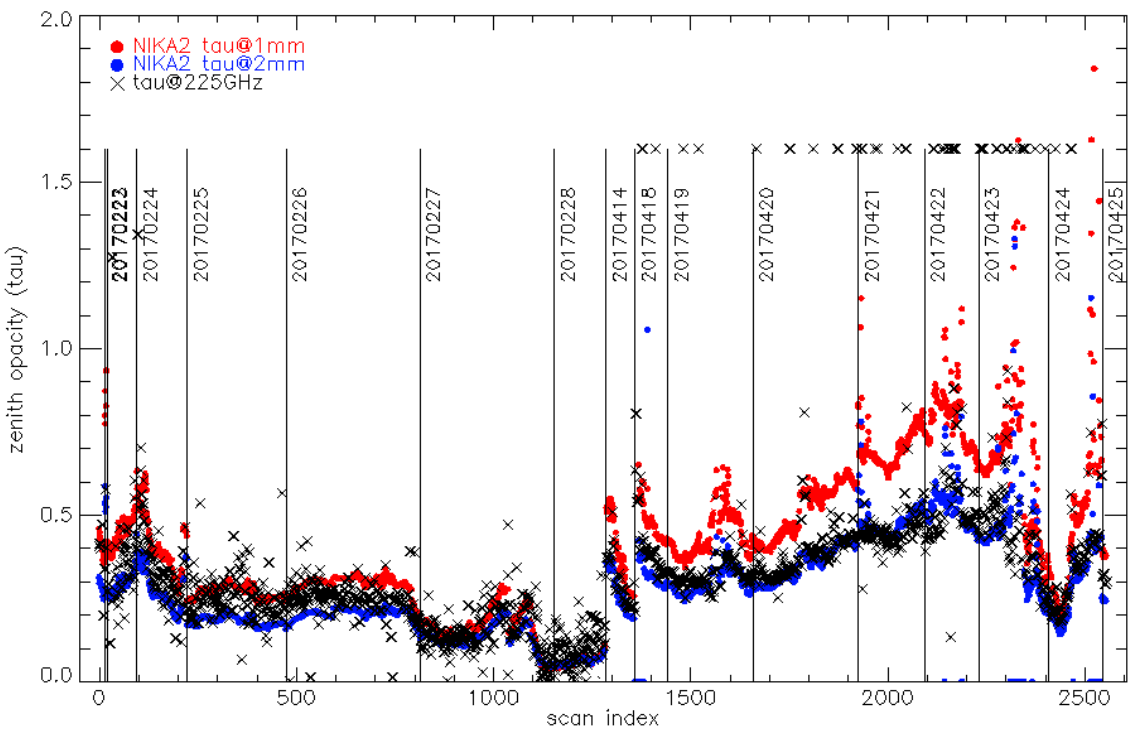


Figure 6: Atmospheric opacity as measured from the IRAM 225 GHz taumeter (black crosses), and from the NIKA2 data at 150 (red) and 260 GHz (blue) during N2R9 and N2R10 commissioning campaigns. We stress the fact that the IRAM 225 GHz taumeter data is not used for the atmospheric correction and is plotted here just for comparison.

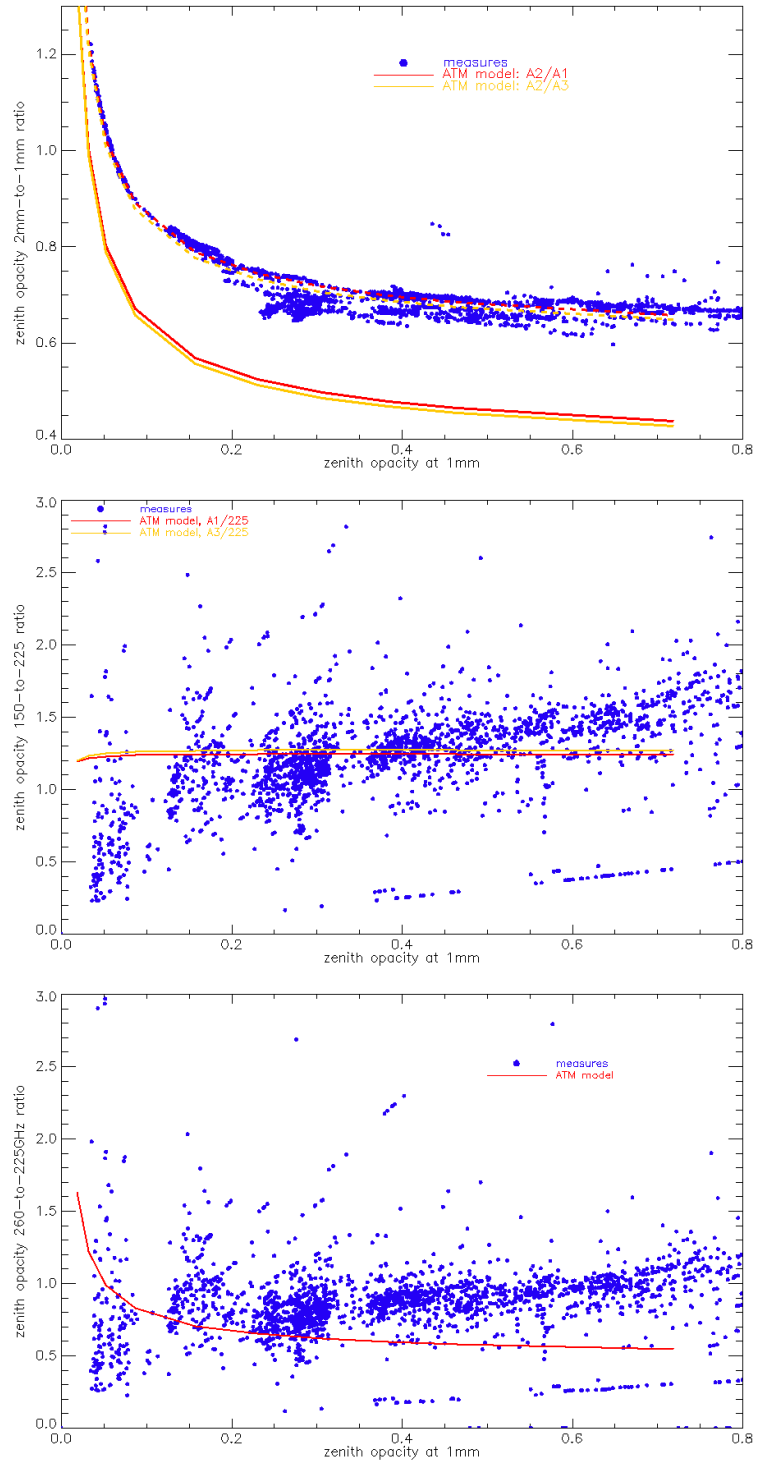


Figure 7: Ratios between the 150 GHz and the 260 GHz NIKA2 zenith opacity estimates and between the NIKA2  $\tau$  and the IRAM tau meter values. The expectation values derived for NIKA2 bands using the ATM model described in ?? are shown for comparison (red and orange curves).

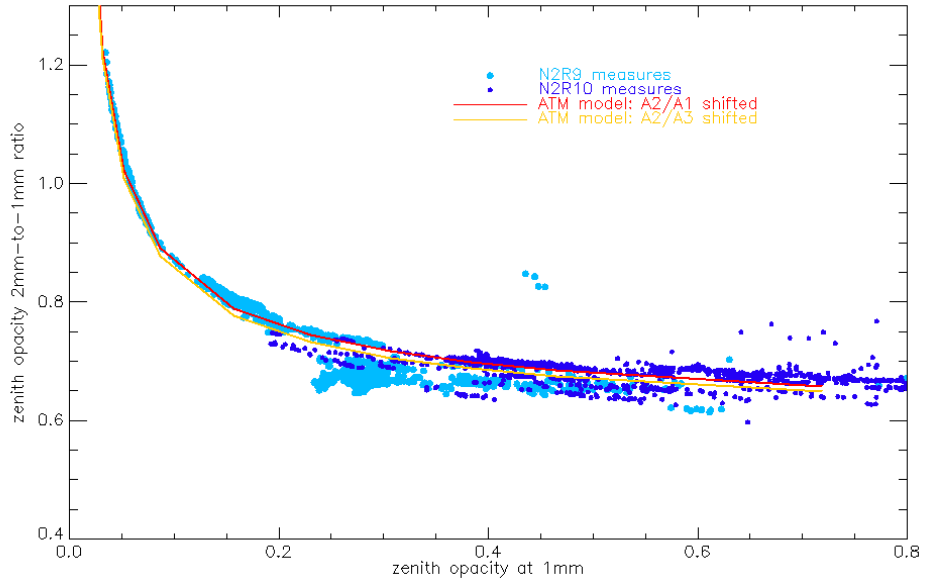


Figure 8: Ratio between the 150 GHz and the 260 GHz NIKA2 zenith opacity estimates. The expectation values derived for NIKA2 bands using the ATM model described in ?? are shown for comparison (red and orange curves). The observed NIKA2 opacity ratio has a smooth, consistent behaviour over the overall probed opacity range, and very few outlier estimates are seen although no scan selection has been performed (out from discarding the dark tests). Also remarkable is the consistency between estimates obtained during two campaigns held two months apart in different weather conditions (good to average during N2R9 and poor and often highly unstable conditions during N2R10). Some sub-structures are seen in the opacity ratio, which are under investigations. They can have several origins (telescope cabin temperature variation, variation of the  $O_2$  fraction, atmospheric temperature variation, internal temperature variations, etc).

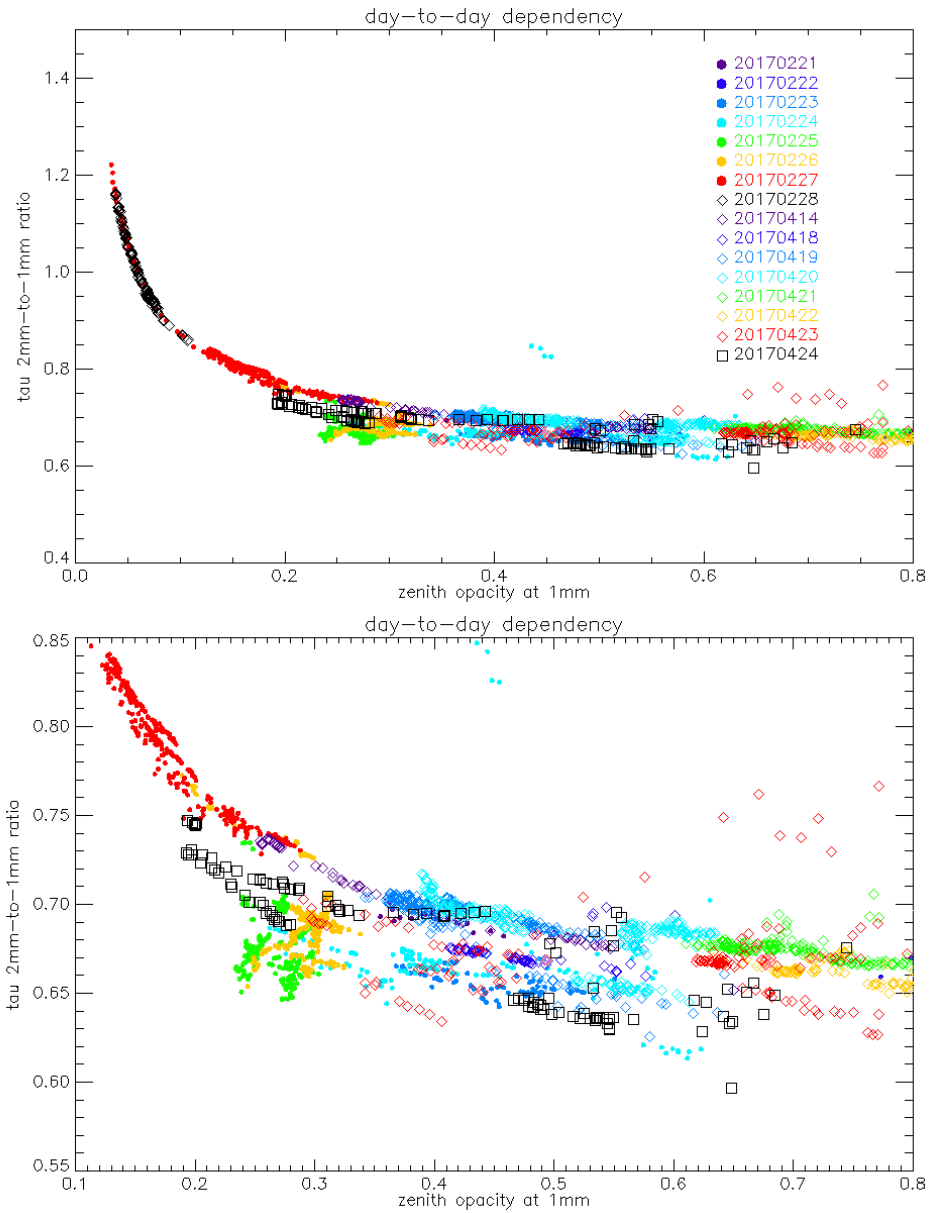


Figure 9: Ratio between the 150 GHz and the 260 GHz NIKA2 zenith opacity estimates. The 4 outlier estimates on February, 24 (in cyan) correspond to a test using the external calibrator. Different regimes are seen on the 25th and 26th of February, while the weather conditions were too unstable to allow the astronomer team to focus.

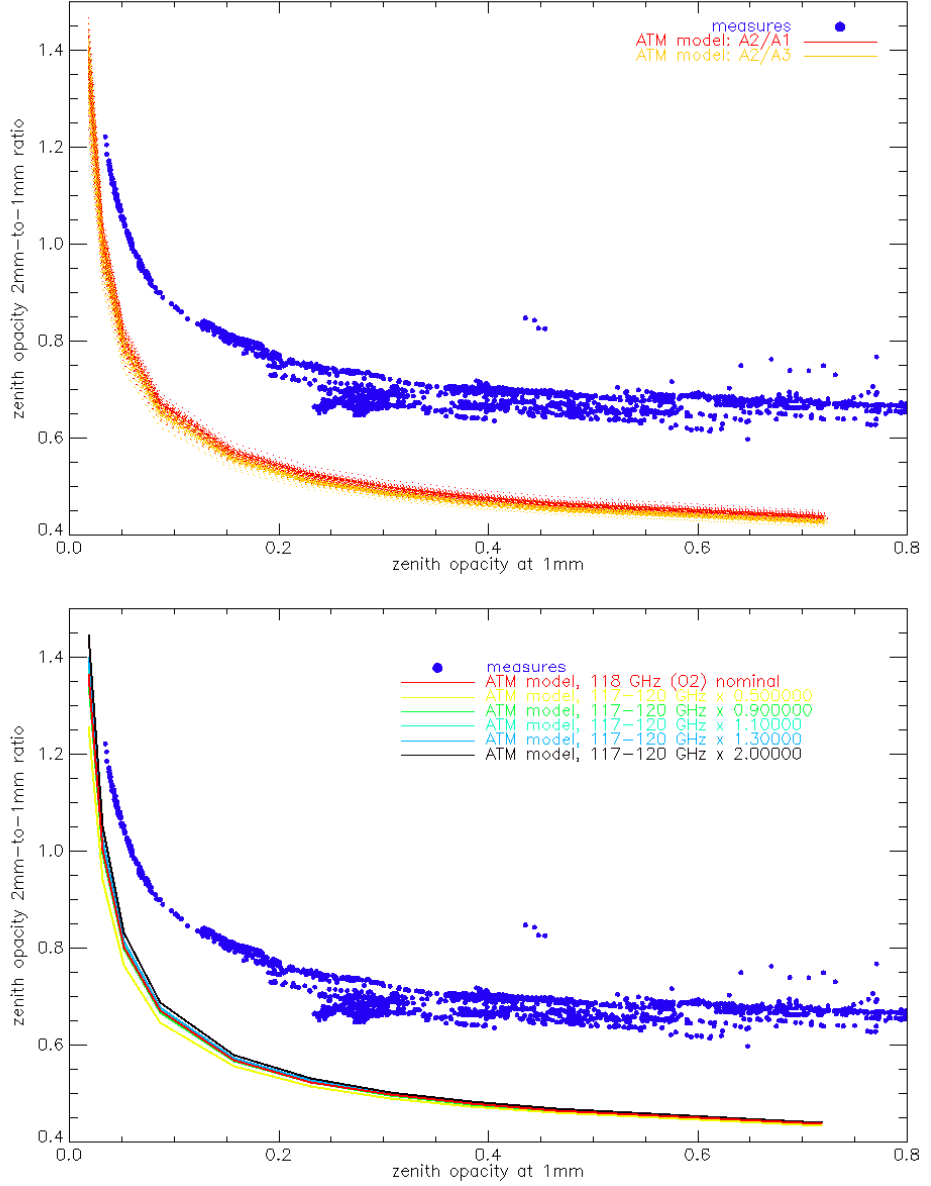


Figure 10: Uncertainty of NIKA2  $\tau$  values. Upper panel: The impact of the NIKA2 transmission measurement uncertainties is illustrated using a very pessimistic relative uncertainty of 10% (instead of the more realistic 1% errors). Lower panel: The impact of the uncertainty on the atmospheric absorption around 118 GHz, due to the lack of precise knowledge of the fraction of oxygen in the atmosphere. The nominal absorption predicted by the ATM model is modified by a factor from 0.5 to 2 in the 117 – 120 GHz frequency band, where the  $O_2$  contributions largely dominates the water vapor ones.

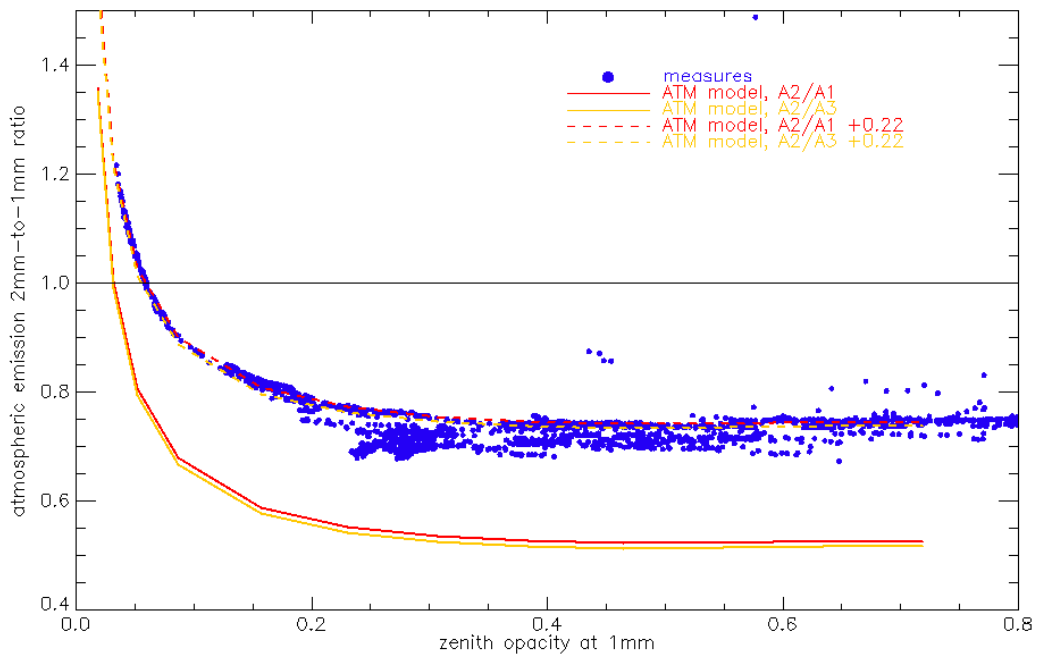


Figure 11: Ratio of the atmospheric emission in NIKA2 bands defined as in Eq. 5, compared with the ATM-model predicted ratio calculated as in Eq. 6

## 4 Focal Plane Reconstruction

### 4.1 Methodology

In order to determine the pointing offsets of each KID with respect to the reference sky coordinates as commanded by the telescope tracking system, we perform a *beammap*, that is to say we map a bright and compact source, most of the time a planet, with an elevation step small enough to meet Nyquist sampling at the 1-mm beam scale, namely 4.8 arcsec. We observe this planet with a raster scan in (az,el) coordinates, either with fixed elevation subscans or fixed azimuth subscans. The former has the advantage of low air mass variation across a subscan, the latter offers an orthogonal scan direction to the former: the combination of both gives a more accurate determination of the far side lobes. The data reduction proceeds in two steps.

**Step 1.** We apply a median filter per KID timeline whose width is 4 FWHM and we project one map per KID in Nasmyth coordinates. This median filter removes efficiently most of the atmospheric and low frequency electronic noise, albeit a slight ringing and flux loss on the source. However, at this stage, we are only interested in the location of the observed planet. To derive the Nasmyth coordinates from the provided (az,el) coordinates, we build the following quantities at time  $t$  :

$$\begin{aligned} dx_t &= \cos el_t daz_t - \sin el_t del_t \\ dy_t &= \sin el_t daz_t + \cos el_t del_t \end{aligned}$$

**FM: why not using  $\delta$  as in the previous section ?**

**FM: i don't think the  $t$  is useful**

where  $el_t$  is the elevation of the reference pointing direction and  $daz$  and  $del$  are the pointing offsets with respect to the source in azimuth and elevation as provided by the tracking system. Note that  $daz$  is already corrected by the  $\cos el_t$  factor to have orthonormal coordinates in the tangent plane of the sky and be immune to the geodesic convergence at the poles. We then fit a 2D elliptical gaussian on each kid map. The centroid of this gaussian is a first estimate of the KID offsets, FWHM's, ellipticity and sensitivity. We apply a first KID selection by removing outliers to the statistics on these parameters. We also discard manually KIDs that show a cross-talk counter part on their map.

**Step 2.** With the Nasmyth offsets derived in step 1, we are now able to mask out the planet in each KID timeline. This mask is centered on the planet location as seen by each kid, it is circular and has a radius of 60 arcsec. We now build a template timeline (a.k.a. "common mode") in two steps. First, we take the median of all samples of all KIDs that are outside this mask at a given time  $t$ . This gives a first estimate of the common mode. Second, we cross-calibrate each KID on this common mode when the KID is outside the mask and we coadd all these KID cross-calibrated timelines when they are outside the mask to have the final common mode. In this sum, each KID TOI is weighted by the inverse of its variance outside the mask. Once we have this common mode in hand, we cross-calibrate each TOI on it outside the mask and we subtract it to the entire KID TOI. We then resume to the projection of each KID TOI in Nasmyth

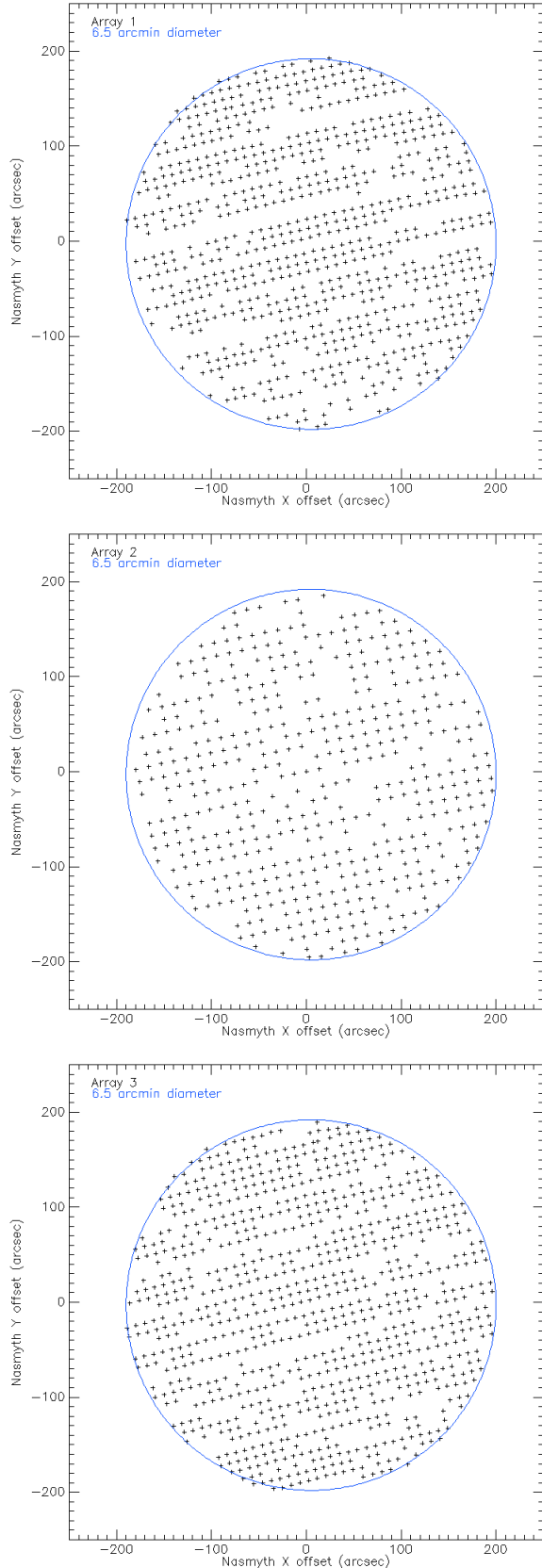


Figure 12: Nasmyth offsets of each array, from beammap 20170226s415 on 3C84 (N2R9).

coordinates like in step 1, and the 2D elliptical gaussian fit on the each kid map. The centroid coordinates and the FWHM are now the final parameters that can be derived on the current scan.

This analysis is repeated on all beam maps, which provides statistics and precision on each KID parameter, together with estimates on KID performance stability.

**FM : precision ?  
show a screen capture of Katana.**

We present an example of the FOV reconstruction in Fig. 12.

The FOV diameter is defined as

$$FOV\text{diameter} = \sqrt{4N_{tot.kids} \times gridstep^2 / \pi} \quad (7)$$

**give the values of gridstep (pitch) both in mm and arcsec on the sky**

The same definition applies to “Effective FOV” to avoid extra multiplication by the fraction of valid pixels

$$F\lambda = gridstep \times D(30m) / \lambda \quad (8)$$

## 4.2 Average Focal Plane Reconstruction

**FM: Figures 13, 14 and 15 are too large. captions cannot be read**

In order to identify the most stable pixels, we compare the KIDs parameter obtained with several beam maps. In the following, we show results as obtained using seven beam maps from Run10, two from Run9 and one from Run8. For each pixel we compute the average position on the focal plane and the average FWHM, counting the times that it has been considered as valid.

In Fig. 13 we show the average focal plane reconstruction, from green to red depending on the number of times that the pixel has been considered as valid. For A1, A3 and A2, respectively, we have 952, 961, and 553 pixels that have been considered as valid at least twice (840, 508, 868 valid at least five times). Using this criterion, we deduce the fraction of valid detectors over the designed ones, as given in Table 4. As a second step, we also flag pixels that move across the focal plane from a beam map to another (Fig. 14 , jumping KIDs) and those who share the same position (twin KIDs). To identify the former, we look at the difference of the mean and median position of each KID (the red crosses and black squares in Fig. 15). For the latter a criterion on the position is applied in order to find the pixels that are closer than the grid step.

**FM: how many twins ? how many jumping kids ?**

Array	Designed detectors	Valid detectors	Fraction
A1	1140	952	84%
A3	1140	961	84%
A2	616	553	90%

Table 4: CAPTION

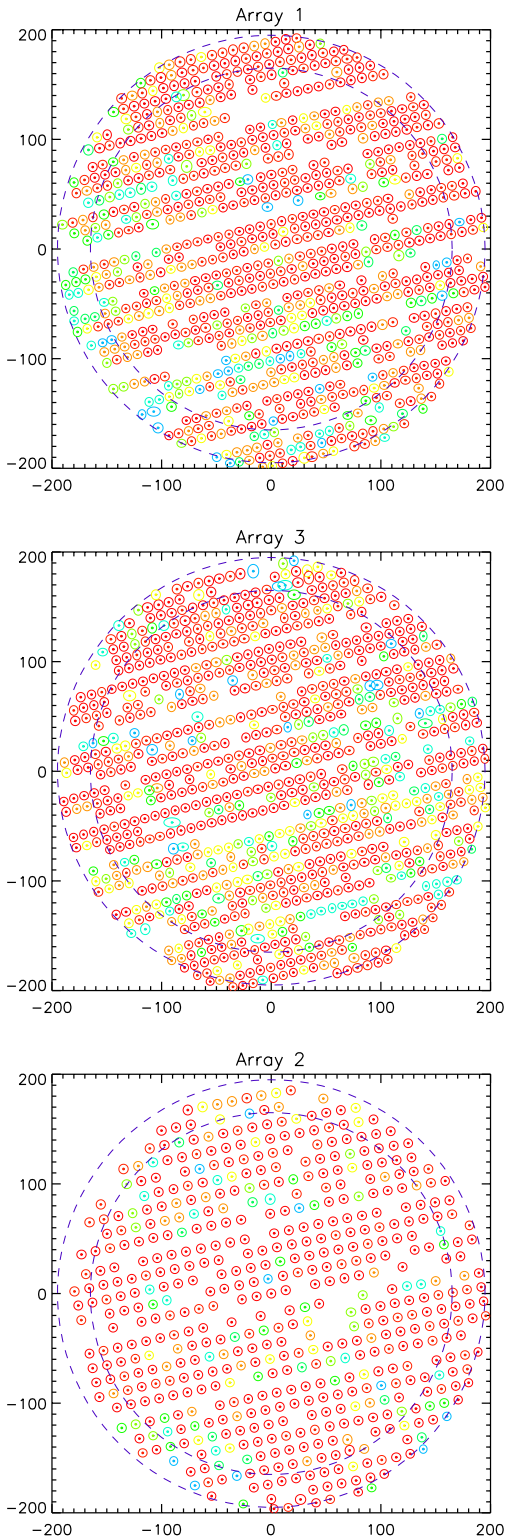


Figure 13: Average detectors positions for arrays A1, A3, and A2 (from green to red as a function of the number of times that a given pixel has been considered as valid). The three plots show the detectors that have seen the sky and passed the quality criteria for at least two beam maps during Run10, 9 and 8: 952, 961, and 553 for A1, A3 and A2, respectively. The inner and outer dash-line circles correspond to a FOV of  $5.5^{\circ}$  and  $6.5^{\circ}$ , respectively. Units are arcseconds. The color (from green to red) shows the number of times that a given pixel has been considered as valid.

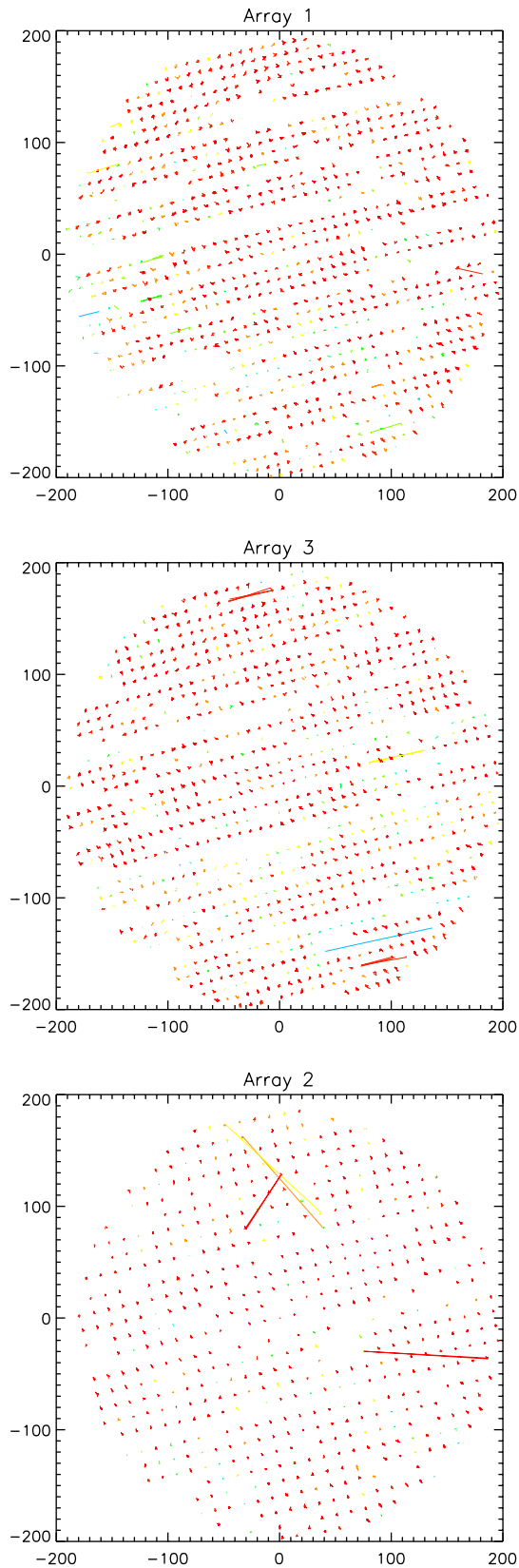


Figure 14: For the valid detectors, we show the positions of each pixel, as obtained from each beam map. Some of them are not found at the same position for all the beam maps. Units are arcseconds. **FM : color code ?**

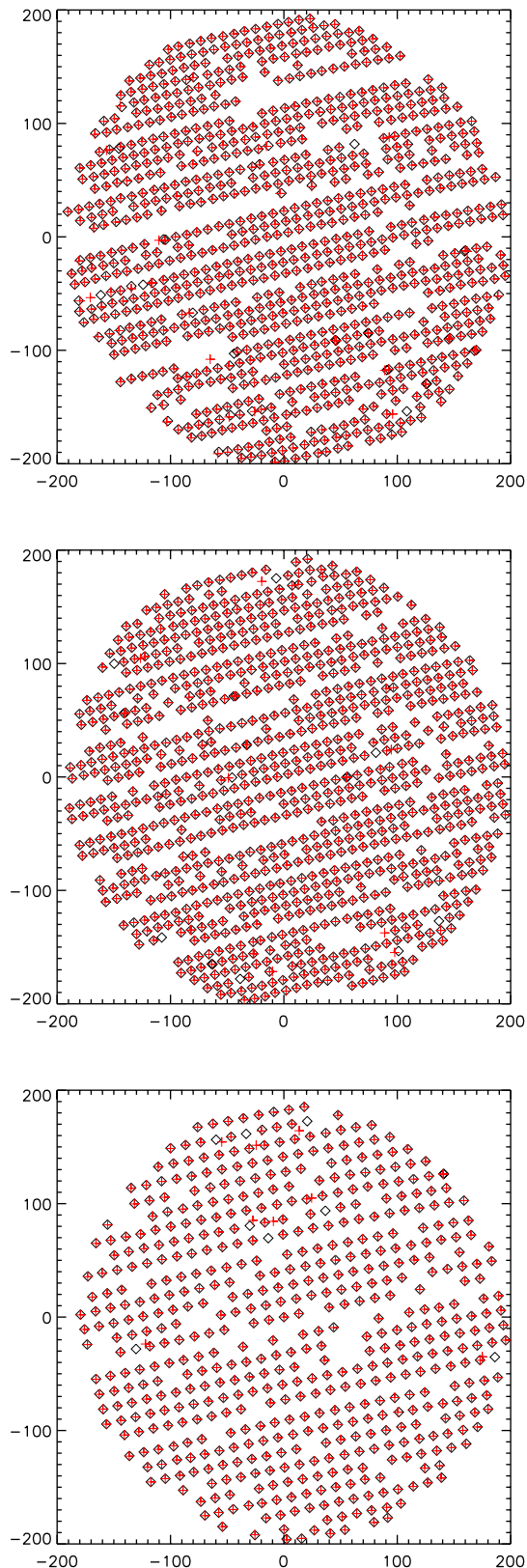


Figure 15: For the valid detectors, we show the mean (red crosses) and the median (black squares) positions of each pixel, as obtained from each beam map. Units are arcseconds. **FM : color code ?**

### 4.3 FOV grid distortion

#### LP edit using Samuel's comments, [TBC]

We studied the matching of the KIDs position on the sky to the *design* position, as described in detail in this wiki post<sup>1</sup> The global result is scaling, rotation, and shift parameters for each array. They are described in Table 4.3.

Array 1	Array 3	Array 2	Comment
1 mm	1 mm	2 mm	
1140	1140	616	Total of designed Kids
736/673	758/734	444/437	Found/Well-placed Kids
91/59	96/64	98/71	Fraction [%] of WPK/FoundKids and WPK/Total
0.87	0.84	0.66	Median deviation (arcsec) for pixels with a deviation smaller than 5 arcsec
0.52	0.69	0.68	Mean distortion across the FoV in arcsec
2.3 -4.5	2.0 -5.8	9.3 -7.5	Array center in Nasmyth coordinates (arcsec)
4.90	4.88	4.88	Plate scaling (arcsec/mm) in the Design x and y (averaged)
77.3	76.4	78.2	Plate rotation angle (degree) from the Design to Nasmyth coordinates
6.6	6.6	6.6	FOV (Total kids)
9.8/2.00	9.7/2.00	13.3/2.75	Distance between near detectors [arcsec, mm]
1.24	1.22	0.97	Distance between near detectors [in lambda/D]

Table 5: Linear 2D fit of the observed position of the detectors in the sky against their mechanical designed position for N2R9.

It shows that on average the position of each detector is known to better than an arcsecond. The 1mm arrays have almost the same center but this center differs by 7 and 2 arseconds from the 2mm array center. The sampling is above  $\lambda/D$  at 1 mm. Note that the plate rotation angle was designed as 76.2 degrees, less than 2 degrees from what is observed. We find that array 1 has the most deviant detectors (above 4 arcseconds from their expected position). These detectors should be excluded from further analysis. We call distortion (in the table) the  $x.y$  term in the polynomial fitting between the design grid and the observed position (the fitting is done with the  $x$  and  $y$  linear terms and  $x.y$  term).

This has been compared to expectations obtained using ZEMAX simulation. The grid diagram generated using ZEMAX provides us with the maximum dispersion in the field defined by

$$P = \frac{\sqrt{(x_p - x_r)^2 + (y_p - y_r)^2}}{\sqrt{x_p^2 + y_p^2}}, \quad (9)$$

where  $(x_p, y_p)$  and  $(x_r, y_r)$  are respectively the predicted and real coordinates on the image surface relative to the reference field position image location (see page 170 of the ZEMAX manual, 2007). The predicted coordinates for the whole field are obtained using a linear interpolation of a small area in the field central part, whereas the real coordinates are calculated by ray tracing through the optical system.

---

<sup>1</sup>see <http://www.iram.fr/wiki/nika2/index.php/>

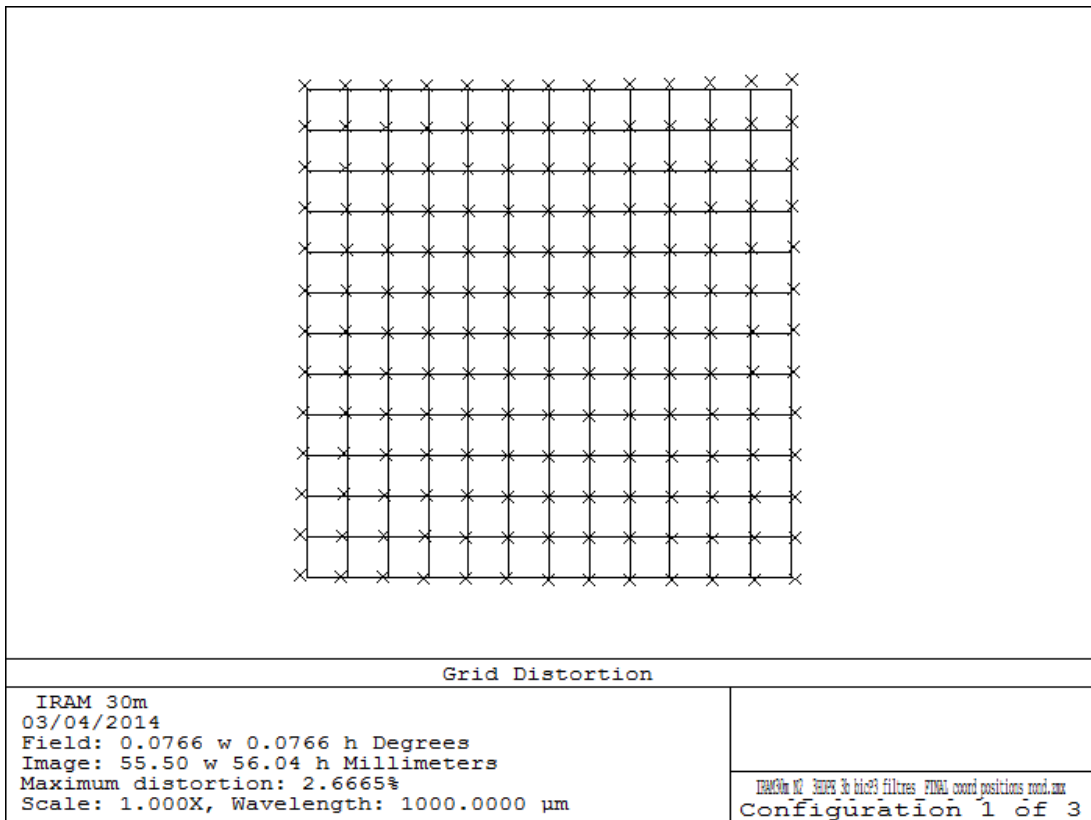


Figure 16: NIKA2 grid diagram simulated using ZEMAX. Crosses indicate the real coordinates on the Nasmyth image plan. **question à Samuel: pourquoi les dimensions indiquées sont environ 4.5 arcmin de côté (et pas 6.5)?**

Figure 16 show the ZEMAX grid diagram for NIKA2 simulated optic system. The maximum grid distortion is expected to be of 2.7% in NIKA2 6.5' FOV. The distortion is the most noticeable in the upper right corner of the Nasmyth plan, which is also the area of the largest defocus w.r.t. to the center.

An expected distortion of 2.7% is at most a 5 arcsecond shift from the center to the outside of the array. The quoted measured distortions are not too dissimilar once the different fitting methods have been taken into account.

## 5 Pointing accuracy

Based on general operating experience at the 30-m telescope, we use the so-called *pointing* or *cross* scans to monitor the pointing during observations. The telescope executes a back and forth scan in azimuth and a back and forth scan in elevation, centered on the observed source. Looking at the timeline profiles of the reference detector, we fit gaussian profiles and derive the current pointing offsets of the system in azimuth and elevation. These offsets can then be passed to PAKO to recenter the next scan (Fig. 17).

Such scans and their analyses are also used to improve the pointing model of NIKA2. A pointing session consists in observing about 30 sources on a wide range of elevations while monitoring the pointing offsets that are measured for each observation. These offsets are then passed to the IRAM staff who finds the pointing model parameters that minimize and symetrize the scattering of these offsets (cf. Fig. ??). Bases on these results Nasmyth offsets are then modified.

**FM : add a figure showing the IRAM fit**

Fig. 18 shows the pointing corrections that had to be applied during Run9, before and after the modification of the Nasmyth offsets.

While the absolute values of the corrections is somewhat arbitrary and set around zero for convenience, the dispersion of the offsets is the true figure of merit of the pointing corrections. The distribution of corrections after the corrections (in yellow to red) is clearly more symmetric and narrower than before. During N2R9 run, the pointing accuracy was 1.62 arcsec rms in azimuth and 1.37 arcsec rms in elevation.

**FM : are these values typical ? other runs ?**

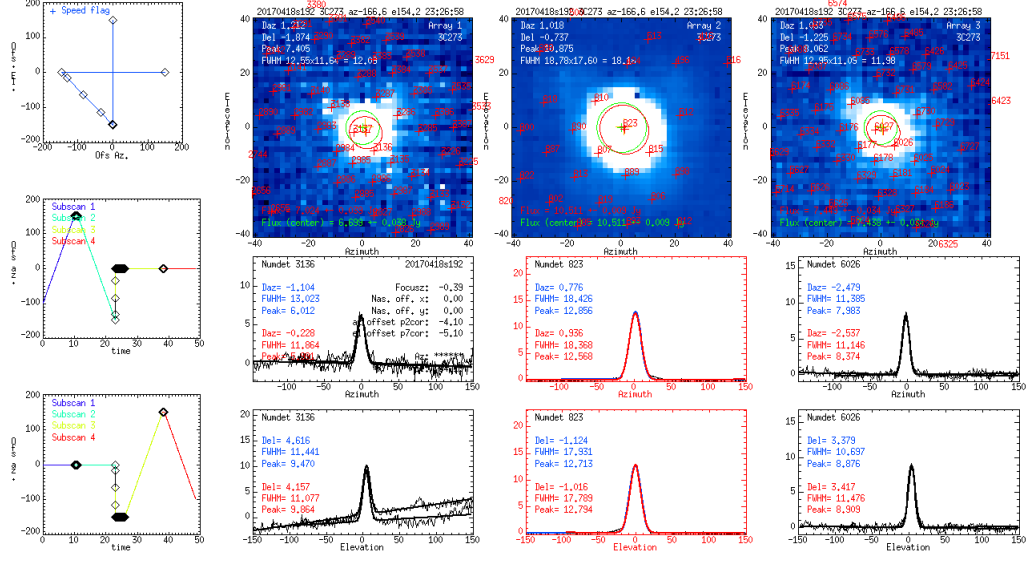


Figure 17: Summary plots of the reduction of pointing scan. There is one combined map per array to check the overall quality of the scan, and a set of azimuth and elevation profiles for one reference detector per array. The 2-mm reference detector, highlighted in red, is the the pointing reference detector of NIKA2. The location of the peak in azimuth and elevation, as observed by the reference detector gives the pointing offset of the current scan.

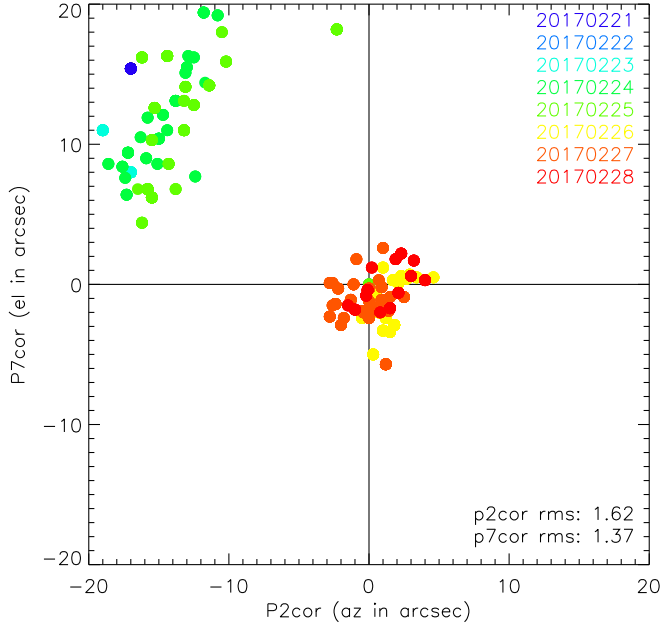


Figure 18: Pointing offsets during Run9 observations, before and after the derivation of Nasmyth offsets with a pointing session on Feb. 26th, 2017.

## 6 Beam pattern

The NIKA2 beam pattern mainly depends on the IRAM 30m telescope and NIKA2 full (external and internal) optical system characteristics, whereas the detectors themselves might have an impact at sub-dominant level (through e.g. time constants or correlated noises). In this section, first we reconstruct the focus surfaces and present the optimal focus, then we characterize both the main beam, which is modeled as an elliptical Gaussian, and the full beam pattern including error beams up to angular scales of 10 arcmin.

### 6.1 Optimal focus

Owing to the NIKA2 6.5 arcmin FOV, the focus is expected to slightly change across the FOV, defining curved focal surfaces at the location of the three arrays. Therefore, beam patterns are expected to show some scatter across the FOV accordingly to the focal surfaces. Although all the detectors cannot be individually focalized, an optimal axial focus of the telescope can be found to maximize the number of detectors at the best focus and hence, maximize the resolution of the NIKA2 maps. This optimal z-focus setting is obtained in measuring the focus at the center of the arrays as described Sect. 6.1.1 and apply a focus shift, which is primarily predicted using Zemax simulation, and ultimately verified by measuring the focus surfaces, as described in Sect. 6.1.3.

#### 6.1.1 Focus estimation

The best axial focus in the central region of the arrays is estimated using the so-called ‘focus\\_OTF’ PAKO script, which realizes a series of five  $1' \times 5'$  OTF scans at various values of the focus in 0.4 mm-steps around an *a priori* value  $z_0$ , namely  $z \in \{-0.8, -0.4, 0, 0.4, 0.8\} + z_0$ . Elliptical Gaussian fits on the reconstructed maps provide estimates of the flux and FWHM along minor- and major-axis for each focus. Then, parabolic fits are used to determine the best focus. We consider three estimates: i)  $\hat{z}_{\text{peak}}$  the focus that maximizes the estimated flux, which is the amplitude of the 2D Gaussian, ii)  $\hat{z}_{\text{fwhm}}$  the focus that minimizes the geometrical FWHM, defined as the quadratic mean of  $\text{FWHM}_{\text{major}}$  and  $\text{FWHM}_{\text{minor}}$ , and iii)  $\hat{z}_{\text{ellipt}}$  the focus that minimizes the beam ellipticity, defined as  $\text{FWHM}_{\text{major}}/\text{FWHM}_{\text{minor}}$ . Fig. 19 shows an example of axial focus measurement using a ‘focus\\_OTF’ observation of Neptune during N2R10.

#### 6.1.2 Focus consistency between arrays

refaire les plots de difference de focus entre matrices

#### 6.1.3 Reconstruction of the focus surfaces

*Method.* We measure NIKA2 focal surfaces by means of a sequence of five ‘beam-map’ scan observations of bright point-like sources, typically Planets or bright quasars, for various settings of the telescope axial focus around the optimal focus  $z_{\text{opt}}$ . A beam-map scan consists of a deep-integrated  $13.5' \times 7.8'$  OTF-scan observation comprising 99 sub-scans and with a scanning speed of either  $65''/\text{s}$  whenever the mean integration elevation is  $< 60$  degree or  $39''/\text{s}$  at higher elevation. The z-focus is changed in step of 0.6 mm to probe a large focus range for measuring even the extreme variation of the focus surfaces, namely  $z \in \{-1.2, -0.6, 0, 0.6, 1.2\} + z_{\text{opt}}$ . Each beam-map scan allows for  $4''$ -resolution individual maps per kid to be projected. Before the

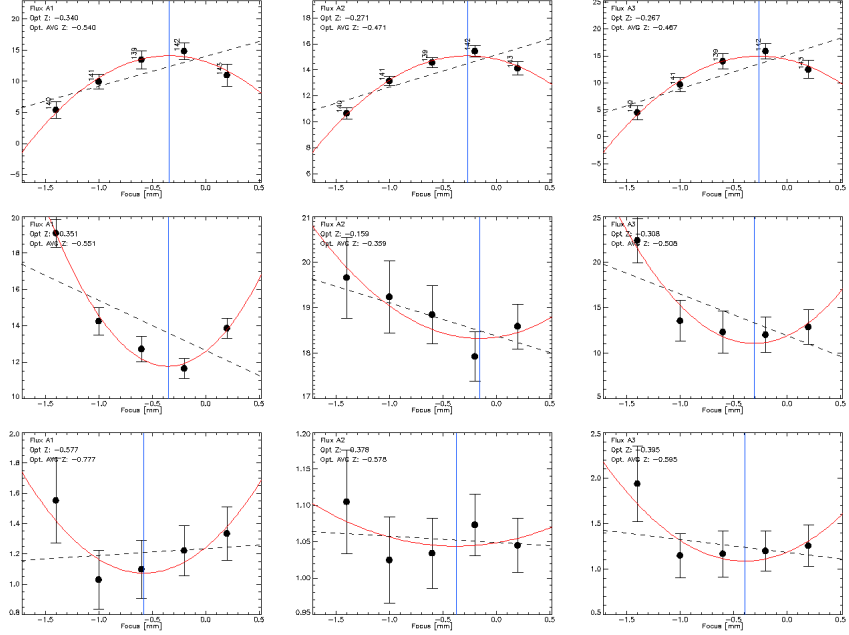


Figure 19: Example of axial focus measurement using a ‘focus\\_OTF’ observation of Neptune during N2R10 [PLACEHOLDER]

projection, the correlated noise is mitigated from each KID timeline in subtracting out a common mode, which is obtained using, amongst the other detectors, those that correlates the most with this KID and that are located outside a radius of  $90''$  around the source centroid. Therefore, a series of five cleaned maps at various focus is available for each detector, from which the best focus is estimated as described in Sect. 6.1.1. The ensemble of the relative focus estimate per KIDs with respect to the best focus at the center of the array constitutes the focus surface. An accurate estimate of the center focus is obtained as the weighted average focus estimate of the KIDs lying in a  $30''$  radius around the geometrical center of the array. This average does not induce any sizeable bias thanks to the flatness of the focus surface in the innermost regions. For robustness test, we consider three focus estimates: the two first ones are the same as discussed in Sect. 6.1.1 – namely i)  $\hat{z}_{\text{fwhm}}$  the focus that minimizes the geometrical FWHM and ii)  $\hat{z}_{\text{peak}}$  the focus that maximizes the amplitude of the best-fitting elliptical Gaussian – whereas the third one is  $\hat{z}_{\text{flux}}$  the focus that maximizes the amplitude of the best-fitting elliptical Gaussian of fixed FWHM (at  $12''$  at 260 GHz and  $18''$  at 150 GHz). The comparison between the two amplitude-based estimators ( $\hat{z}_{\text{peak}}$  and  $\hat{z}_{\text{flux}}$ ), will test the stability of the focus results against the exact choice of the beam fitting function. Since the ellipticity-based estimator  $\hat{z}_{\text{ellip}}$  is less sensitive to focus changes and yields larger uncertainties than the others, we do not use it for the focus surface reconstruction.

*Data selection.* During the three commissioning campaigns that occurred after the change of A1 lens and the improvement of internal optics alignment (hence in the final NIKA2 optic configuration), nine out-of-focus beam-map scan sequences have been acquired, including incomplete sequences and sequences hindered by poor atmospheric conditions. We select sequences that i)

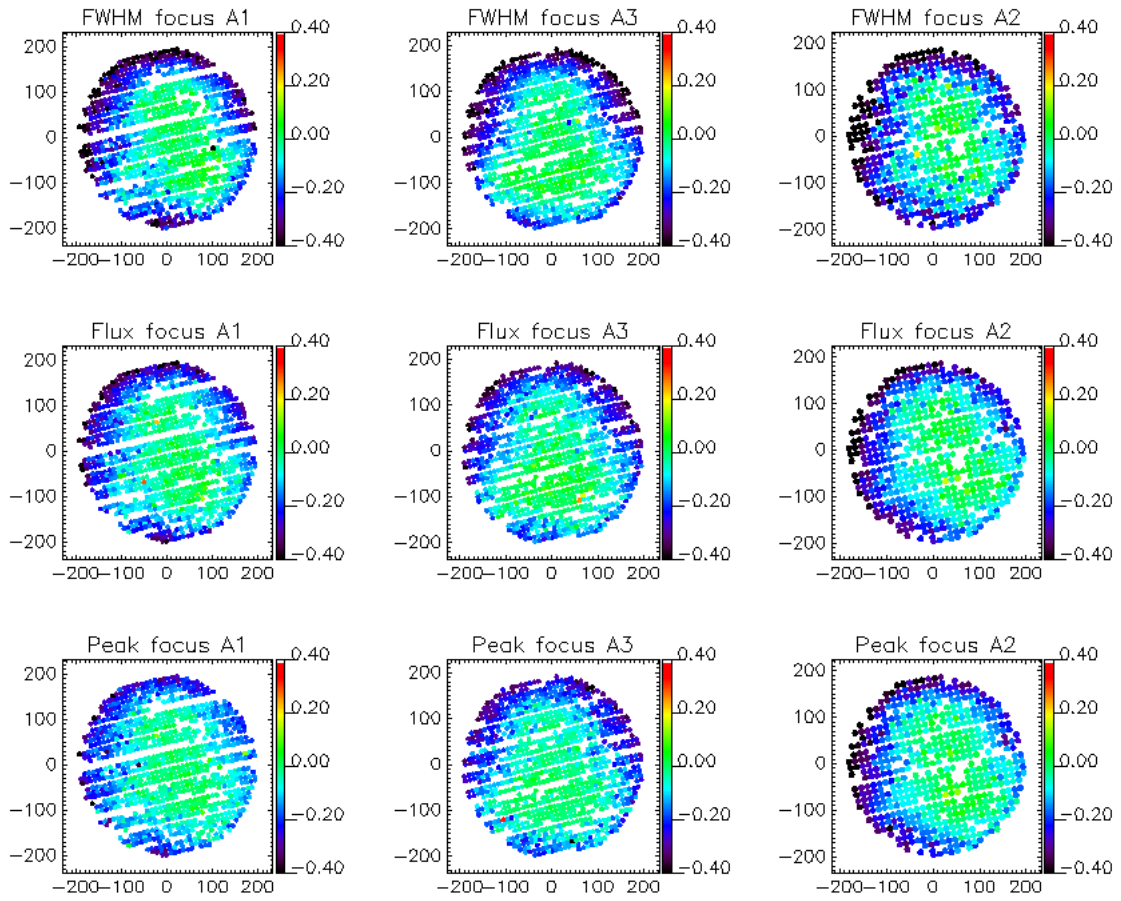


Figure 20: Focus surface of A1, A3 and A2 arrays from left to right. From top to bottom, the focus estimates rely on FWHM-minimization, amplitude-maximization of an elliptical Gaussian of fixed FWHMs and amplitude-maximization of an elliptical Gaussian.

comprises at least four scans, ii) have been observed at zenith opacity at 225 GHz (as indicated by the IRAM taumeter) below 0.5 and iii) have a maximal central focus drift between the starting time and the end of the sequence of 0.5 mm. These criteria preserve five sequences from which focus surfaces can be reconstructed. Namely, we consider the sequences 20170226s415–419, 20170419s133–137, 20170420s113–117, 20170421s160–164 and 20170424s123–127, which consist of observations of the bright quasar ‘3C84’ and Neptune.

*Results.* For each detector  $k$  and each beam-map sequence  $s$ , we obtain for the array  $a$ , a focus measurement  $z_k^{a,s} \pm \sigma_k^{a,s}$ , where  $\sigma_k^{a,s}$  is the 1- $\sigma$  error of the least-square polynomial fit. The focus surface measurements per array obtained from the five beam-map sequences are combined using an inverse-variance weighting scheme to obtain the focus surface estimates

$$z_k^{(a)} = \left( \sigma_k^{(a)} \right)^2 \sum_s \frac{z_k^{a,s}}{\left( \sigma_k^{a,s} \right)^2}, \quad (10)$$

with uncertainties

$$\sigma_k^{(a)} = \left[ \sum_s \frac{1}{\left( \sigma_k^{a,s} \right)^2} \right]^{-1/2}. \quad (11)$$

We present NIKA2 focus surfaces per arrays obtained as in Eq. 10 in Fig. 20. The three flavours of focus-estimators provide us with focus surfaces per arrays that are in good agreement with each others and that have a non-axisymmetrical flatten bowl shape consistent with expectations from simulation [TBA, as discussed further below]. The median defocus (that is the relative focus w.r.t. the center) across the detectors is about  $-0.1$  mm for the three arrays. Maximal defocus values of about  $-0.6$  mm are found for detectors located in the outer top and left regions of the FOV. Finally, a fraction comprised between 20 and 30% of the KIDs has a relative  $z \leq -0.2$  mm.

We primarily estimate the uncertainty of the focus surface measurements using the standard deviation between the three estimators  $z_k^{(a)}|_{\text{fwhm}}$ ,  $z_k^{(a)}|_{\text{peak}}$  and  $z_k^{(a)}|_{\text{flux}}$ . We found approximately homogeneous standard deviation surfaces per arrays, which have median values across the FOV of about 0.03 mm. However, we cross-check this error estimate by forming the quadratic mean of the three inverse-variance error surfaces per arrays, which are defined in Eq. 11 and quoted  $\sigma_k^{(a)}|_{\text{fwhm}}$ ,  $\sigma_k^{(a)}|_{\text{peak}}$  and  $\sigma_k^{(a)}|_{\text{flux}}$ . This provides us with more optimistic error surfaces per array, which do not show any clear pattern across the FOV and which have a median value across the detectors of about 0.015 mm.

*Stability across sequences.* By comparing the focus surface obtained from the five individual focus sequences, we test the stability of the NIKA2 focus surfaces across the time and the atmospheric conditions. In Figs. 21-22, we compare the defocus along two perpendicular diameters across the FOV. Although any direction would have been equivalent for this test, we choose to position the diameters along-with and perpendicular-to the KID geometrical grid to avoid the scatter due to KID non-alignement in any other direction. The scatter is further mitigated by considering four-detector-wide diameters as shown in upper the left corner of Figs. 21-22.

**add a sentence to conclude on the stability**

#### 6.1.4 Constraints on the X and Y foci

**add a description of the method**

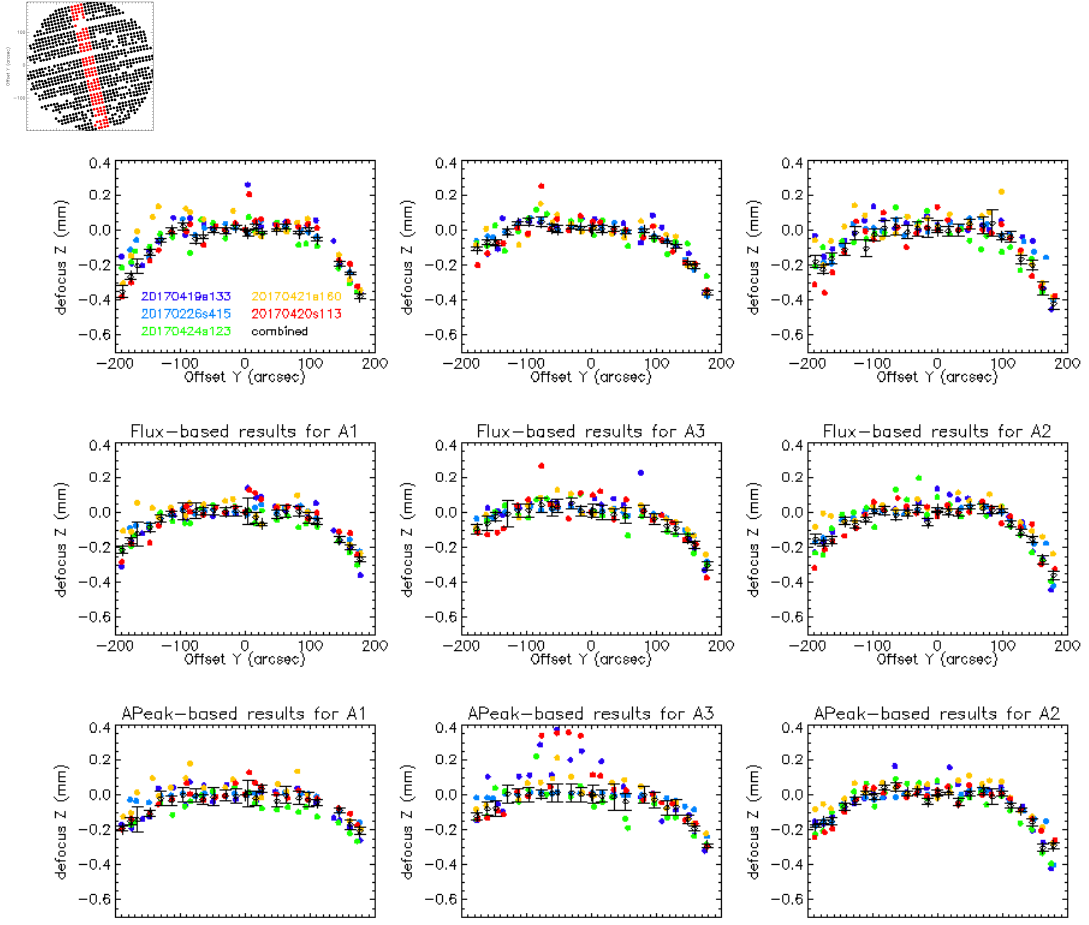


Figure 21: Stability of the focus surface across the sequences. This series of plot show the relative focus with respect to the center (defocus) along the ‘vertical diameter’, that is a band of four-detector width across the FOV, which is vertical with respect to the detector geometrical grid, as illustrated by the plot in the upper left corner. The datapoints show the defocus along the ‘vertical diameter’ estimated from the five focus sequences, namely 20170226s415–419 (sky blue), 20170419s133–137 (dark blue), 20170420s113–117 (red), 20170421s160–164 (yellow) and 20170424s123–127 (green), using the  $z^{(a)}|_{\text{fwhm}}$ ,  $z^{(a)}|_{\text{flux}}$  and  $z^{(a)}|_{\text{peak}}$  estimators from top to bottom, and for A1, A3 and A2 arrays from left to right. The black datapoints are the five-sequence combined defocus, as presented in Fig. 20, taken along the ‘vertical diameter’, and the errorbars, the five-sequence combined defocus errors along the ‘vertical diameter’.

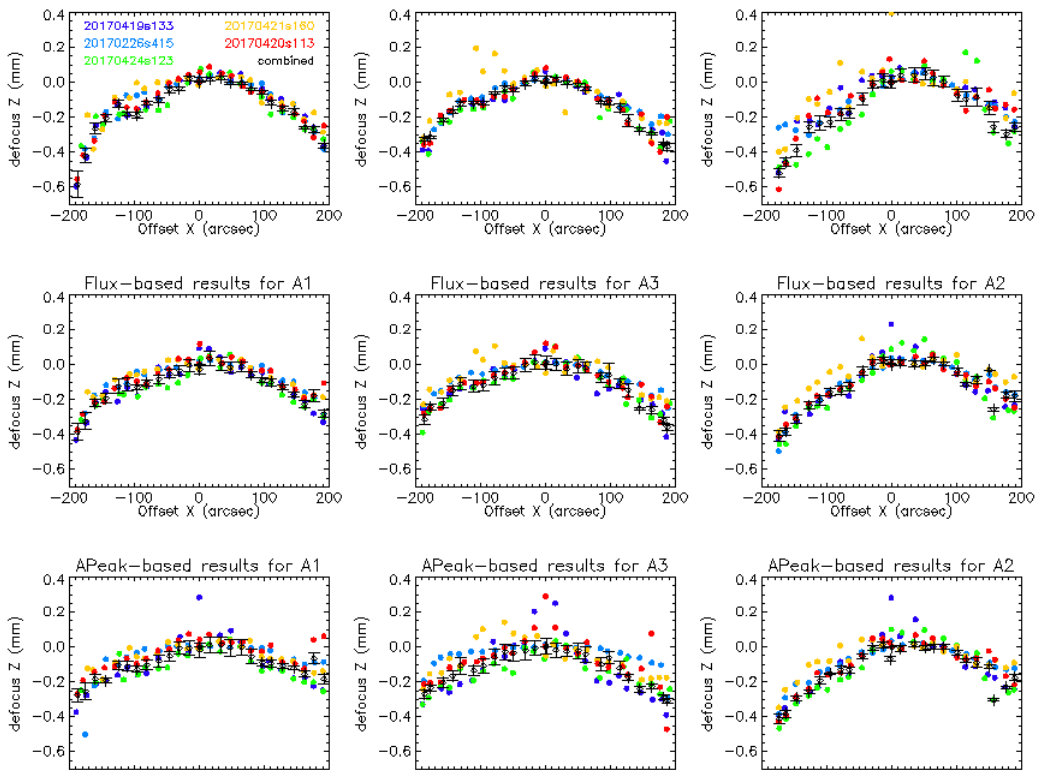


Figure 22: Stability of the focus surface across the sequences. Same legend as in Fig. 21, but for the detectors located in an ‘horizontal diameter’, i.e. a band of four-detector width across the FOV, which is horizontal with respect to the detector geometrical grid, as illustrated by the plot in the upper left corner.

## expand a little the discussion below

Very delicate measurements

The plan is to devote a few hours of technical observation time in good weather condition to perform an accurate measure of NIKA2 lateral focus. The X-, Y-focus will then be set at these robust estimated values and checked only a few times a year (at the seasonal change for example).

Figures 23 and 24 show examples of the lateral focus measurements performed during N2R9.

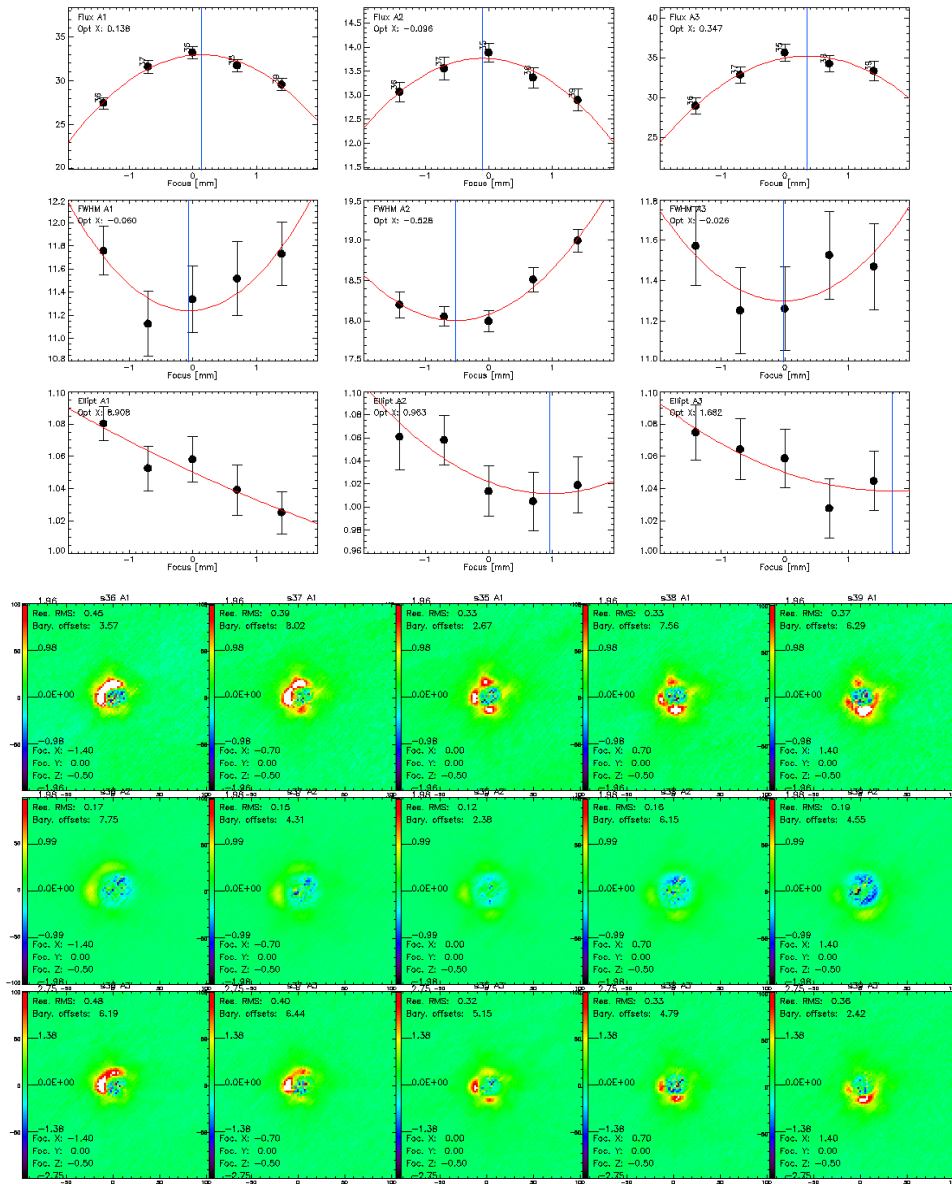


**Figure 23:** **Left:** X-focus measurement using a parabolic fit of the flux, beam fwhm and ellipticity on a sequence of five OTF scans on Uranus (20170223s39-43) **Right:** Beam residuals after subtracting a model of the main beam for each OTF-scan of the X-focus session.

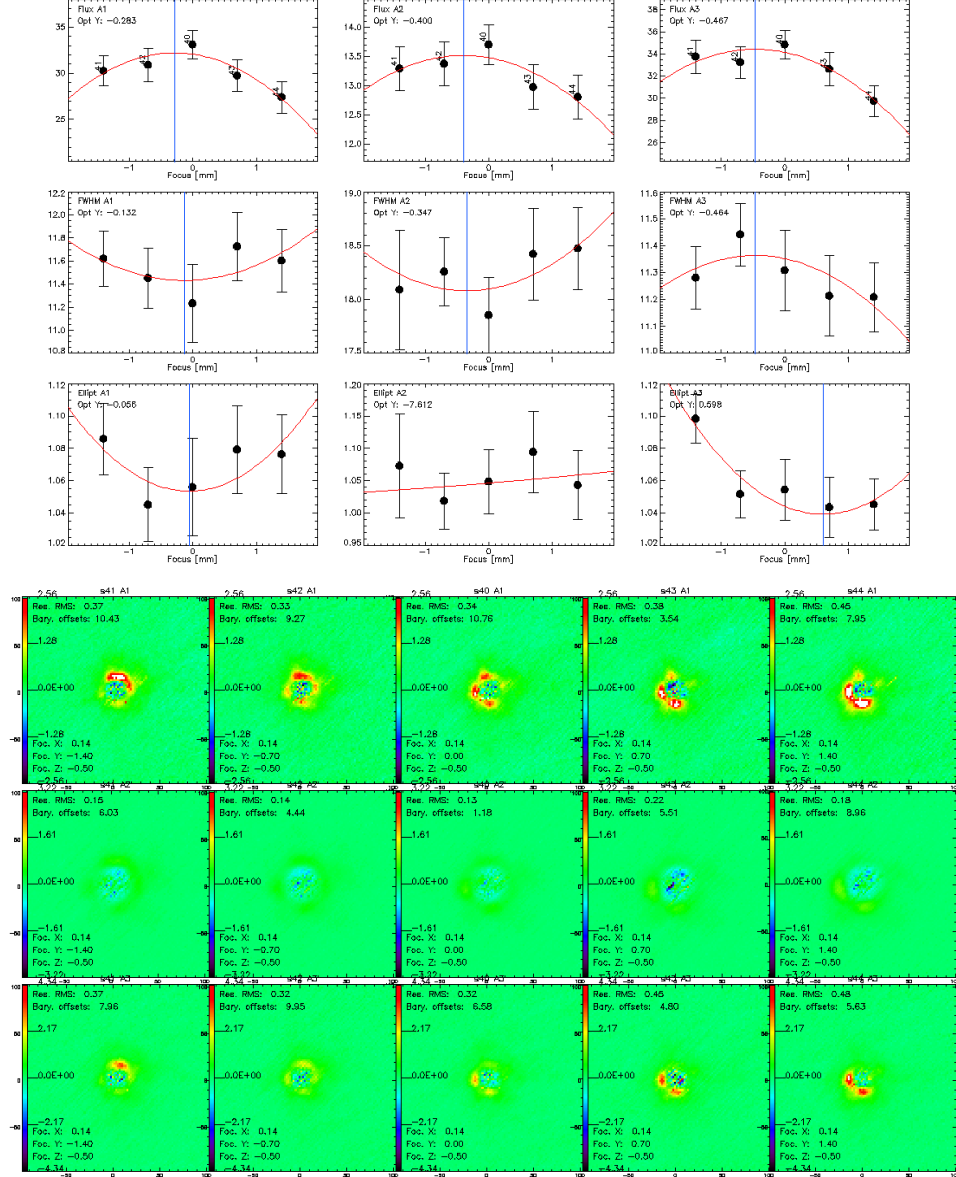


**Figure 24:** **Left:** Y-focus measurement using a parabolic fit of the flux, beam fwhm and ellipticity on a sequence of OTF scans on Uranus (20170223s44-48). **Right:** Beam residuals after subtracting a model of the main beam for each OTF-scan of the Y-focus session.

## 6.2 Full beam pattern

### 6.2.1 Data sets

The characterization of the IRAM 30-m beam pattern observed through NIKA2 detectors is mainly based on observations of strong compact sources, such as planets including Uranus, Neptune and Mars, and bright quasars. We generally use beam-map scans, which we recall, are deep-integration raster-scan observations that consist of 99 sub-scans placed at intervals of  $4.8''$  to cover a total of  $13.5' \times 7.8'$ . Most of our beam-related analysis are based on the

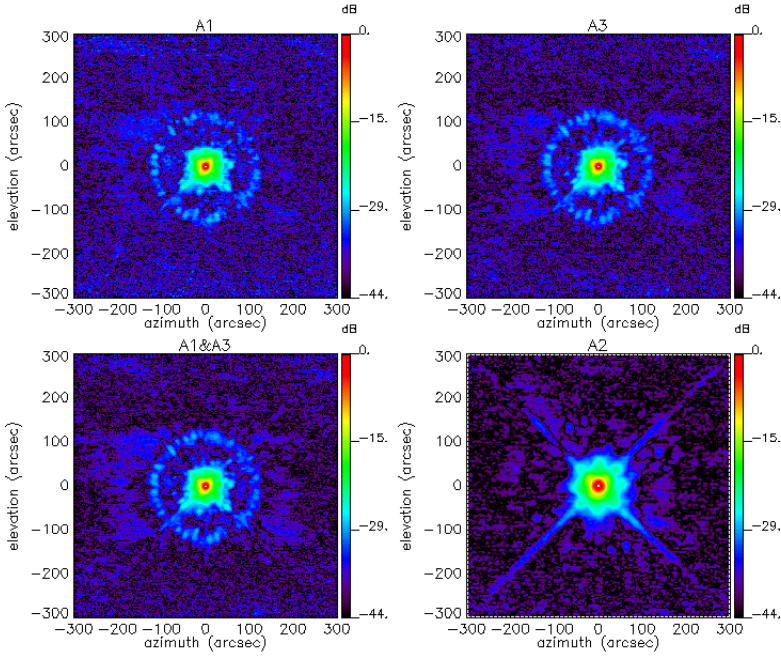


Figure 25: Beam pattern. From upper left to lower right, beam maps of array 1 (labeled 'A1'), array 3 ('A3'), the combination of the 1.15mm arrays ('A1&3') and the 2mm array ('A2') are shown in decibel. These maps, which consist of normalized combination of four long OTF scans of bright point sources, are in celestial coordinates and cover a sky area which extend over 10 arcmin.

same set of beam-map scans as previously selected to perform the average FOV reconstruction. The set comprises nine beam-map scans that distribute as one from N2R8, '20170125s243', two from N2R9, '20170224s177' and '20170226s415' and six from N2R10, which are '20170226s425', '20170227s84', '20170419s133', '20170420s113', '20170424s116', '20170424s123'.

### 6.2.2 Deep beam maps

We present the two-dimensional distribution of the beam in Fig. 25. We primarily use a map obtained from a combination of deep observations of strong point sources collected during NIKA2-*run8* and *run9*. Namely, we use 'beammap' OTF scans of Uranus (scan id '20170125s223' and '20170125s243'), Neptune ('20170224s177') and the bright quasar 3C84 ('20170226s415'). However, we checked the stability of our results on single scan maps, combinations of scans for a single source, and combinations of shallower scans but spanning a large range of scanning direction. The data processing includes a mitigation of the correlated noise, which mainly originates from the atmosphere. We primarily use a subtraction of a common mode estimated from the most correlated detectors (the so-called 'cm one block' method). However, other methods are tested for assessing the immunity of our results to noise residuals.

The deep NIKA2 beam maps reveal some noticeable features, which are shown in Fig. 26.

**Implement Samuel's comments copied below** Commentaires faits à Alessandro pour le papier:

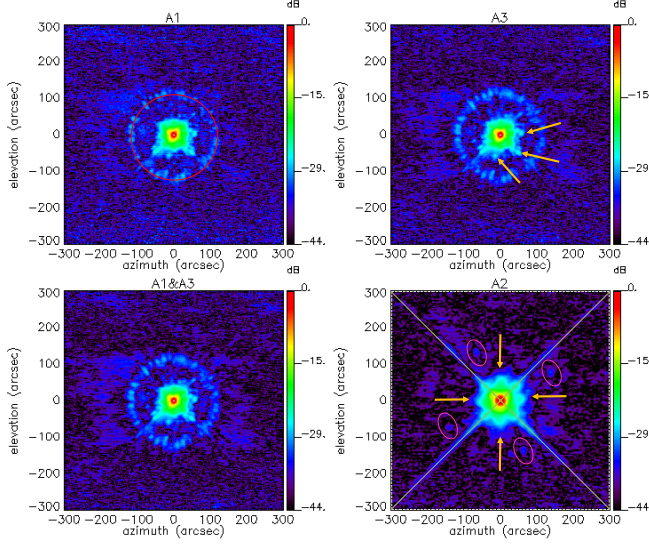


Figure 26: Noticeable features of NIKA2 beam pattern. Red circle: diffraction ring seen in 1-mm maps (the spokes are presumably caused by radial and azimuthal panel buckling (cf. Fig.4 in Greve et al. 2010)); Perpendicular green lines: diffraction pattern caused by quadrupod secondary support structure (prominently seen in 2mm maps); Yellow arrows in the upper right pannel: pattern of 3 spikes seen in 1mm maps of unknown origin; Yellow arrows in the lower right pannel: four symmetrical spokes of the first errorbeam; Pink ellipses: 4 spikes seen in 2mm maps.

- (1) les four symmetrical spokes of the error beam sont normaux et attendu d'après mes simus comme tu peux voir dans la petite image ci-dessous (c'est le beam obtenu dans Zemax pour la bande 1mm convolué avec une fonction porte de la taille du pixel)
- (2) par contre les pink ellipse show spikes in this map montrent un effet de diffraction ou de ghost image anormal et inattendu qui est du à un probleme optique dans le cryostat ou au niveau de M5 ou M6 ou la fenetre. On le sait car quand on regarde leur position en fonction de l'elevation on voit qu'ils tournent avec l'elevation dans les cartes Az-El
- (3) quant aux spikes of unknown origin montrés sur A3 je pense que les deux en bas et à droite sont juste un des petits lobes de la simu avec un meilleur contraste que ceux du haut et de gauche, alors que pour le petit blob dans la diagonale a peu pres au niveau de la diffraction sur un bras du quadrupode je soupçonne un effet d'amplification du a la petite boite qui se trouve sur le coté du secondaire que tu peux voir sur la photo du slide 2 de la présentation qu'Andrea a envoyée aujourd'hui (mais je n'ai pas de preuve)

To gain a first impression of the structure of the Iram 30-m beam as seen with NIKA2, we use radial cuts to evidence the relative level of the main beam, the first error beam and other features seen in the 2D beam pattern using radial cuts. NIKA2 full beam is shown in Fig. 27 by means of two orthogonal cuts through Uranus from a high quality map obtained on 2017 January 25th in excellent conditions (low opacity  $\tau_{225} = 0.08$  and elevation  $46^\circ$ ).

A model made of three Gaussians centered on the source peak was best fit *by hand* to these

cuts. We observe that the main beam starts to depart from the first Gaussian at the level of about -12dB for the three arrays. We note that for the instrument EMIR on the radiotelescope, this departure is about -20dB (Kramer, Penalver and Greve 2013). However, this discrepancy between a feedhorn-based experiment and a bare pixels one is expected since the main effect of the feedhorns is to lower the side lobes of the Airy diffraction pattern. The precise characterization of the full beam structure is discussed in Sect. 6.2.3.

### 6.2.3 Beam profile

**complete this sub-section**

The beam profile is the azimuthal average of the beam map around the main beam center. Although the profile cannot represent the sub-dominant non-axisymmetrical extended features, which are seen in the beam pattern and discussed in Sect. 6.2.2 (telescope arms, spikes), it provides us with a useful representation of the internal and central parts of the beam (about up to 100''). We determine a beam profile from a beam map in centering to the fitted value of the main beam center and forming the weighted average of the pixels equidistant to the center.

We model the beam profile as a three-Gaussian function defined as:

$$B(\theta) = \sum_i A_i G_i(\theta) + B_0 \quad (12)$$

Figure 28 shows the beam profile from a beam map acquired during N2R8 (scan ID: 20170125s223), as well as the best-fit 3-Gaussian model.

## 6.3 Main beam

We define NIKA2 main beam as the principal Gaussian (of the smaller FWHM) that encloses most of the measured source flux. The principal-power, smaller-FWHM Gaussian fitted function within the three-Gaussian model, as discussed in Sect. 6.2.3, provides us with a first estimate of the main beam, which is given in Table 6. However, this estimate could be biased toward the lower-FWHM values due to degeneracies between the three-Gaussian model parameters. To ensure obtaining robust main beam FWHM estimates, we devise two alternative dedicated methods, which both resort to masking the side lobes: i) Gaussian fits of the beam profile to benefit from the signal-over-noise increase after azimuthally averaging the signal, ii) Elliptical Gaussian fits of the beam map for a better 2D modeling. Cross-checking the outputs from these complementary methods is an important robustness test of our results.

We also consider different data sets acquired during N2R8, N2R9 and N2R10: i) a series of  $8' \times 5'$  OTF scans of primary and secondary calibrators, ii) beam-map scans of Planets.

Table 6 gathers the main beam FWHM results obtained using the three discussed methods and two datasets.

### 6.3.1 Sidelobe-masked Profile-based analysis

**add a description here [Jean-Francois's method]**

### 6.3.2 Sidelobe-masked Map-based analysis

**Method description** NIKA2 main beam two-dimensionnal distribution is modeled using an elliptical Gaussian. We characterize NIKA2 resolution by giving the *FWHM*, defined as

$$FWHM = 2\sqrt{2 \ln 2} \sqrt{\sigma_x \sigma_y}, \quad (13)$$

where  $\sigma_x$  and  $\sigma_y$  are the Gaussian standard deviation along minor- and major-axis. To avoid the side lobes contamination, we use masked versions of the beam map, in which an annulus of inner radius  $r_{in}$  and outer radius  $r_{out}$  is cut out. Whereas  $r_{out}$  is conservately set to be  $100\text{arcsec}$ ,  $r_{in}$  is let free to vary around a central value about  $8'$  for A1 and A3 and about  $12'$  for A2 to provide the best 2D Gaussian fit.

**Estimates using  $8' \times 5'$  OTF scans** We select N2R9 and N2R10  $8' \times 5'$  OTF scans of bright point sources, including primary and secondary calibrators. Namely, we consider scans of Uranus, Neptune, 3C273, 3C84, 0316+413, Vesta and MWC349, whereas we avoid CRL2688 and NGC7027, which are slightly extended. Conservative data selection criteria with respect to observing conditions are applied: average elevations  $el \geq 20$ , zenith opacities as estimated by NIKA2 in the 1mm band  $\tau_{1\text{mm}} \leq 0.4$ , reasonable lateral focus settings  $x, y \leq 0.5\text{mm}$ . After selection cuts, our data set includes 130 OTF scans acquired during N2R9, which consists of a representative sub-sample of a typical NIKA2 observation campaign, as well as XXX [TBC] scans of N2R10.

Figure 29 shows FWHM distributions obtained using the elliptical Gaussian fit method from the selected set of  $8' \times 5'$  OTF scans. We checked a posteriori that  $r_{in}$  distributes as  $7 \pm 1.5$  arcsec at 1mm and  $13 \pm 4$  arcsec at 2mm, in agreement with settings defined in the profile-based analysis.

**Estimates using beam-map scans** We use masked version of the beam maps, which are selected as described in Sect. 6.2.1. Sidelobe masks are defined by a fixed  $r_{out}$  of  $100\text{arcsec}$  and a  $r_{in}$  that freely varies from  $8'$  to  $9'$  for the 260 GHz-arrays, and from  $10'$  to  $14'$  for the 150 GHz array. We checked, hovewer, that we obtain consistent results but larger dispersion when using annulus masks of fixed  $r_{in}$  of  $8.5'$  and  $12'$  at 260 and 150 GHz respectively. The median main beam FWHM and the rms error estimate, which have been obtained from the nine beam-maps, are given in Table 6.

Table 6: FWHM of the NIKA2 main beam in arcsec.

Method	Dataset	Array or array combination			
		A1	A3	A1 & A3	A2
Three-Gaussian model G1 <sup>a</sup>	beam-map	$10.8 \pm 0.2$	$10.8 \pm 0.2$	$10.8 \pm 0.3$	$17.2 \pm 0.05$
Sidelobe-masked profile-based	TBD				
Sidelobe-masked map-based	OTF	$11.0 \pm 0.3$	$10.9 \pm 0.2$	$11.0 \pm 0.2$	$17.8 \pm 0.2$
	beam-map	$11.3 \pm 0.2$	$11.2 \pm 0.2$	$11.2 \pm 0.2$	$17.7 \pm 0.05$

<sup>(a)</sup> Median FWHM of the first (lowest-FWHM) Gaussian function within the Three-Gaussian model fitted from the beam-map scan selection

### 6.3.3 FWHM distribution across the FoV

Figure 30 shows the distribution of the main beam FWHMs of the arrays A1, A3 and A2 using a beammap scan of Neptune acquired during the April 2017 commissioning campaign and for average weather conditions (scan ID: 20170424s123). We also show in red the best Gaussian fit to histogram data. We find an average main beam FWHM of  $10.9''$  at 260 GHz and  $17.5''$  at 150 GHz in agreement with the main beam estimates gathered in Table 6. The observed dispersion of about  $0.6''$  is expected from the optics design and its associated field distortions across the 6.5 arc-minutes FoV, as discussed in Sect. 4.3. This quantifies the impact of the non-constant focus across the FoV, which is characterised in Sect. 6.1.3, on the individual detector main beams.

## 6.4 Beam efficiency

### discrepant results between methods

*method 1:*

$$\text{Eff} = \text{integral of the 2D Gaussian Main Beam} / \text{integral of the beam map}$$

*method 2:*

$$\text{Eff} = \text{integral of the 2D Gaussian Main Beam} / \text{integral of the measured profile}$$

*'Instru' Paper*

Comparing the 2D gaussian main beam fit to the full beam pattern measurement up to a radius of  $250''$ , we compute the beam efficiencies defined as the ratio of power between the main beam and this full beam. We find beam efficiencies  $\approx 55\%$  and  $\approx 75\%$  for the 260 and 150 GHz channels, respectively. Heterodyne observations of the lunar edge and of the forward beam efficiency derived from skydips show that a significant fraction of the full beam is received from beyond a radius of  $250''$ . This fraction is not considered here.

The beam efficiency estimates for the three arrays and the 1mm-array combination are given in Table 7.

Table 7: Beam efficiency

Method	Array or array combination			
	A1	A3	A1 & A3	A2
2D elliptical-over-deep map beam <sup>a</sup>	$0.75 \pm 0.07$	$0.69 \pm 0.04$	$0.73 \pm 0.06$	$0.85 \pm 0.05$
2D elliptical-over-measured profile <sup>a</sup>	$0.63 \pm 0.10$	$0.56 \pm 0.05$	$0.58 \pm 0.06$	$0.79 \pm 0.06$
$250''$ estimates <sup>b</sup>	0.55	0.55	0.55	0.75

<sup>(a)</sup> Laurence's study

<sup>(b)</sup> values reported in the 'Instrument' paper

## 6.5 Stability of the beam pattern

### 6.5.1 Individual scan beam profiles

We checked the stability of the beam against various observing condition (source intensity, weather condition, focus optimisation) by comparing the beam profile of the beam-map set, which comprises nine beam-maps acquired from N2R8 to N2R10, as defined in Sect. 6.2.1. The nine beam profiles and their ratio w.r.t. the median beam profile are shown in Fig. 31.

### **6.5.2 Main beam FWHM stability**

[A FAIRE:

AJOUTER LES PLOTS DE STABILITE EN FONCTION DE ELEVATION, TAU  
]

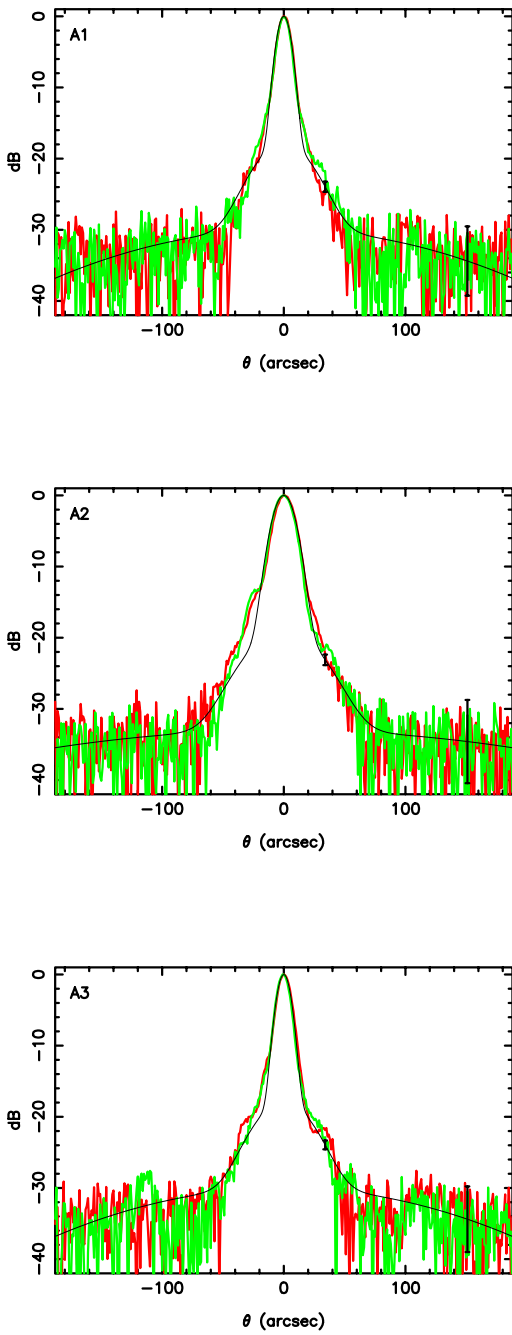


Figure 27: Two orthogonal cuts through the beam are shown in red and green and a best fit model made of three Gaussians is superimposed in black. These cuts were obtained from the high quality map of Uranus on 2017 January 25th. The main beam starts to depart from the first Gaussian at -12dB.

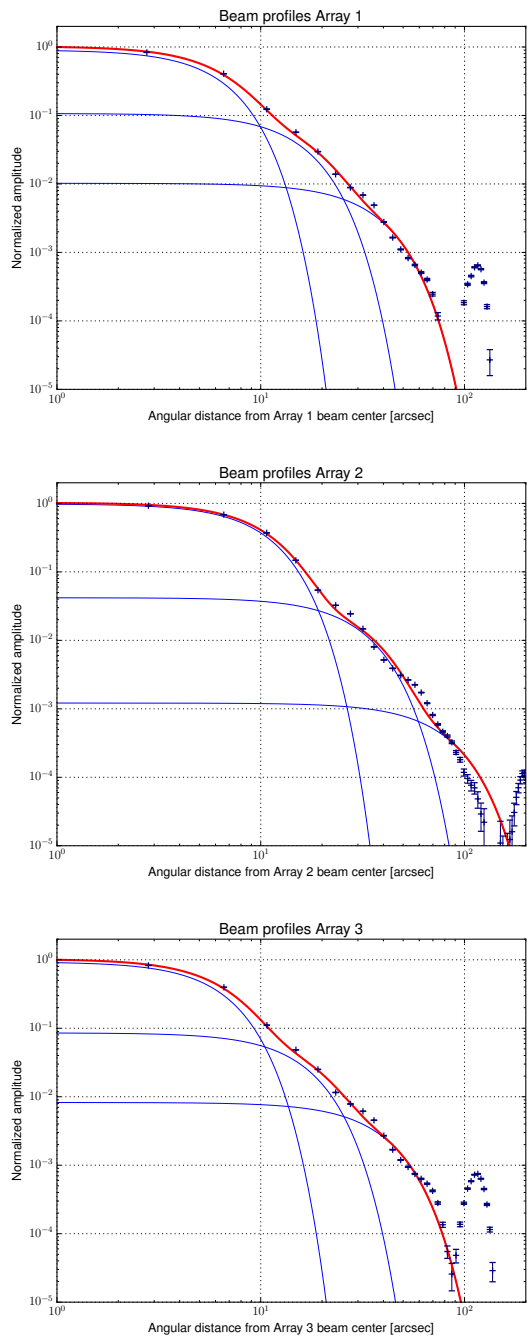


Figure 28: Beam profiles for array 1, 2, and 3.

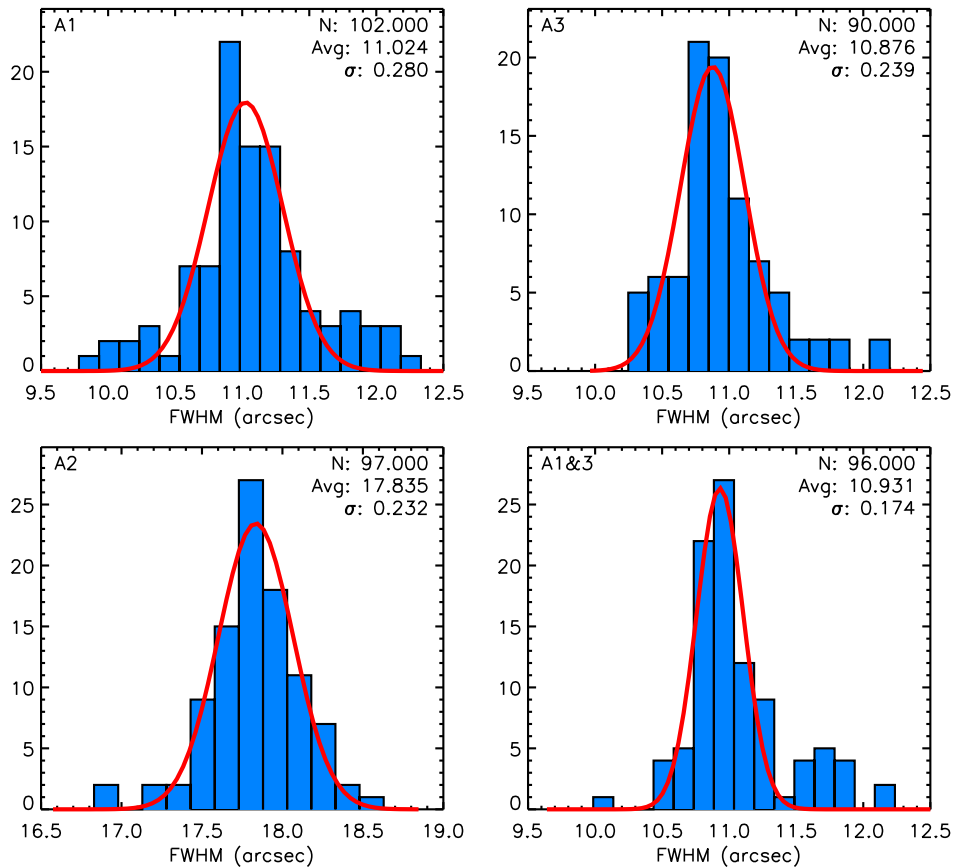


Figure 29: Distribution of the main beam FWHM estimates using 2D Gaussian fits on N2R9 and N2R10  $8' \times 5'$  OTF scans of bright point sources

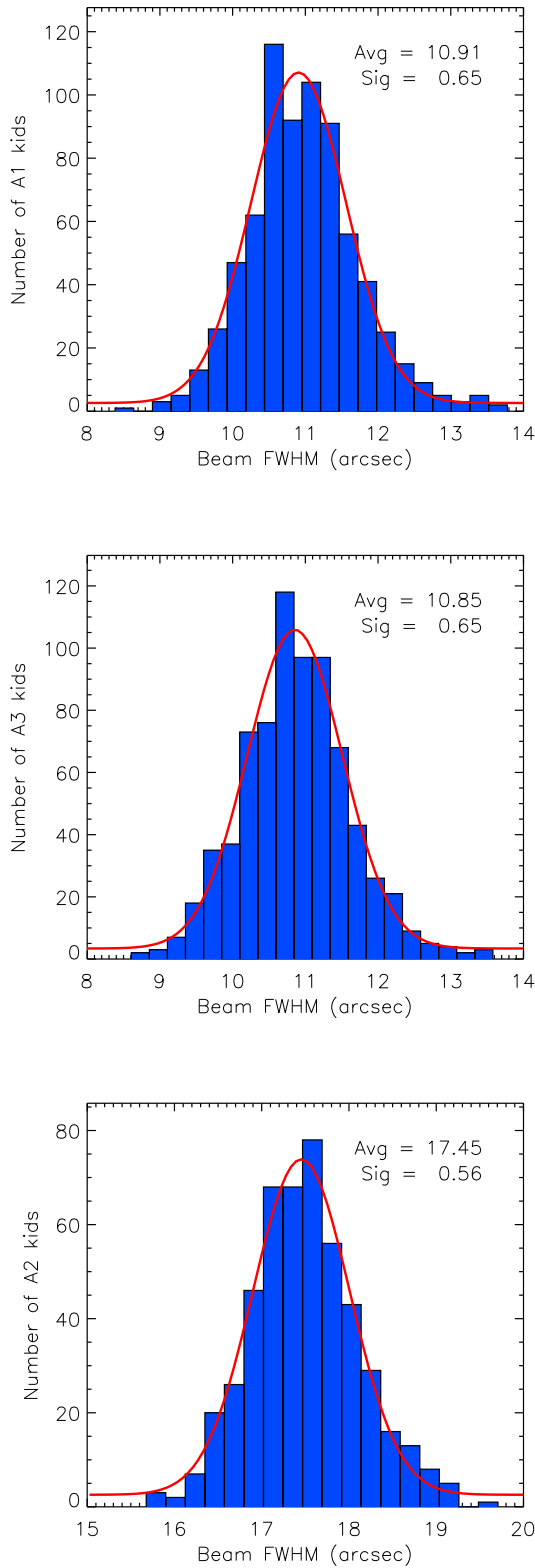


Figure 30: From top to bottom, main beam FWHM distribution of all valid KID detectors of arrays A1, A3, and A2. The main beam FWHM is the geometrical combination of the two-orthogonal FWHM estimates obtained from an elliptical Gaussian fit on side-lobe masked individual maps per KID (see text). The red curves show a Gaussian fit to the histogram data.

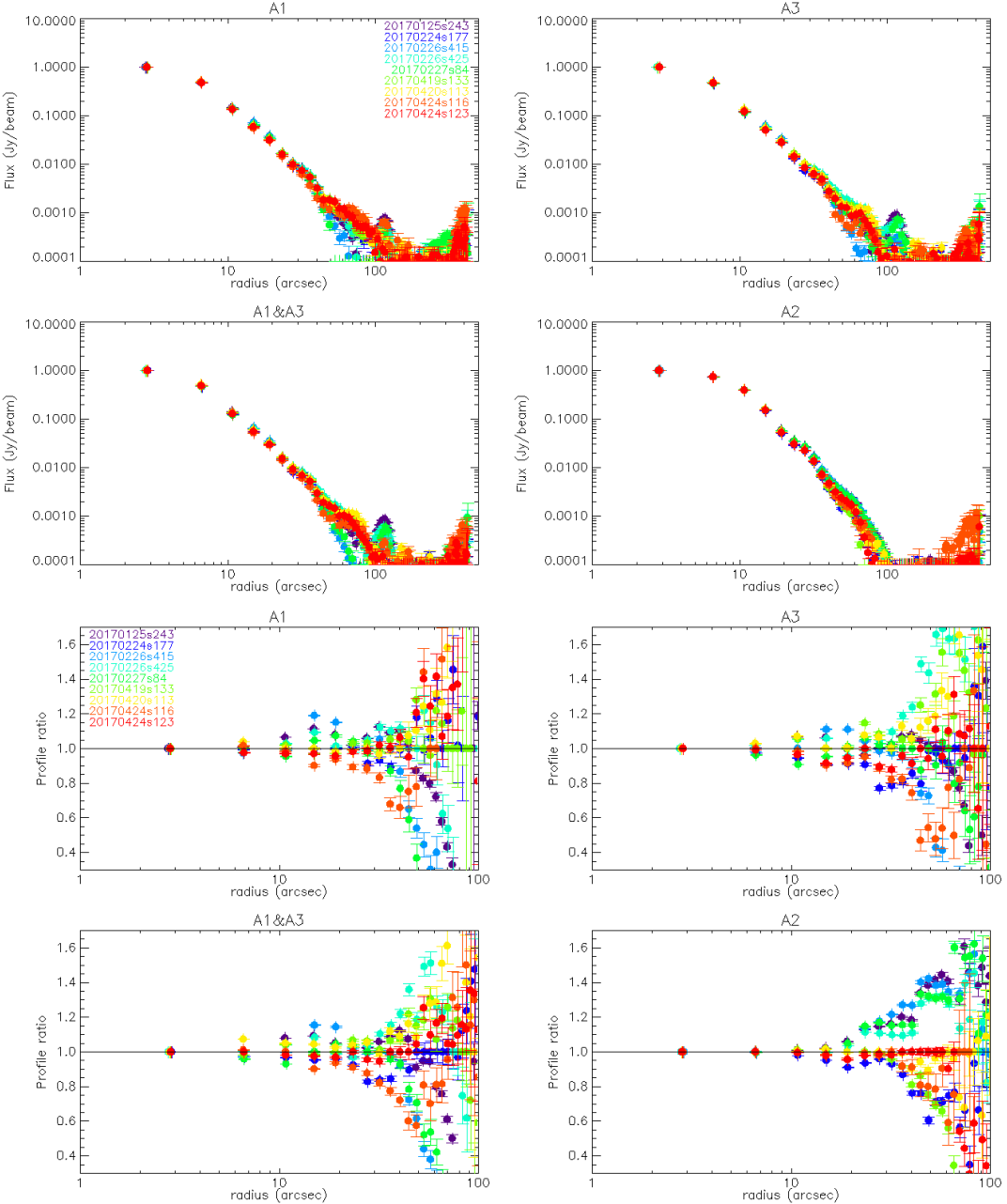


Figure 31: Stability of the beam profile across various N2R8 to N2R10 beam-map scans. The upper panel shows the beam profiles normalised to the maximum value, and the lower panel the ratios w.r.t. the median profile.

## 7 Calibration

The calibration of the NIKA2 instrument in its final configuration of January 24th 2017 is studied in this section in using the primary calibrators, Uranus and Neptune, and secondary calibrators (planetary nebulae NGC7027, CRL2688, and MWC349A). Planer Mars and the two largest asteroids Ceres and Vesta were also observed.

### 7.1 NIKA2 Photometric System

	1 mm	2 mm
Reference frequency $\nu_0$	260 GHz	150 GHz
Reference FWHM	12.5 "	18.5 "

Table 8: NIKA2 reference frequencies and FWHM

#### 7.1.1 Response of a detector to astronomical source

**FM: airmass was  $x$  in previous section, and elevation was  $\delta$ . we have to choose among these various notations**

Let us consider a source observed at airmass  $\sec z$  under  $mm_{H_2O}$  of precipitable water, with specific intensity  $I_\nu$  (in units of  $W/m^2/sr/Hz$ ) in the direction  $\theta, \phi$ , where  $\theta$  is the off-axis distance and  $\phi$  the position angle, illuminating a KID of the NIKA2 array.

A KID response located at position  $\theta, \phi$  on the focal plane to this signal will be:

$$R(\theta, \phi, \sec z, mm_{H_2O}) = G_k \int_0^{+\infty} I(\nu) \frac{T'(\nu)}{\left(\frac{\nu}{\nu_0}\right)^2} e^{-\sec z \cdot \tau(\nu, mm_{H_2O})} A\Omega(\nu) d\nu \quad (14)$$

**FM: if  $k$  is the kid number, then it should be  $R_k$**

where the different factors in the integral are:

- $\frac{T'(\nu)}{\left(\frac{\nu}{\nu_0}\right)^2}$ : the system transmission.  $T'(\nu)$  is the transmission as measured in section 2 with a Rayleigh-Jeans source. It is divided by  $\left(\frac{\nu}{\nu_0}\right)^2$  to correct for the incident spectrum.

**FM: in section 2, we define  $T$  note  $T'$**

- $e^{-\sec z \cdot \tau(\nu, mm_{H_2O})}$ : the atmospheric transmission at airmass  $\sec z$  for an amount of precipitable water vapor  $mm_{H_2O}$  generating an opacity  $\tau(\nu)$ .
- $A\Omega(\nu)$ : the KID etendue **FM: extent ? etendue is not english as far as i know, i. e.** the product of its light collecting area by the solid angle it intercepts on the sky. While the step between pixels is well known and is measured (see sec 4.1), the actual solid angle is not known precisely and is *probably* a function of the frequency because the pixels sizes are close to the wavelength of operation (2.75 mm at 2 mm for example). The collecting  $A$  area is the projection of the IRAM primary on the cold pupil and is also not known very accurately.

The integral in eq 14 gives the total power (units of W) falling on a pixel. The factor  $G_k$  (units of  $\text{W}^{-1}$ ) converts this power to ADU. **FM: ADU ?**

By virtue of the conservation of specific intensity in a telescope, equation 14 can be rewritten as:

$$R(\theta, \phi, \sec z, mm_{H_2O}) = G_k A_p \Omega_s \int_0^{+\infty} I(\nu) \frac{T'(\nu)}{\left(\frac{\nu}{\nu_0}\right)^2} e^{(-\sec z \cdot \tau(\nu, mm_{H_2O}))} \Omega_b(\theta, \phi, \nu) d\nu \quad (15)$$

where:

- $A_p$  is the area of the entrance pupil (*i.e.* the dish collecting area).
- $\Omega_s$  is the solid angle of the source seen from the entrance pupil.
- $\Omega_b(\theta, \phi, \nu)$  is the fraction of source signal illuminating the KID. It is thus normalized so that:

$$\int \int_{4\pi} \Omega_b(\theta, \phi, \nu) \sin \theta d\theta d\phi = 1 \quad (16)$$

Equation 15 describes the response of a KID, and is quite complex. We will in the following simplify it by making a few assumptions. Let us first turn ourselves toward the effect of the atmosphere.

### 7.1.2 Effect of the atmosphere

In order to study the effects of the atmosphere, let us define the effective frequency of a source as the weighted frequency of the passband, taking into account the system and atmospheric transmission, as well as the shape of the incident spectrum:

$$\nu_{eff}(\sec z, mm_{H_2O}) = \frac{\int_0^{+\infty} I(\nu) \frac{T'(\nu)}{\left(\frac{\nu}{\nu_0}\right)^2} e^{(-\sec z \cdot \tau(\nu, mm_{H_2O}))} \nu d\nu}{\int_0^{+\infty} I(\nu) \frac{T'(\nu)}{\left(\frac{\nu}{\nu_0}\right)^2} e^{(-\sec z \cdot \tau(\nu, mm_{H_2O}))} d\nu} \quad (17)$$

**FM: already defined in eq 1...**

In order to compute the atmospheric transmission, we have used the IRAM atmosphere 2009 models provided in GILDAS, computed for so called *midlatwinter* conditions, a temperature of 268 K and a pressure of 703.5 hPa.  $\nu_{eff}$  allows us to characterise the impact of the variation of the atmospheric transmission on the full system transmission. Note that the instrument transmission  $T'(\nu)$  is the one measured in sec 2.

**FM: but we called it  $T$ ...**

Figure 32 shows the variations of  $\nu_{eff}$  as a function of the water content of the atmosphere for two elevations (zenith and 20 degree) and two spectral shape (RJ and flat spectrum), in the two 1mm passbands and in the 2mm passband.

Typical variations of  $\nu_{eff}$  with the spectral shape of the source range between 1% and 3%, and are relatively stable between good ( $\tau_{225GHz} \simeq 0.1$ ) and poor ( $\tau_{225GHz} \simeq 1.0$ ) atmospheric conditions for both the 1mm and 2mm bands. Let us now examine the effect of elevation. Under good atmospheric conditions ( $\tau_{225GHz} \simeq 0.1$ ),  $\nu_{eff}$  changes by less than 0.3% between zenith and 20 degree elevation. Under poor conditions ( $\tau_{225GHz} \simeq 1.0$ ), this rises to almost 3% for a

Rayleigh-Jeans spectrum in the 2 mm band, *i.e.* larger than the variations due to the spectral shape of the source.

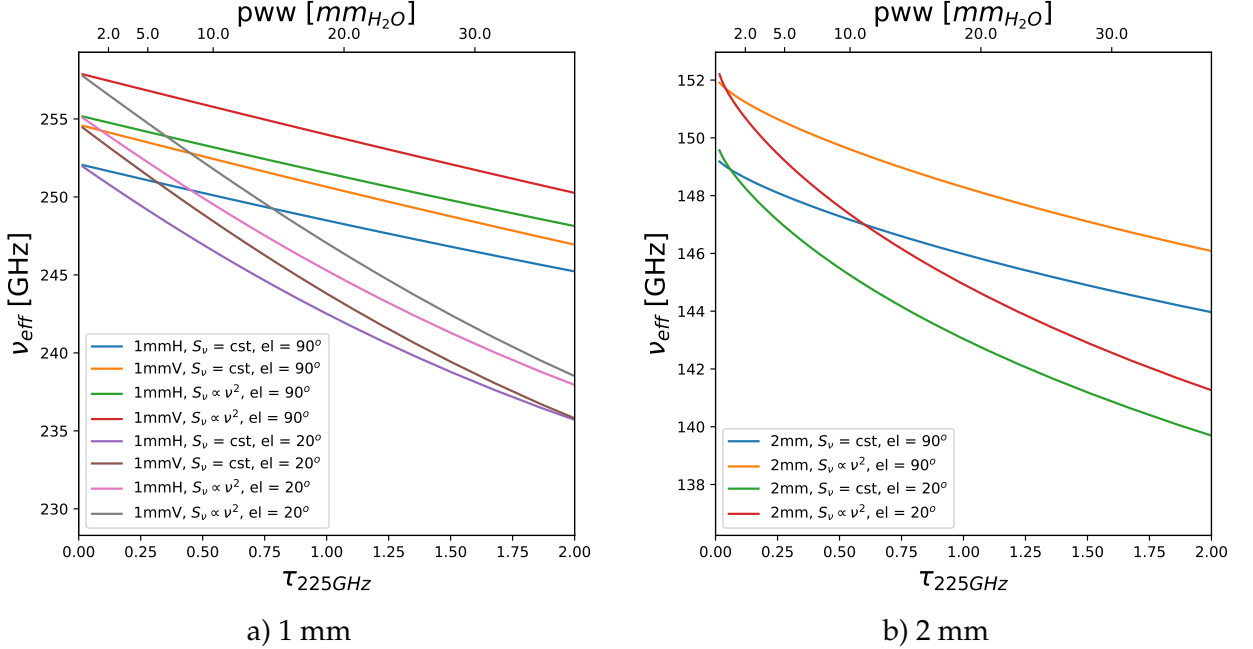


Figure 32: Effective frequency as a function of the sky opacity. The effective frequency (see text) have been computed for two source spectra (RJ and constant), and for two elevations.

Nevertheless, to a first approximation, we consider the shape of the atmospheric transmission independent of the elevation and water content, so that an effective zenith opacity  $\tau_{eff}$  used. Equation 15 becomes under this assumption:

$$R(\theta, \phi, \sec z, mm_{H_2O}) \simeq G_k A_p \Omega_s e^{(-\sec z \cdot \tau_{eff}(mm_{H_2O}))} \int_0^{+\infty} I(\nu) \frac{T'(\nu)}{\left(\frac{\nu}{\nu_0}\right)^2} T_{atm}(\nu) \Omega_b(\theta, \phi, \nu) d\nu \quad (18)$$

where  $T_{atm}(\nu)$  is the transmission of the atmosphere at zenith, and is a function of the frequency only. From the computations made to plot figure 32, we derive that this approximation is valid below the percent level for  $\tau_{225GHz} < 0.35$

The dependance on elevation and opacity can be corrected as shown in section 3, so that a response outside of atmosphere (in terms of airmass, but not in terms of transmission) can be derived:

$$R(\theta, \phi) \simeq G_k A_p \Omega_s \int_0^{+\infty} I(\nu) \frac{T'(\nu)}{\left(\frac{\nu}{\nu_0}\right)^2} T_{atm}(\nu) \Omega_b(\theta, \phi, \nu) d\nu \quad (19)$$

Equation 19 is the main photometric equation.

Because both  $A_p$  and  $\Omega_b$  are not known with good accuracy, it is not possible to compute all the terms of eq. 19 from first principles, and a practical way of calibrating the system must be used: it is done by observing a primary calibrator.

### 7.1.3 Beammap of a calibrator

A primary calibrator is a source whose spectral irradiance is known. For NIKA2, we use two planets as primary calibrators, Uranus and Neptune.

The specific intensity  $I_c(\nu)$  of the calibrator is:

$$I_c(\nu) = \frac{S_c(\nu)}{\Omega_s} = \frac{S_c(\nu_0)}{\Omega_S} f\left(\frac{\nu}{\nu_0}\right) \quad (20)$$

Where  $S_c(\nu)$  is the spectral irradiance of the calibrator (units of  $\text{W/m}^2/\text{Hz}$ ) or Jy. We parametrize the source spectral irradiance as a function of a reference frequency  $\nu_0$  that we choose arbitrarily to be:  $\nu_0 = 150 \text{ GHz}$  for the 2mm array and  $\nu_0 = 260 \text{ GHz}$  for both 1mm arrays.

Equation 19 becomes:

$$R(\theta, \phi) \simeq G_k A_p S_c(\nu_0) \int_0^{+\infty} f\left(\frac{\nu}{\nu_0}\right) \frac{T'(\nu)}{\left(\frac{\nu}{\nu_0}\right)^2} T_{atm}(\nu) \Omega_b(\theta, \phi, \nu) d\nu \quad (21)$$

Let further parametrize the beam as a function of the effective frequency as defined in eq 17, considering that its frequency dependency is only due to the diffraction law, hence a variation as  $1/\nu$ .

With this in hand, we can write the equation of a beammap using a single KID with eq 18. At each position  $(\theta, \phi)$  on the beam map we have:

$$R_c(\theta, \phi) = G_k A_p S_c(\nu_0) \int_0^{+\infty} f\left(\frac{\nu}{\nu_0}\right) \Omega_b(\nu_0, \theta \times \frac{\nu}{\nu_0}, \phi) \frac{T'(\nu)}{\left(\frac{\nu}{\nu_0}\right)^2} T_{atm}(\nu) d\nu \quad (22)$$

### 7.1.4 Calibration in $\text{FWHM}_0$ beam

This map is fitted with a gaussian of fixed width:  $\text{FWHM}_0$  (we recall that  $2\sqrt{2\ln 2}\sigma_0 = \text{FWHM}_0$ ).

$$R_c(\theta, \phi) = \frac{A_c}{2\pi\sigma_0^2} e^{-\frac{\theta^2}{2\sigma_0^2}} + \epsilon(\theta, \phi) \quad (23)$$

where  $\epsilon(\theta, \phi)$  are the residuals of the fit.

Assuming that the fit is not biased, we have:

$$\int \int R_c(\theta, \phi) \sin \theta d\theta d\phi = A_c \quad (24)$$

because errors average out so that:

$$\int \int \epsilon(\theta, \phi) \sin \theta d\theta d\phi = 0 \quad (25)$$

But we also know that integral of the beammap should give the power emitted by the source. Therefore, we form the map:

$$M_c(\theta, \phi) = R_c(\theta, \phi) S_c(\nu_0) / A_c \quad (26)$$

where  $S_c(\nu_0)$  is the spectral irradiance of the calibrator at a reference frequency  $\nu_0$  given in table 7.1. This map has units of  $\text{W/m}^2/\text{Hz}$ . Note that the choice of the reference frequency is arbitrary, it is a convention. By construction, integrating over the map we have:

$$\int \int M_c(\theta, \phi) \sin \theta d\theta d\phi = S_c(\nu_0) \quad (27)$$

Similarly, a point source with spectral irradiance  $S_s(\nu)$  will generate a response at position  $(\theta, \phi)$

$$R_s(\theta, \phi) = G_k A_p \int_0^{+\infty} S_s(\nu) \Omega_b(\nu_0, \theta \times \frac{\nu}{\nu_0}, \phi) \frac{T'(\nu)}{\left(\frac{\nu}{\nu_0}\right)^2} T_{atm}(\nu) d\nu \quad (28)$$

Note here that the effective frequency for the beam is not necessarily the same as the one for the primary calibrator, as it depends on the source spectrum.

This beammap will be fitted with a gaussian of fixed width:

$$R_s(\theta, \phi) = \frac{A_s}{2\pi\sigma_o^2} e^{-\frac{\theta^2}{2\sigma_o^2}} + \epsilon(\theta, \phi) \quad (29)$$

The quoted flux for the source is then:

$$S_q(\nu_0) = S_c(\nu_0) \times \frac{A_s}{A_c} \quad (30)$$

In other words, the quoted flux is the flux that should have the calibrator in order to generate a response that would be fitted with a gaussian of fixed width and the same amplitude as the source. Let us form the map:

$$M_s(\theta, \phi) = R_s(\theta, \phi) S_c(\nu_0) / A_c \quad (31)$$

*The map  $M_{\theta, \phi}$  is said to be calibrated in Jy / FWHM<sub>0</sub> beam.*

If we have a single point source in M, we have when we fit a gaussian of fixed width:

$$\int \int M_s(\theta, \phi) \sin \theta d\theta d\phi = A_s S_c(\nu_0) / A_c = S_q(\nu_0) \quad (32)$$

Note that the quoted flux is not the flux of the source at the reference frequency. In order to find the flux of the source at the reference frequency, a color correction has to be applied

$$S_s(\nu_0) = S_q(\nu_0) C_s \quad (33)$$

### 7.1.5 Color correction for point sources measured with fixed gaussian fit

When a source is measured

$$C_s = S_s(\nu_0) / S_q(\nu_0) = S_s(\nu_0) / S_c(\nu_0) \times \frac{A_c}{A_s} \quad (34)$$

$$C_s = S_s(\nu_0) / S_c(\nu_0) \times \frac{\int \int R_c(\theta, \phi) \sin \theta d\theta d\phi}{\int \int R_s(\theta, \phi) \sin \theta d\theta d\phi} \quad (35)$$

$$C_s = S_s(\nu_0) / S_c(\nu_0) \times \frac{\int \int G_k A_p S_c(\nu_0) \int_0^{+\infty} f\left(\frac{\nu}{\nu_0}\right) \Omega_b(\nu_0, \theta \times \frac{\nu}{\nu_0}, \phi) \frac{T'(\nu)}{\left(\frac{\nu}{\nu_0}\right)^2} T_{atm}(\nu) d\nu \sin \theta d\theta d\phi}{\int \int G_k A_p \int_0^{+\infty} S_s(\nu) \Omega_b(\nu_0, \theta \times \frac{\nu}{\nu_0}, \phi) \frac{T'(\nu)}{\left(\frac{\nu}{\nu_0}\right)^2} T_{atm}(\nu) d\nu \sin \theta d\theta d\phi} \quad (36)$$

which simplifies into:

$$C_s = S_s(\nu_0) \times \frac{\int_0^{+\infty} f\left(\frac{\nu}{\nu_0}\right) \int \int \Omega_b(\nu_0, \theta \times \frac{\nu}{\nu_0}, \phi) \sin \theta d\theta d\phi \frac{T'(\nu)}{\left(\frac{\nu}{\nu_0}\right)^2} T_{atm}(\nu) d\nu}{\int_0^{+\infty} S_s(\nu) \int \int \Omega_b(\nu_0, \theta \times \frac{\nu}{\nu_0}, \phi) \sin \theta d\theta d\phi \frac{T'(\nu)}{\left(\frac{\nu}{\nu_0}\right)^2} T_{atm}(\nu) d\nu} \quad (37)$$

We have:

$$\int \int \Omega_b(\nu_0, \theta \times \frac{\nu}{\nu_0}, \phi) \sin \theta d\theta d\phi = 1 \quad (38)$$

So that:

$$C_s = S_s(\nu_0) \times \frac{\int_0^{+\infty} f\left(\frac{\nu}{\nu_0}\right) \frac{T'(\nu)}{\left(\frac{\nu}{\nu_0}\right)^2} T_{atm}(\nu) d\nu}{\int_0^{+\infty} S_s(\nu) \frac{T'(\nu)}{\left(\frac{\nu}{\nu_0}\right)^2} T_{atm}(\nu) d\nu} \quad (39)$$

### 7.1.6 Calibration for aperture photometry

For aperture photometry, the map calibrated in Jy /  $FWHM_0$  must be converted in a map in Jy / pixel.

### 7.1.7 Calibration in surface brightness

## 7.2 Reference flux densities of the calibrators

The two main calibrators of NIKA2 are the giant planets Uranus and Neptune. Mars can also be used as primary calibrator, but care must be taken to use a flux corresponding to the date of the observations. Secondary calibrators were also observed during the commissioning campaign.

### 7.2.1 Uranus and Neptune

For the flux densities of the giant planets, we use the ESA model from [10]: Version 5 for Neptune and Version 4 for Uranus. Both models provide the planet brightness temperature in the Rayleigh-Jeans approximation as a function of the frequency. The resulting flux is therefore:

$$S_\nu = \Omega \times \frac{2\nu^2 k T_{RJ}}{c^2} \quad (40)$$

where  $\Omega$  is the solid angle of the planet on the sky. Following Bendo et al. (2013) REF and correcting their equation 12 we have:

$$\Omega = \pi \frac{r_e r_{p-a}}{D^2} \quad (41)$$

where  $r_e$  is the equatorial radius of the planet and  $r_{p-a}$  is its apparent polar radius, and  $D$  the distance to the planet.  $r_{p-a}$  can be computed from the sub-observer latitude  $\phi$  (e.g. the latitude of the observed ? as seen from the planet in the planet equatorial reference frame) and  $r_p$  the polar radius of the planet as:

$$r_{p-a} = \sqrt{r_p^2 \cos^2 \phi + r_e^2 \sin^2 \phi} \quad (42)$$

	Uranus	Neptune
$r_e$ [km]	25559	24764
$r_p$ [km]	24973	24341
$\phi$	Ob-lat	Ob-lat
$D$ [AU]	delta	delta

Table 9: Physical quantities used for the Uranus and Neptune fluxes computation (equation 41. Ob-lat and delta are quantities tabulated by NASA Horizons system [9] as a function of the date

All quantities to compute the planet flux are obtained from the NASA Horizons web site [9], and are listed in table 9. To compute the planet fluxes for a given date, we use the python photometry package available at [8].

The model spectra are linearly interpolated in log space at the reference frequencies of the NIKA2 bandpasses. Fluxes for all NIKA2 calibration runs are listed in table 10, together with the expected variation between the start and end of a run.

The Uranus and Neptune models have been compared to Planck observations of these planets [7]. For Uranus, the model used in the comparison is the ESA V2, and it is found to overpredict by 4 K (about 4%) the observed RJ temperature at 143 GHz, to agree at 217 GHz, and to underpredict at 353 GHz. We use for NIKA2 calibration ESA model V4, that predict a flux respectively -3.3%, 0.3% and 4.7% higher in the the 143, 217 and 353 GHz, that would lead to a percent accuracy with respect to Planck observations.

For Neptune, the same study compared Planck observation with the ESA V5 model, *i. e.* the same one used for NIKA2 calibration. For this planet, temperatures are found to disagree at most by 5 K, *i.e.* 4.1%, with the same trend with frequency as observed for Uranus. All thing considered, this study confirm that Uranus ESA V4 and Neptune ESA V5 models are accurate to 5% for predicting planet fluxes. Calibration values tabulated in table ?? show that the variations of Uranus and Neptune over the duration of a typical NIKA2 run are negligible compared to the model accuracy. On the other hand, not taking into account the planet shape and orientation with respect to the observer in the computations of its solid angle can lead to errors between 1 and 2% as illustrated in the Python notebook [6] distributed with the software.

### 7.2.2 Mars

For Mars, we use the model of Belloche & Amri (2006) available at [5], with default parameters. Model output is computed at the two reference frequencies of NIKA2, 150 and 260 GHz.

Fluxes of Mars are tabulated in table 10. In many cases, the variations of Mars flux during the course of a run are larger than the model uncertainty (5%), and should be recomputed at more frequent times.

#### FM: conclusion for Mars ?

### 7.2.3 Secondary calibrators

The secondary calibrator MWC349A is a young Be star, part of a stellar binary system, surrounded by a disk. Its radio continuum emission originates in an ionized bipolar outflow [4].

NR <sup>a</sup>	JD <sup>b</sup>	$\Delta t$ <sup>c</sup>	$S_\nu(260 \text{ GHz})$ <sup>d</sup>	$S_\nu(150 \text{ GHz})$ <sup>e</sup>	$\Delta S_\nu / S_\nu^f$
	d	d	Jy	Jy	%
Uranus					
13	2457330.5	12	45.59	17.65	-0.89
14	2457354.5	8	44.44	17.21	-1.07
15	2457409.5	20	40.62	15.73	-3.22
16	2457455.5	14	38.27	14.82	-1.16
18	2457660.0	25	46.06	17.83	+1.25
19	2457690.0	7	46.09	17.85	-0.32
20	2457732.0	7	44.14	17.09	-1.04
21	2457764.5	4	41.82	16.19	-0.69
22	2457809.0	7	39.08	15.13	-0.83
23	2457865.0	7	37.96	14.70	+0.14
24	2457915.4	5	39.49	15.29	+0.66
Neptune					
13	2457330.5	12	17.09	7.18	-1.26
14	2457354.5	8	16.64	6.99	-0.92
15	2457409.5	20	15.76	6.62	-1.35
16	2457455.5	14	15.55	6.53	+0.19
18	2457660.0	25	17.65	7.41	-1.30
19	2457690.0	7	17.24	7.24	-0.68
20	2457732.0	7	16.46	6.91	-0.79
21	2457764.5	4	15.92	6.68	-0.34
22	2457809.0	7	15.56	6.53	-0.08
23	2457865.0	7	15.89	6.67	+0.57
24	2457915.4	5	16.73	7.02	+0.56
Mars					
13	2457330.5	12	146.19	48.30	+7.75
14	2457354.5	8	175.88	58.14	+8.70
15	2457409.5	20	319.71	105.62	+27.68
16	2457455.5	14	666.46	218.49	+30.37
18	2457660.0	25	597.17	199.44	-21.61
19	2457690.0	7	439.23	146.24	-4.82
20	2457732.0	7	311.78	103.98	-4.89
21	2457764.5	4	239.37	79.54	-2.12
22	2457809.0	7	174.99	57.94	-4.94
23	2457865.0	7	123.61	40.61	-5.44
24	2457915.4	5	102.08	33.68	+0.59

Table 10: NIKA2 Planet fluxes. a: Nika Run, b: Julian Date when the model are computed, c: Run duration, d, e: total fluxes at 260 and 150 GHz, f: variation of the 150 GHz flux density over the duration of the run

	flux densities (Jy)			
	A1 & A3 260 GHz	A2 150 GHz	$\alpha^1$	Ref.
MWC349A	$2.06 \pm 0.04$	$1.48 \pm 0.02$	$+0.60 \pm 0.01$	PdB [11]
NGC7027	$3.46 \pm 0.11$	$4.26 \pm 0.24$	$-0.34 \pm 0.10$	Hoare et al 1992 [12]
CRL2688	$2.91 \pm 0.23$	$0.76 \pm 0.14$	$+2.44 \pm 0.18$	Dempsey et al 2013 [2]

<sup>1</sup> Spectral index is defined as  $S_\nu \propto \nu^\alpha$ .

Table 11: Reference flux densities of secondary calibrators at the NIKA2 reference frequencies 150 and 260 GHz. Uncertainties of flux densities extrapolated at 150 and 260 GHz include contribution of the uncertainty on  $\alpha$ .

MWC349A has been monitored with the Plateau de Bure interferometer and VLA, and shown to be stable in time and only slightly angularly resolved, making it a point source for the 30-metre telescope. The SED of MWC349A [11] is presented in Fig. 33. We have computed its flux densities at the NIKA2 reference frequencies 150 and 260 GHz with  $S_\nu = 1.16 \pm 0.01 \times (\nu / 100\text{GHz})^{0.60 \pm 0.01}$  provided by this monitoring [11].

The secondary calibrator CRL2688 is an Asymptotic Giant Branch star. Its radio continuum emission is mostly from circumstellar dust and is somewhat extended [3]. Its flux densities at  $850 \mu\text{m}$  and  $450 \mu\text{m}$  have been stable at the 5% level as monitored by SCUBA2 in 2011-2012 [2]. We have extrapolated their flux densities to 150 and 260 GHz with the power law  $S_\nu \propto \nu^\alpha$  and index  $\alpha = 2.44 \pm 0.18$  derived from their SCUBA2 measurements.

The secondary calibrator NGC7027 is a young, dusty, carbon rich Planetary Nebula with an ionized core. It is extended in the continuum and molecular lines (Bieging et al 1991), and is not a point source for the 30-metre telescope. Its most recent flux densities are reported at  $1100\mu\text{m}$  and  $2000\mu\text{m}$  by Hoare et al (1992). It has been reported to decrease by  $\sim 0.145$  percent/yr in the optically thin part of its spectrum above 6 GHz from VLA observations (Zijlstra, van Hoof & Perley 2008, and Hafez et al, 2008) that makes these flux densities uncertain by 3.6% currently. Its SED from cm wavelengths to optical is also presented in Hafez, Y.A. et al (2008). Its flux densities have been extrapolated to 150 and 260 GHz and the modelled decrease since 1992 included.

All these extrapolated flux densities are in Table 11.

### 7.3 Aperture photometry

Generally speaking, photometry is most advantageously done by PSF fitting when target is a point-source and the telescope PSF is well known. The 30-metre PSF with NIKA2 is not fully characterised yet and likely depend on elevation and atmospheric conditions. Hence, instead of PSF fitting, we have used aperture photometry to recover as much as possible of the calibrator flux spread over the main beam and side lobes of the telescope for our study of the stability of the calibration. For this study, observations were beammmaps and  $8' \times 5'$  otf's of the primary calibrators Uranus and Neptune and of the secondary calibrators MWC349A, NGC7027 and CRL2688. All are point-sources or quasi, except NGC7027 which is slightly extended.

We describe now how we have implemented aperture photometry.

All observations (beammmaps and  $8' \times 5'$  otf's) were first processed with the pipeline set

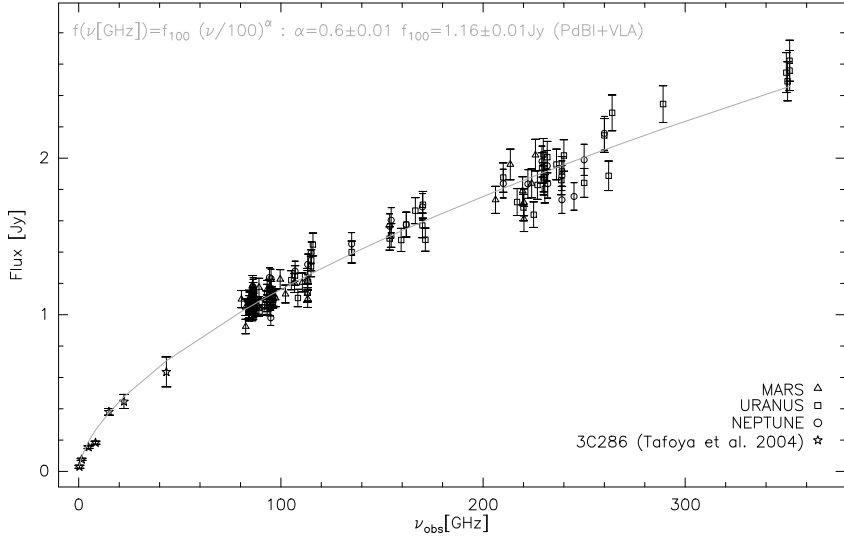


Figure 33: SED of MWC349A from its flux density monitoring at PdB and VLA [11]. Symbols are for primary calibrators used (Uranus, Neptune and Mars).

up with the parameters of Table 12 to produce the intensity map of each array. We stress that the gain-elevation curve of EMIR implemented in the pipeline was NOT turned on for this processing.

	run 9	run 10
kidpar	kidpar-best3files-FXDC0C1-GaussPhot	kidpar-n2r10-calib.fits
Decorrelation method	COMMON-MODE-ONE-BLOCK	COMMON-MODE-ONE-BLOCK
Opacity	l.o.s	l.o.s
Sky Projection	RADEC	RADEC
a priori mask	50''	100''
Iteration in mapping	None	None
Elevation gain curve	None	None

Table 12: Pipeline set-up for processing of the calibrators.

The total flux density of a source measured over an aperture is :

$$S_\nu = \sum_m \sum_n I_{m,n} (\text{Jy}/\text{beam}) \times \frac{dx^2}{\Omega_{\text{true}}} \quad (43)$$

$I_{m,n}$  is the brightness in Jy/beam measured in each pixel  $(m, n)$  of the NIKA2 map ;  $dx$  is the pixel size ;  $\Omega_{\text{true}}$  is the solid angle of the total beam named *true* by usage ; pixel indices  $m, n$  are such that  $dx \times \sqrt{(m - m_c)^2 + (n - n_c)^2} < 150''$  with  $m_c, n_c$  being the map center, i.e. radial distance is smaller than the aperture radius 150''.

In each pixel, brightness  $I_{m,n}$  is naturally expressed in unit of Jy/beam where *beam* stands for the total beam of the telescope. This is because the source power incident on the telescope is captured both through its main beam and side lobes, *i.e.* through its total beam. Hence, prior to

summing all pixels within the aperture, brightness  $I_{m,n}$  must be converted from natural unit Jy/beam to Jy/pixel. This conversion is done with the factor  $\frac{dx^2}{\Omega_{true}}$  which is, effectively, **the pixel area  $dx^2$  in unit of fractional beam<sup>2</sup>**. Practically,  $dx^2$  being set in arcsec<sup>2</sup> in the pipeline,  $\Omega_{true}$  must be measured in arcsec<sup>2</sup> also.

The computation of the solid angle of the total beam  $\Omega_{true}$  depends on the observation frequency  $\nu$  and on the radius  $r_{max}$  allowed by the map size. It can be measured as :

$$\Omega_{true}(\nu, r_{max}) = \int_0^{2\pi} \int_0^{r_{max}} B(\nu, r) 2\pi r dr \quad (44)$$

where  $B(\nu, r)$  is the radial profile of the source obtained in azimuthally averaging brightness over narrow annuli  $dr$  in width, and normalised so that  $B(0)=1$  (R. Adam's thesis (2016) or J.D. Kraus (1980)). (Equally valid is the direct summation of the pixels in each annuli scaled appropriately so that  $B(0)=1$ ). We have used  $r_{max} = 250''$  which is the maximum extent allowed by the size of the maps acquired during observations of runs 9 and 10. Power left beyond  $r_{max} = 250''$  at 260 GHz is between 34%, as estimated at 280 GHz, and 21% at 210 GHz in using parameters in Tables 1 and 4 of Kramer et al (2013) (amplitudes of the three error beams,  $\eta_{fss}$  and 1-Feff and see Carsten's email).

The excess of the total beam relative to the Gaussian beam is the ratio  $\Omega_{true}/2\pi(\sigma_{Gauss})^2$ , with  $\sigma_{Gauss}$  derived from the FWHM determined with the NIKA2 map for a point-like source.

#### 7.4 Determination of the solid angle of the total beam with Uranus and Neptune :

The solid angle  $\Omega_{true}$  of the total beam has been computed with eq. 44 as well as its excess relative to the Gaussian main beam for each observation of Uranus and Neptune in runs 9 and 10 under a broad range of atmospheric conditions ( $0.05 < \tau_{1mm} < 0.65$ ) and histograms of their values are shown in Fig. 34.

We have found that the solid angle of the total beam is slightly variable and its mean and rms are  $269 \pm 32$ ,  $462 \pm 30$ , and  $256 \pm 32$  arcsec<sup>2</sup> for arrays 1, 2, and 3, respectively. We note that  $\Omega_{true}$  is proportional to  $\nu^{-1}$  as expected. The excesses of the total beam relative to the Gaussian main beam (ratio of solid angles) have means and rms of  $1.89 \pm 0.16$ ,  $1.35 \pm 0.08$  and  $1.84 \pm 0.17$ , for arrays 1, 2 and 3, respectively. The beam efficiencies (ratio of powers between main beam and total beam) can be derived in inverting these ratios. These efficiencies are  $\sim 55\%$  at 1mm ( $(1/1.87) \times 100$ ) and  $\sim 70\%$  at 2mm ( $(1/1.35) \times 100$ ) over the extent  $r_{max} = 250''$  and are consistent with the direct determination reported in Table 7 in § 6.

**FM: it would help the reader to have all these values in a table ; JFL's reply at the moment : inconsistencies between numbers in Table 7 above required some discussion.**

We have searched for any systematics in  $\Omega_{true}$  with respect to elevation, opacity, and transmission ( $\exp(-\tau/\sin(elev))$ ) in Fig. 35. Over the limited range of elevations between 33° and 58°

---

<sup>2</sup>(-check this-) in the pipeline, aperture photometry assumes the solid angle of a fixed Gaussian beam, and so :

$$S_\nu = \sum_m \sum_n I_{m,n} (\text{Jy/beam}) \times \frac{dx^2}{2\pi\sigma_0^2}$$

where the conversion factor becomes  $\frac{dx^2}{2\pi\sigma_0^2}$ , with  $\sigma_0 = \text{FWHM0}/2\sqrt{2\ln 2}$  for the Gaussian FWHM0=12.5'' and 18.5'' at 1 and 2 mm, respectively. Note that  $\frac{\Omega_{true}}{2\pi\sigma_0^2}$  is  $\sim 1.5$  and  $\sim 1.2$  at 1 and 2 mm, respectively.

covered by these observations, there is no definitive correlation although a 15% increase of  $\Omega_{true}$  at small opacity ( $< 0.15$ ) and, consequently, at high transmission ( $> 0.8$ ), is hinted by inspection of the plots. This effect is not understood and under investigation.

## 7.5 Stability of calibration with the primary calibrators Uranus and Neptune

The primary calibrators Uranus and Neptune are the best sources to characterize the stability of the instrument because they are significantly stronger than the other calibrators. We have characterized the stability of NIKA2 in estimating the ratios between their measured and predicted flux densities. The measured flux densities are from aperture photometry of all 18 observations of Uranus and Neptune of runs 9 and 10. These observations are beammaps (20 min) and integrated sequences of 4 consecutive off scans ( $4 \times 4 \text{ min} = 16 \text{ min}$ ), providing comparable integration times and so similar statistical error for all observations. The aperture radius was as large  $150''$  to reach saturation level as illustrated in Fig. 36.

The stability of the calibration during these two runs is shown in Fig. 37 where all the flux density ratios of Uranus and Neptune are plotted sequentially. First, we have found that the resulting means  $\mu$  of these ratios are close to unity, 1.005, 1.007, 1.034, for array 1, 2, 3, respectively, indicating that the reference flux densities of the planets used to set the Jansky scale early in the data processing with the kidpar have been properly recovered. This absence of significant bias is a self-consistency test : input and output flux densities of planet are the same to better than 3.4 %. This indicates that calibration of the kidpar made in fitting a Gaussian with a reference FWHM0 of  $12.5''$  or  $18.5''$  to determine the response of each KID at 1 or 2mm is a good proxy for fitting the total beam. This was not obvious from the start since these reference FWHM0's were carried over from NIKA1. This should be subject to further investigations. Note that the resolution of the telescope set by the main beam is finer with FWHM's of  $\sim 11''$  and  $\sim 17.5''$  (see § 6.3). Second, we have found that the scatter (rms) around these mean ratios are indicative of a stability at the level of 4.5%, 5.0%, 6.6% for arrays 1, 2, 3, respectively. This stability is comparable to the level achieved by other modern instruments, e.g. SCUBA2 (Dempsey, 2013).

It is noticeable that this level of stability has been characterised in using two runs separated by two months and a warm up of the instrument in between. It is also noticeable that the atmospheric conditions change significantly ; it changed from fair weather during run 9 in february 2017 ( $0.05 < \tau_{1mm} < 0.35$ ) to mediocre weather during run 10 in April 2017 ( $0.3 < \tau_{1mm} < 0.65$ ). A detailed analysis shows that scatters around the mean ratios are about twice smaller in the first run (fair) than during the second run (mediocre) ; precisely, stabilities for the first run are 3.6%, 2.5% and 2.9% for arrays 1, 2, 3, respectively, and, correspondingly, are 5.3%, 6.7% and 8.6% for the second run. It is thought, at the moment, that limitations in stability must be caused by residual atmospheric fluctuations in the astronomical signal and small uncertainty in opacity corrections.

Also, we have plotted the flux density ratios versus elevation, opacity and attenuation in Fig. 38. No correlation is apparent. The possible correlation of  $\Omega_{true}$  with small opacity found in Fig. 34 is not seen in the flux densities. This is an indication that variability of  $\Omega_{true}$ , possibly caused by telescope surface deformations and atmospheric conditions, has been modelled properly and that the conversion factor  $dx^2/\Omega_{true}$  used for aperture photometry in eq. 43 has largely removed the effect in the measured flux densities. We stress again that no gain-elevation curve was applied in processing the data but that  $\Omega_{true}$  was determined for each observation.

In addition to the stability that we have just characterised, absolute calibration depends also on the accuracy of the Moreno's model used to predict the reference flux densities of Uranus and Neptune (see § 7.1.7). This is estimated to be 5% in the millimeter wavelength domain of the SED's of the planets. Hence, in combining quadratically all limitations, bias ( $\mu$ ), stability (rms) and Moreno's model accuracy, absolute flux density of NIKA2 is 11% in mediocre atmospheric condition and 7% in fair condition as characterized with Uranus and Neptune in runs 9 and 10. There is no significant difference between 1 and 2 mm. This is summarised in Table 13.

Weather	limitations			absolute
	$\mu$	rms	model	
fair ( $0.05 < \tau_{1mm} < 0.35$ )	3.4 %	3.6 %	5 %	7 %
mediocre ( $0.3 < \tau_{1mm} < 0.65$ )	3.4 %	8.6 %	5 %	10.5 %

Table 13: Accuracies of components and absolute calibration.

Correlations between flux density ratios of the three arrays are shown in Fig. 39, separately for runs 9 and 10. Highest correlations are found between arrays 1 and 3.

Finally, for the sake of completeness, we have redone the stability study in keeping separate all individual 4 minute long otf's. The resulting flux density ratios are shown in Fig. 40. Their means and rms are found to be totally consistent with our previous estimates.

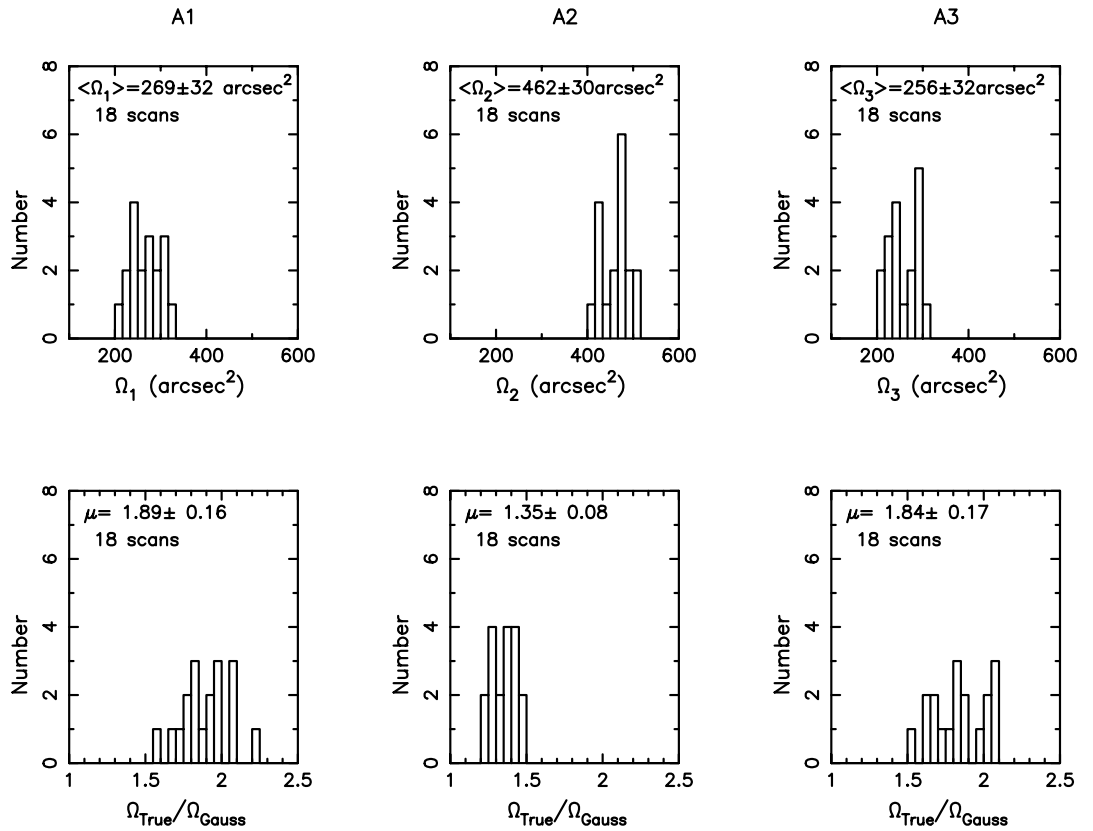


Figure 34: Top line : solid angles of the total beam ( $\Omega_{true}$ ) for arrays A1, A2, A3. Bottom line : excesses relative to the Gaussian main beam ( $\Omega_{true}/2\pi(\sigma_{Gauss})^2$ ) for the three arrays. All 18 observations of Uranus and Neptune a during runs 9 and 10 are shown ( $\sigma_{Gauss}$  is related to the FWHM actually measured for the Gaussian main beam for each observation, i.e. it is not related to the reference FWHM0 12.5'' and 18.5''). Mean and rms are provided for the three arrays.  
**FM:** the scale of the y axis should be much smaller ; **JFL :** will be done for final version of document

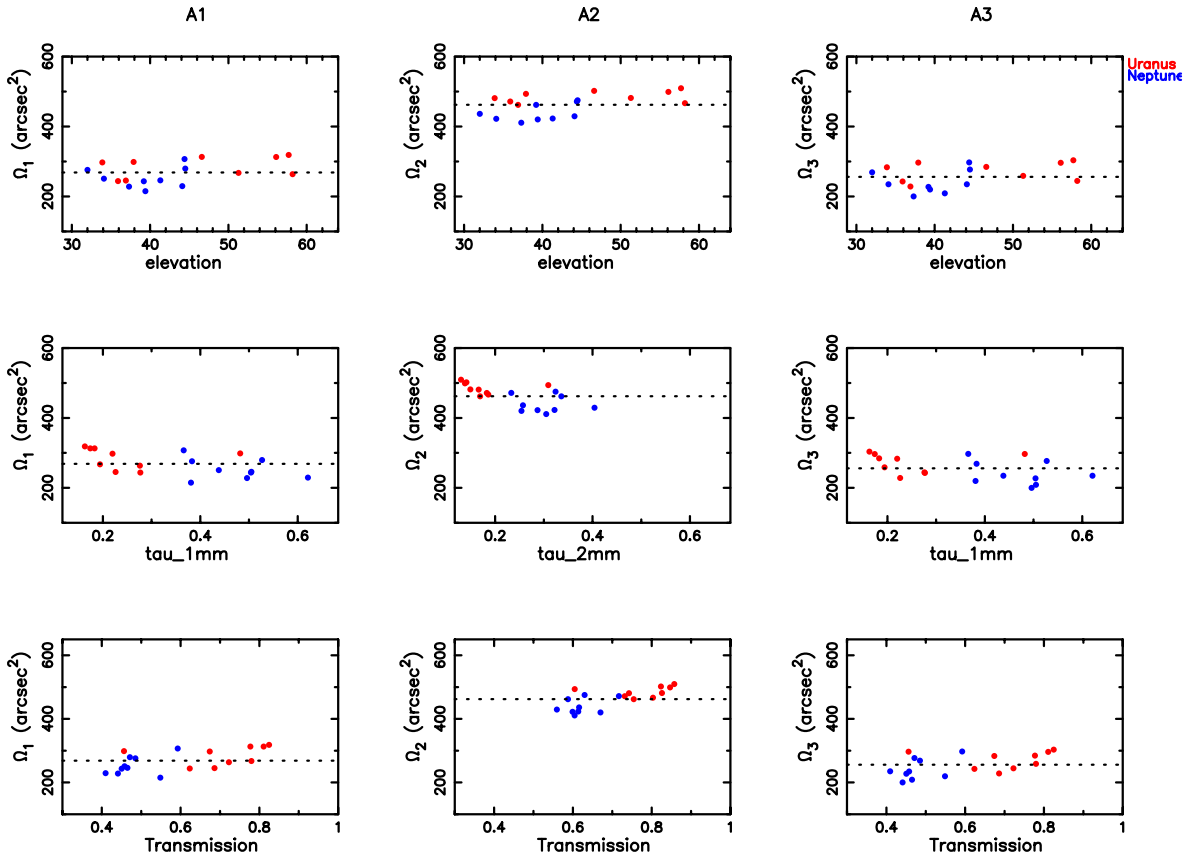


Figure 35: Search for systematics in the solid angle of the total beam  $\Omega_{true}$  with respect to elevation, opacity and transmission ( $\exp(-\tau/\sin(\text{elev}))$ ) of all 18 observations of Uranus and Neptune during runs 9 and 10. There is no definitive correlation although a 15% increase of  $\Omega_{true}$  at small opacity ( $< 0.15$ ), and consequently at high transmission ( $> 0.8$ ), is hinted by close inspection of these plots. **FM: the scale of the y axis should be much shorter ; JFL's reply : will be done for final version of document**

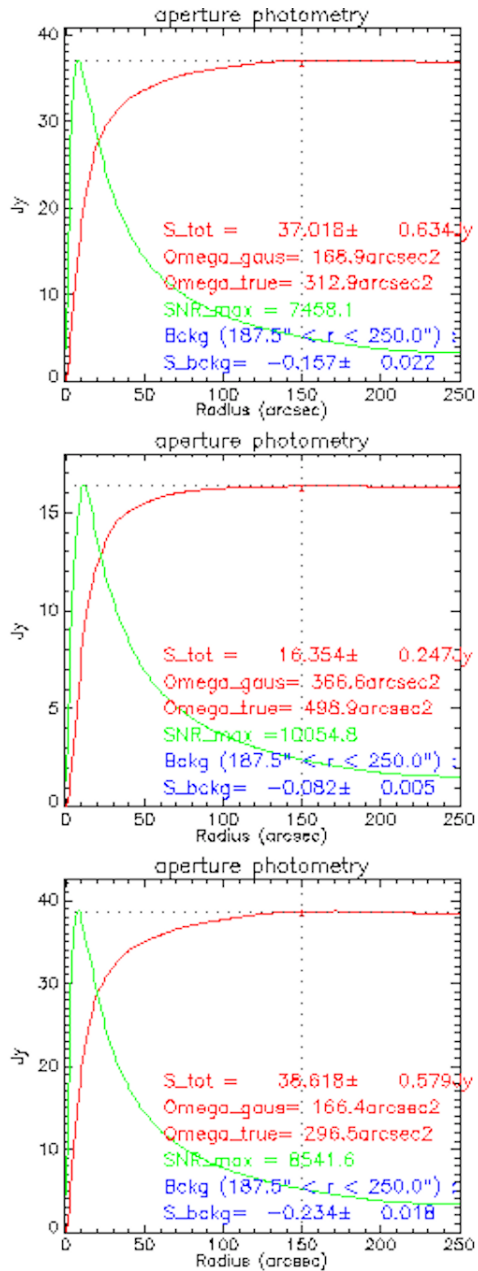


Figure 36: Aperture photometry of Uranus scan 20170227s308 on arrays 1, 2 and 3 from top to bottom. The photometric curve in red saturates at about the radial distance of 150''. (Green curve is the SNR in individual annulus ; it can be ignored for the purpose of this document)

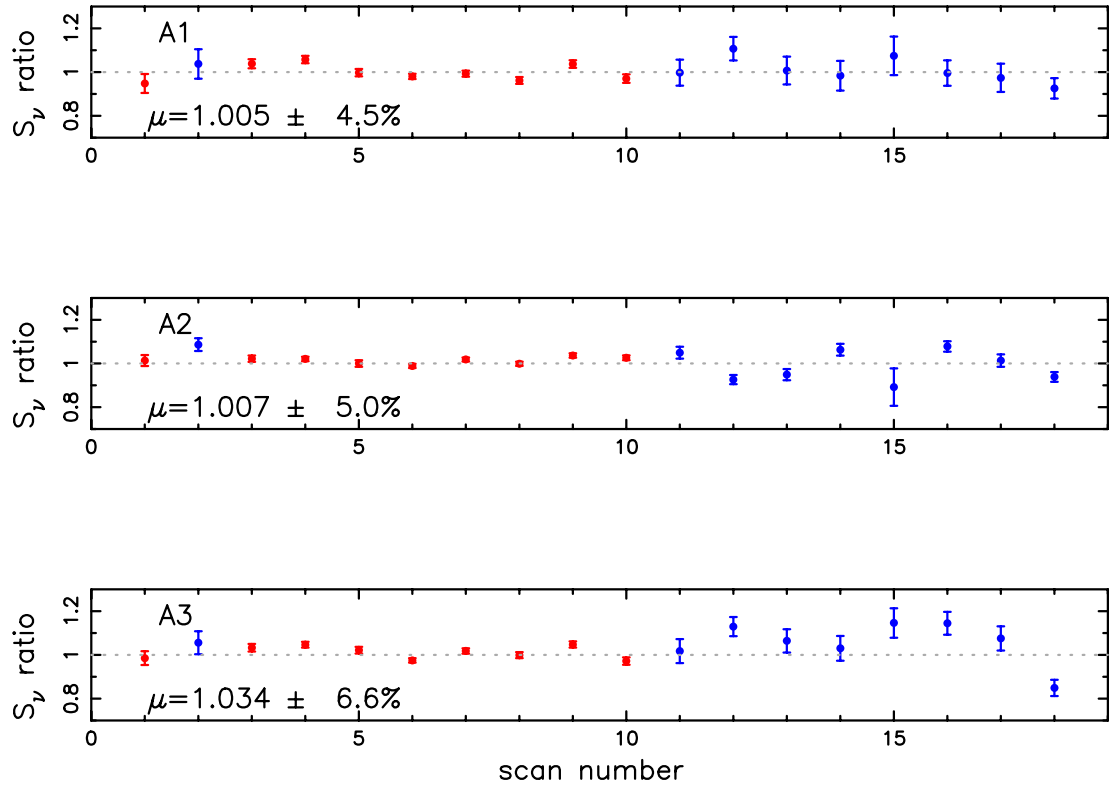


Figure 37: Stability of calibration with the primary calibrators Uranus (red) and Neptune (blue) shown in plotting ratios between their measured and reference flux densities during run 9 and 10. Mean ratio  $\mu$  and scatter in percent are provided for each array. Observation numbers are time ordered : 1 to 10 are during run 9 (23-28 february 2017) and 11 to 18 are during run 10 (19-25 april 2017). Neptune was hardly visible at the telescope during run 9, and Uranus was not visible during run 10. Observations are beammaps (22 min) and integrated sequence of 4 consecutive 4 minute long ofts (16 min) that are comparable in integration times.

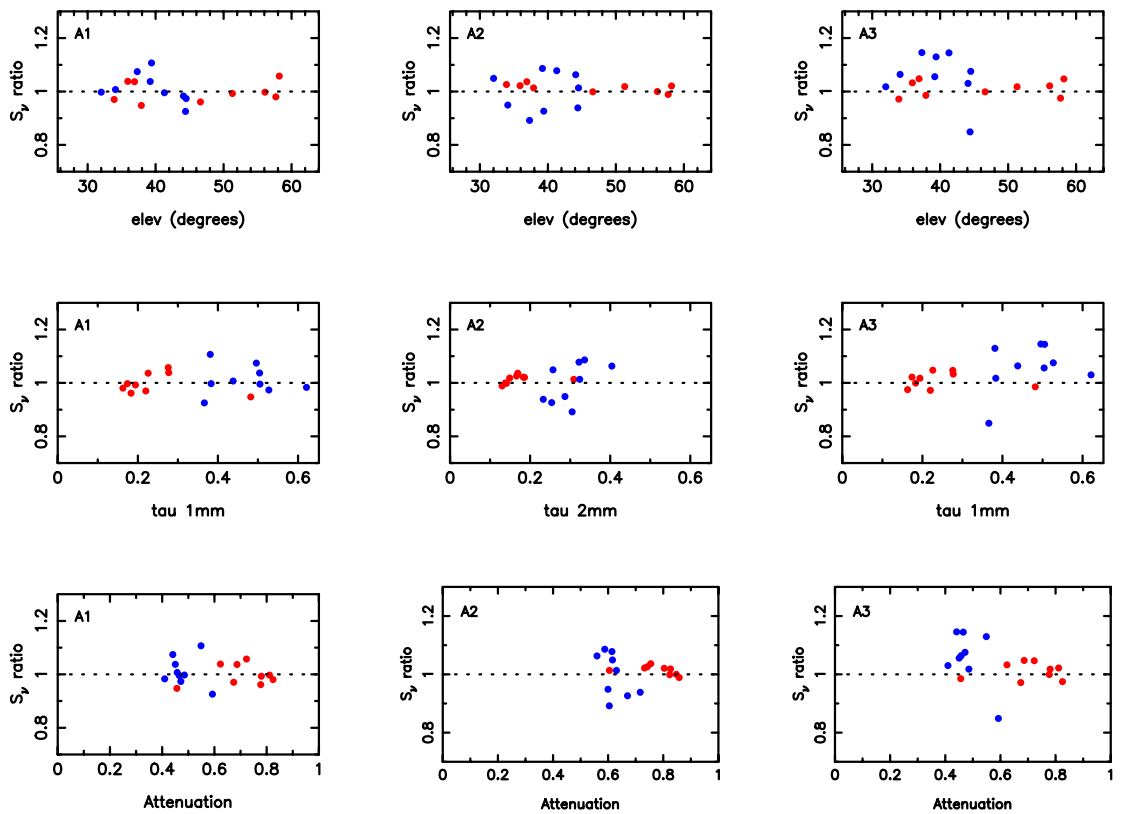


Figure 38: Flux density ratios versus elevation, opacity, and attenuation ( $\exp(-\tau / \sin(\text{elev}))$ ) for Uranus and Neptune. No correlation is apparent with attenuation. **FM: the scale of the y axis should be much shorter ; JFL's reply : will be done for final version of document**

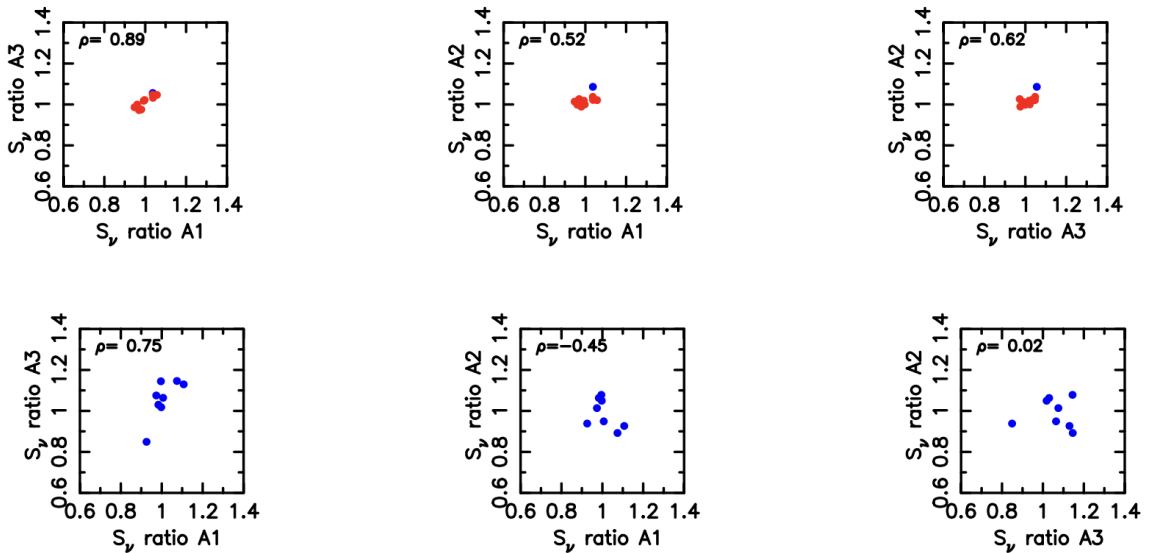


Figure 39: Correlation plots for the flux density ratios between the three arrays shown separately for run 9 in the first line (fair atmospheric condition), and for run 10 in second line (mediocre condition). Correlation coefficients  $\rho$  are given. **FM: the scale of the y and x axis should be much shorter ; JFL's : will be done for final version of document**

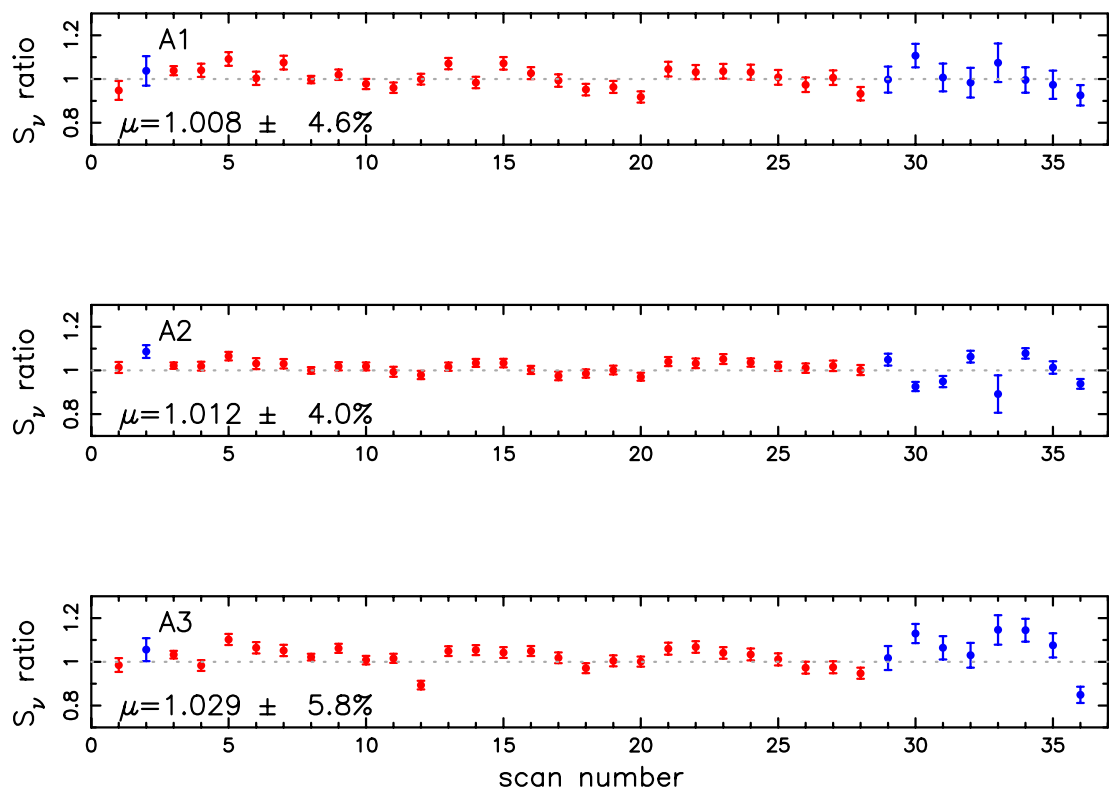


Figure 40: Stability of calibration with the primary calibrators Uranus (red) and Neptune (blue). In this plot, single 4 minute long otf's of Uranus acquired during run 9 are kept separate, while, in Fig.37 above, observations of 4 consecutive otf's were integrated together (16 min). Means and rms of flux density ratios are not significantly different though.

## 7.6 Calibration of the secondary calibrators MWC349A, NGC7027 and CRL2688

The sources MWC349A, NGC7027 and CRL2688 are standard secondary calibrators and were observed during runs N2R9 and N2R10. Their reference flux densities at the NIKA2 frequencies of 150 and 260 GHz are in Table 11 and were predicted from the literature for NGC7027 and CRL2688 (see § 7.2.3) and from the IRAM monitoring program at PdB for MWC349A [11]. Thirteen of the 84 observations (sequence of 4 consecutive 4 min long otf's) of these three secondary calibrators were discarded because aperture photometry failed.

As for the planets, the observations of these secondary calibrators were processed with the pipeline set up with the parameters of Table 12. In this scheme, the basic conversion from KID Hz shifts to Jy/beam is done through the kidpars, *kidpar-best3files-FXDC0C1-GaussPhot* for run 9 and *kidpar-n2r10-calib* for run 10, which were calibrated with Uranus and Neptune. Maps of the secondary calibrators were produced and their flux densities were measured with two methods : aperture photometry in Table 14, and the pipeline Gaussian fit in Table 15. For aperture photometry, the solid angle of the total beam  $\Omega_{true}$  was determined for each observation, while for the pipeline Gaussian photometry a fixed solid angle is assumed and based on the reference FWHM 12.5'' and 18.5''.<sup>3</sup> Color-corrections have been applied with indices  $\alpha = +0.6, -0.34$  and  $+2.44$  for MWC349A, NGC7027 and CRL2688, respectively, while Uranus and Neptune have  $\alpha = +1.6$ . These color corrections are smaller than 2.5% (see Table in § 7.1.7, CAUTION : this table is pending in HA section). Note that in Tables 14 and 15, for each calibrator, its flux density and uncertainty are the mean and standard deviation of all its observations with an array during a run. Note again that each observation is the integration of 4 consecutive otf scans (total 16 minutes).

			Flux densities (Jy)		
	run	#obs	A1 $S_{260\text{GHz}}$	A2 $S_{150\text{GHz}}$	A3 $S_{260\text{GHz}}$
MWC349A	9	10	$2.23 \pm 0.32 (+8.2\%)$	$1.49 \pm 0.11 (+0.6\%)$	$2.15 \pm 0.35 (+4.6\%)$
	"	14	$1.96 \pm 0.17 (-4.8\%)$	$1.48 \pm 0.08 (+0.2\%)$	$2.10 \pm 0.19 (+1.8\%)$
NGC7027	9	13	$3.22 \pm 0.39 (-6.9\%)$	$4.19 \pm 0.18 (-1.6\%)$	$3.05 \pm 0.54 (-11.9\%)$
	"	15	$3.01 \pm 0.36 (-13.0\%)$	$4.04 \pm 0.30 (-5.2\%)$	$3.31 \pm 0.19 (-4.2\%)$
CRL2688	9	11	$2.91 \pm 0.48 (-0.1\%)$	$0.59 \pm 0.05 (-22.9\%)$	$2.68 \pm 0.51 (-7.9\%)$
	"	8	$2.36 \pm 0.14 (-19.0\%)$	$0.52 \pm 0.04 (-32.1\%)$	$2.49 \pm 0.18 (-14.5\%)$

Table 14: Flux densities from **aperture photometry** and relative differences with respect to reference values.

**FM: i'm not sure that the relative differences with respect to reference values is an interesting parameters as in our case the bias, if any, is small than the error bars.**

**FM: I think it would help the reader to have the values of these tables on a figure (or 2) to judge by eye is there is an agreement. Moreover, the comparison requires to use a table**

<sup>3</sup>Although flux densities  $S_\nu$  were measured at the central frequencies of the arrays  $\nu_c$  (255, 152, 258 GHz) adopted initially for the kidpars of Table 12, they were changed afterward to the NIKA2 reference frequencies  $\nu_{ref}$  (150, 260GHz) in using the correction  $\Delta S_\nu = \alpha S_\nu (\nu_{ref} - \nu_c) / \nu_c$  with the spectral indices  $\alpha$  ( $S_\nu \propto \nu^\alpha$ ) of the calibrators in Table 11. These changes are less than 5%.

given 10 pages before. The assessment of the photometry is a key point that would deserve an illustration. (but keep the tables as well)

JFL reply to FM : OK, in a short while, I will make a plot to summarize the two tables and will remove % differences from Tables (but they are kept in in the meantime)

By inspection of Tables 14 and 15, we conclude that :

- measured flux densities are statistically consistent when results are compared between runs 9 and 10 despite very different weather conditions. Satisfactorily, this is an indication that the atmospheric signal is properly removed from the raw data by the pipeline.
- measured flux densities are biased at the 10% level when results are compared between the two methods (aperture photometry and pipeline Gaussian photometry) ; for each calibrator, it is 10% up for MWC349A and CRL2688 (point sources) while it is 10% down for NGC7027 (slightly extended) and it is similar for the three arrays. This bias between the two methods should be investigated further but it indicates already that the two methods are viable. We remind that the pipeline fits the source with a Gaussian with a reference FWHM empirically fixed to 12.5'' or 18.5'', *i.e.* larger than the main beam width in order to approximate the complexe profile of the beam.
- measured flux densities of MWC349A and NGC7027 are statistically consistent when compared to the reference flux densities of Table 11. This is not true for CRL2688 which is found to be 20% lower at 1mm and 30% lower at 2mm. This overestimation of the reference flux densities in Table 11 is likely due to the large lever arm in frequency when extrapolating from the SCUBA2 850  $\mu\text{m}$  (345 GHz) and 450  $\mu\text{m}$  (650 GHz) measurements to the NIKA2 frequencies 150 and 260 GHz, and because of the large uncertainty of the SCUBA2 450  $\mu\text{m}$  flux density. However, we note again that the NIKA2 flux densities of CRL2688 are statistically consistent between the two runs. Future measurements should be planned for confirmation of this stability before CRL2688 is considered a reliable calibrator.

Finally, we provide the ratios between measured and reference flux densities for MWC349 only because its reference flux densities are monitored at PdB by Iram at frequencies close to NIKA2 and so are the most reliable among the three secondary calibrators. Ratios are given for

			Flux densities (Jy)		
	run	#obs	A1 $S_{260\text{GHz}}$	A2 $S_{150\text{GHz}}$	A3 $S_{260\text{GHz}}$
MWC349	9	10	$1.98 \pm 0.16 (-4.1\%)$	$1.46 \pm 0.05 (-1.3\%)$	$2.02 \pm 0.17 (-2.0\%)$
	"	10	$1.71 \pm 0.16 (-16.8\%)$	$1.44 \pm 0.05 (-2.5\%)$	$1.84 \pm 0.20 (-10.7\%)$
NGC7027	9	13	$3.53 \pm 0.33 (+2.1\%)$	$4.28 \pm 0.18 (+0.4\%)$	$3.62 \pm 0.36 (+4.7\%)$
	"	10	$3.27 \pm 0.19 (-5.5\%)$	$4.28 \pm 0.14 (+0.6\%)$	$3.53 \pm 0.19 (+2.1\%)$
CRL2688	9	11	$2.53 \pm 0.23 (-17.0\%)$	$0.55 \pm 0.02 (-27.5\%)$	$2.49 \pm 0.24 (-14.2\%)$
	"	8	$2.22 \pm 0.12 (-23.6\%)$	$0.54 \pm 0.02 (-29.3\%)$	$2.32 \pm 0.13 (-20.4\%)$

Table 15: Flux densities from **pipeline** gaussian fit and relative differences with respect to reference values.

aperture photometry in Fig. 41, and given for the pipeline Gaussian photometry in Fig. 42. The mean ratio and rms are provided in the figures. At 1mm, rms are  $\sim 10\%$  on arrays A1 and A3 and are slightly better in using the pipeline Gaussian photometry than aperture photometry. However, for the pipeline Gaussian photometry, the mean ratios are systematically lower than unity by  $\sim 10\%$  at 1mm. This bias in using the pipeline Gaussian photometry is also found for the Uranus and Neptune data of runs 9 and 10 but at a level of 5% at both bands. It is likely that an adjustment of the reference FWHMs for the pipeline Gaussian fit (currently 12.5'' and 18.5'') could remove this bias.

## 7.7 Tentative gain-elevation curve

We have searched for any elevation dependence of the solid angle of the total beam  $\Omega_{true}$  of Uranus and Neptune and found none for the elevation range of their observations between 30° and 65°. We have also studied such a dependence for the observations of the three secondary calibrators which span a larger range between elevations 23° and 74°. The most conclusive study is for NGC7027, the brightest secondary calibrator, in Figure 43. Its pipeline Gaussian photometry exhibits some degree of curvature centered around elevation 45° and in a similar way for the three arrays. While the pipeline Gaussian photometry assumes a fixed solid angle for the total beam based on the reference FWHM's 12.5'' and 18.5'', the solid angle as determined with the data themselves in using eq. 44 exhibits instead a similar curvature centered on elevation 45°. This needs confirmation with further observations over the largest elevation range possible at the telescope and on the strongest source available. Note finally, that the flux density of NGC7027 determined with aperture photometry does not exhibit any curvature, as expected, since the conversion factor  $\frac{dx^2}{\Omega_{true}}$  in eq 43 models the effect. We stress again that the EMIR gain curved was not turned on to process the data.

## 7.8 Calibration stability across the run

## 7.9 Flat fielding: calibration stability across the FOV

The dispersion of the detector responsivity across the field of view has been characterized by estimating flat fields using the nominally focused *beammap* scans described in Sect. 4. We have considered different kinds of flat field:

- Main beam flat field: the flat field for the main beam, which is the far field of the telescope estimated for the sources, is determined using the relative calibration factors obtained for the calibration in  $FWHM_0$  beam discussed in Sect. 7.1.7. These are defined as

$$G_k = \frac{S_{th}(\nu_0) e^{-\tau/\sin(\delta)}}{A_k}, \quad (45)$$

where  $S_{th}(\nu_0)$  is the expected flux of the source integrated in the NIKA2 bandpasses and derived at the reference frequency  $\nu_0$ ,  $\tau/\sin(\delta)$  is the line-of-sight opacity measured using the *skydip* method described in Sect. 3 and  $A_k$  is the amplitude of a Gaussian of fixed FWHM fitted from the detector  $k$  map (as  $A_c$  in Eq. ??).

- Forward beam flat field: the flat field for forward beam, which is the near field of the telescope determined for the sky noise, is estimated using the correlation factor of each detector to a median common mode estimated off-source.

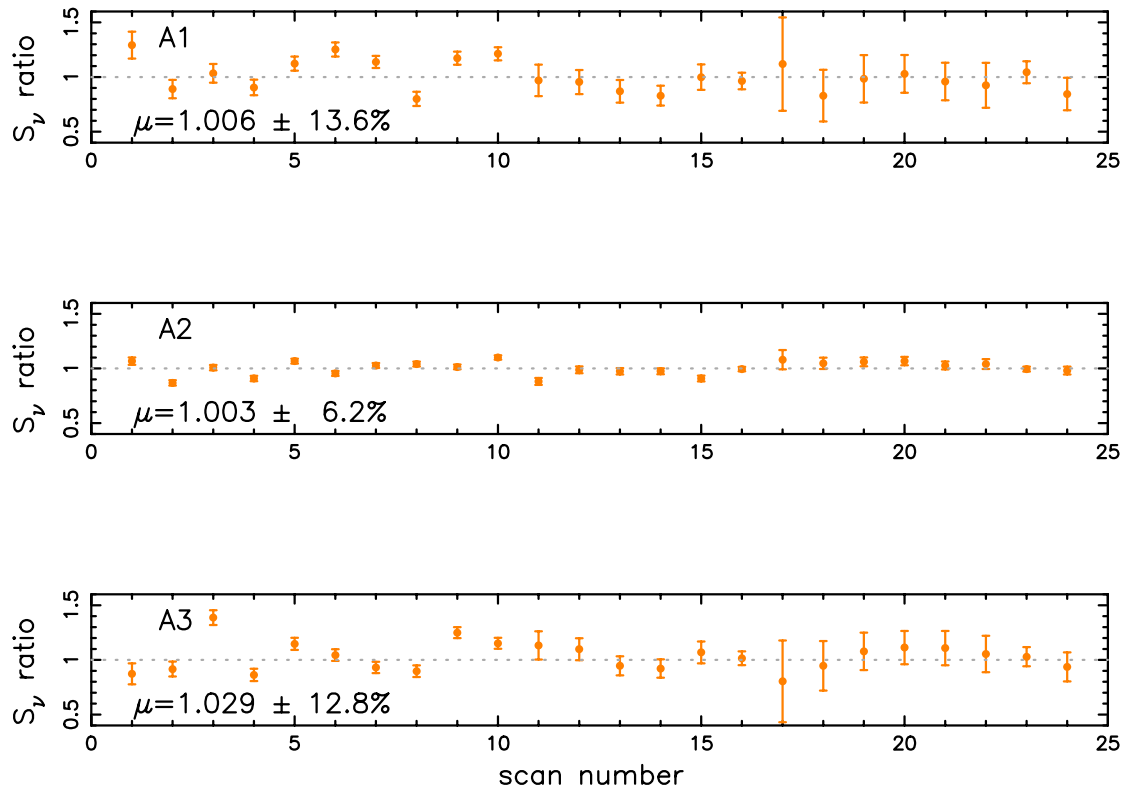


Figure 41: Ratios between measured and reference flux densities of the secondary calibrator MWC349A during runs 9 and 10. **The flux density is measured with aperture photometry.** Note that mean ratios on the three arrays are close to unity as expected for proper calibration. Scan numbers are time ordered (index 1 to 11 : run 9 (fair weather) and index 12 to 24 : run 10 (mediocre weather)). Each observation is a sequence of 4 consecutive 4 minute long offs (total integration is 16 minutes).

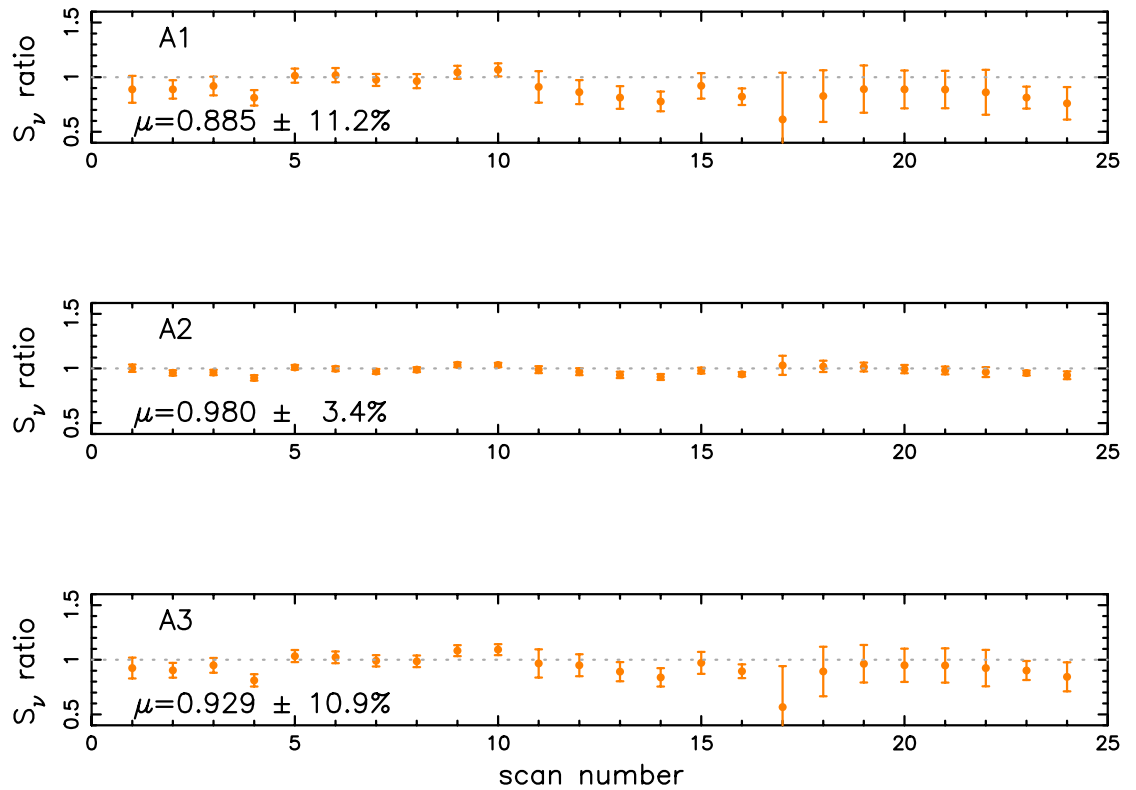


Figure 42: Ratios between measured and reference flux densities of the secondary calibrator MWC349A during runs 9 and 10. **The flux density is measured with the Pipeline Gaussian photometry.** Note that mean ratios on A1 and A3 are  $\sim 10\%$  lower than unity, unsatisfactorily. Scan numbers are time ordered (index 1 to 11 : run 9 (fair weather), and index 12 to 24 : run 10 (mediocre weather)). Each observation is a sequence of 4 consecutive 4 minute long offs (total integration is 16 minutes).

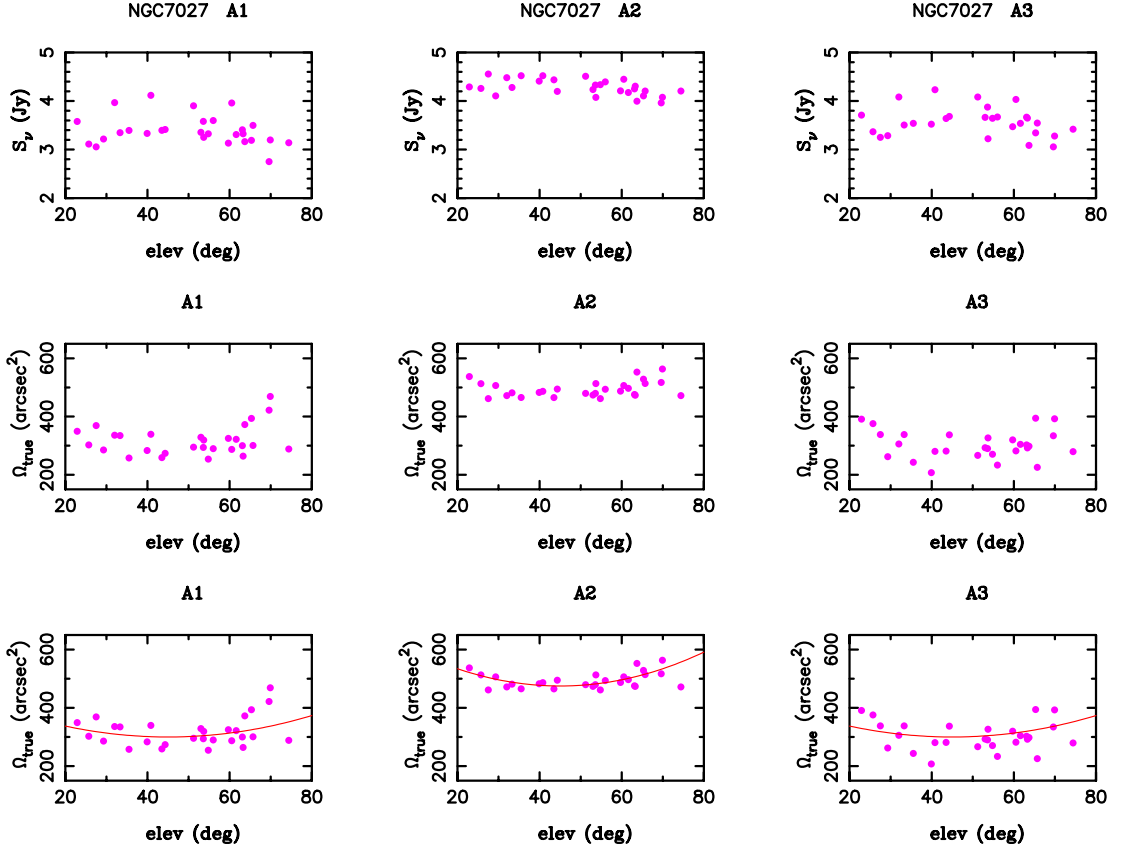


Figure 43: **Top line :** Flux densities of the secondary calibrator NGC720 **measured with the pipeline Gaussian photometry** with a fixed solid angle for the total beam of the telescope. The flux densities are given for the three arrays during runs 9 and 10 and exhibit some degree of curvature over the elevation range of the observations. **Second and third lines :** The solid angle of the total beam determined with the observations of NGC7027 themselves.  $\Omega_{\text{true}}$  is shown twice ; as unmarked plots on the second line and with a “fit by eye” centered on elevation  $45^\circ$  on the third line. Were this tentative gain-elevation curve applied, it would flatten the flux density above. Scan numbers are time ordered (index 1 to 13 : run 9 (fair weather), and index 14 to 28 : run 10 (mediocre weather)). Each observation is a sequence of 4 consecutive 4 minute long ofts (total integration is 16 minutes).

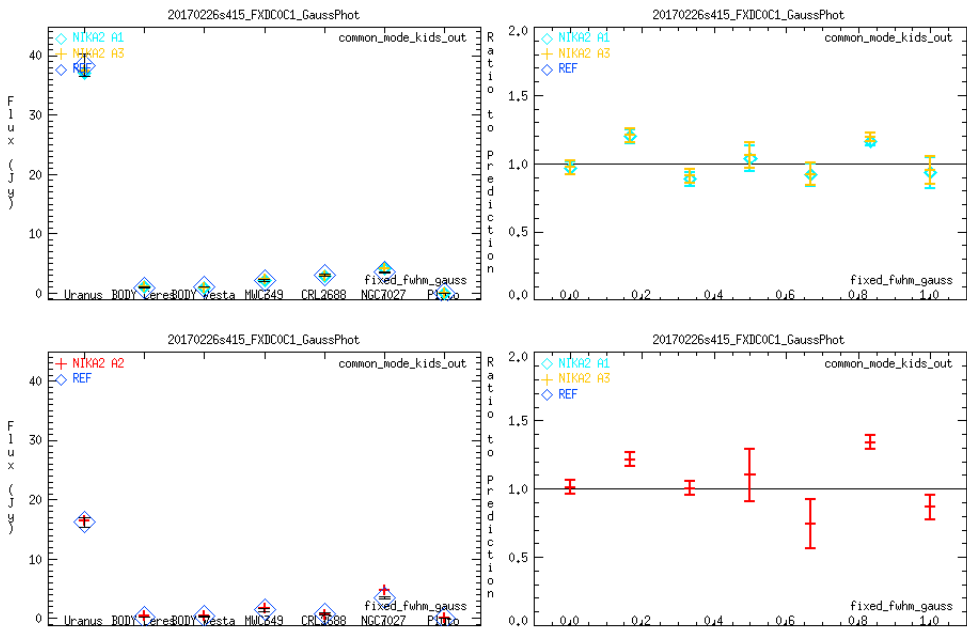


Figure 44: Decorrelation mask: 100 or 60 arcsec, KID cross-calib with fixed fwhm (12.5 and 18.5), then absolute photometry with the same fixed fwhm. Note: NGC7027 not point like and not corrected for here. Error bars from NIKA2 measurements and abs. cal. uncertainties by JFL.

Figures 49 and 50 show the average main beam and forward beam flat fields for the three arrays. These have been constructed by combining the normalised flat fields of five *beammap* scans, which were selected by thresholding the line-of-sight opacity measured in the 1-mm band, such as  $\tau / \sin(\delta) \leq 0.85$ . The distribution for the average flat fields are shown in the bottom panel of Fig. 49 & 50.

We observe a sizable variation of the flat fields for Array 1 from the left-most side to the right-most side of the FOV: this reveals a significant change of Array 1 detector responsivities depending on their position in the FOV. Namely, this effect, the origin of which is under investigation, mainly impacts the left-most third of the array, which is referred to as the "shadow-zone". This variation of the flat field translates into a broadening of the distribution. However, we verified that A1 flat field dispersions are in line with the ones of Array 3 after the detectors within the shadow-zone were flagged out using a crescent-shaped mask. The masked flat field distributions are shown in green in Fig. 49 & 50, whereas shadow-zone distributions are in red. In addition to the average flat fields, we further characterize the flat fields for individual *beammap* scans. Fig. 51 shows the dispersion of the flat fields for nine *beammap* scans using either the whole FOV or masking the shadow-zone. The dispersion estimates for this two cases are gathered in Table 7.9.

Dispersion (%)	KID selection	A1	A3	A2
Main beam flat field	all the FOV	$34.4 \pm 3.4$	$15.5 \pm 1.4$	$13.2 \pm 1.7$
	shadow-zone excluded	$17.0 \pm 1.1$	$14.2 \pm 1.2$	$12.8 \pm 1.3$
Forward beam flat field	all the FOV	$21.6 \pm 1.4$	$10.1 \pm 1.7$	$5.2 \pm 0.9$
	shadow zone excluded	$12.2 \pm 1.6$	$10.1 \pm 2.1$	$4.9 \pm 1.2$

Table 16: Average flat field dispersions in percent for nine *beammap* scans over all the FOV and after masking out the shadow-zone

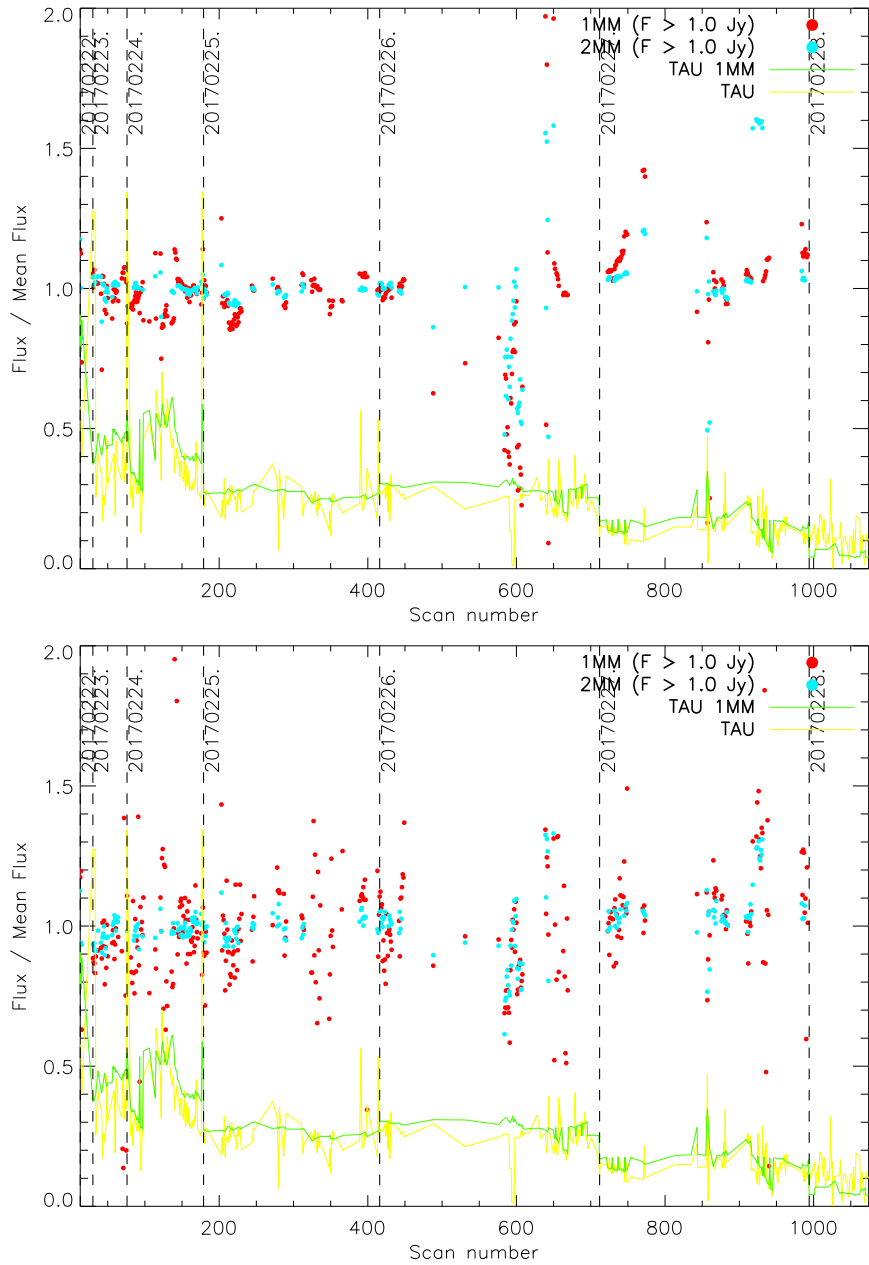


Figure 45: Ratio between the measured flux per scan and the averaged flux for all sources observed in N2R9. We considered both fixed FWHM (top) and aperture photometry fluxes for the 1 (red) and 2 (cyan) mm channels.

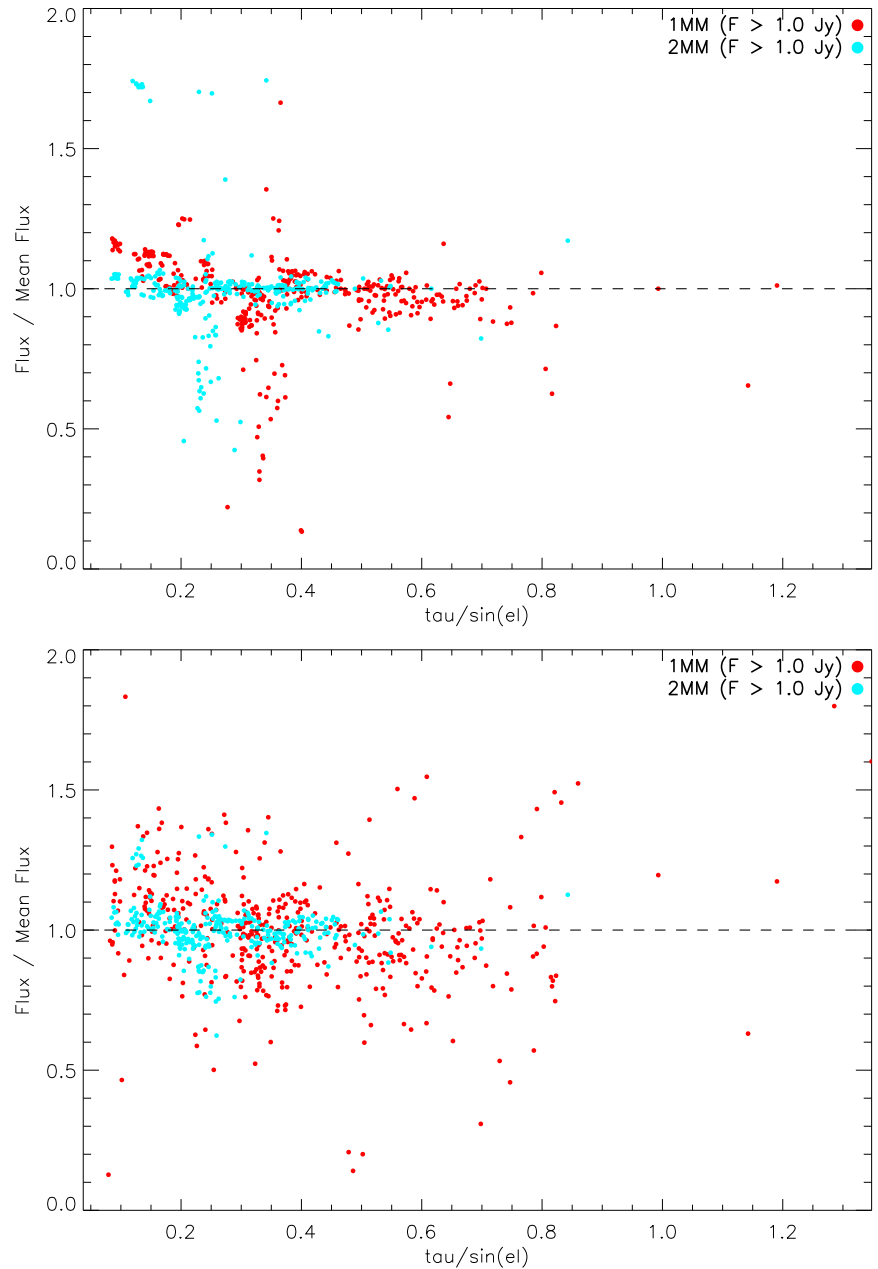


Figure 46: Ratio between the measured flux per scan and the averaged flux as a function atmospheric background for all sources observed in N2R9. We considered both fixed FWHM (top) and aperture photometry fluxes for the 1 (red) and 2 (cyan) mm channels.

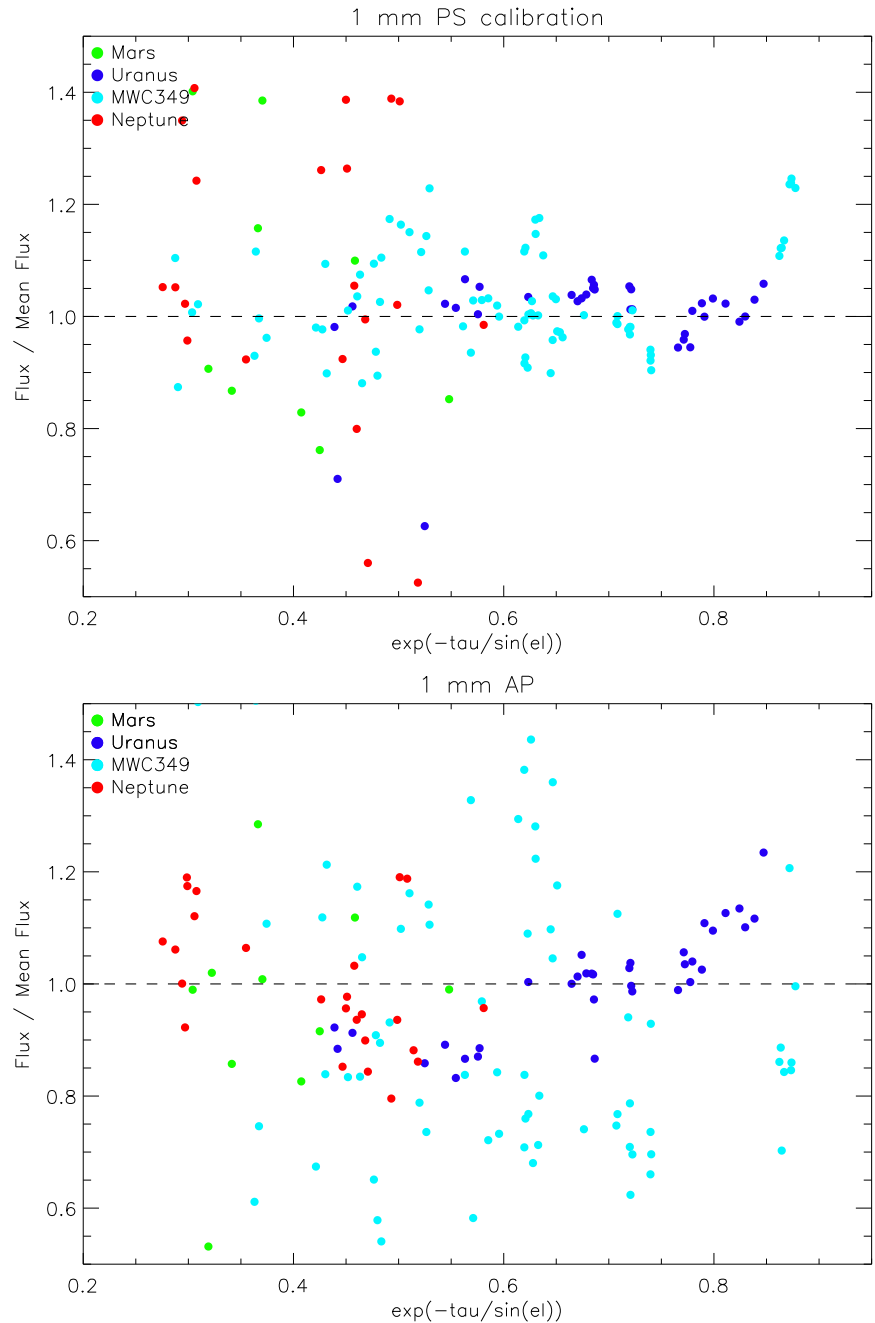


Figure 47: Ratio between the measured flux per scan and the averaged flux for all sources observed in N2R9 and N2R10. We considered both fixed FWHM (top) and aperture photometry fluxes for the 1 mm channel

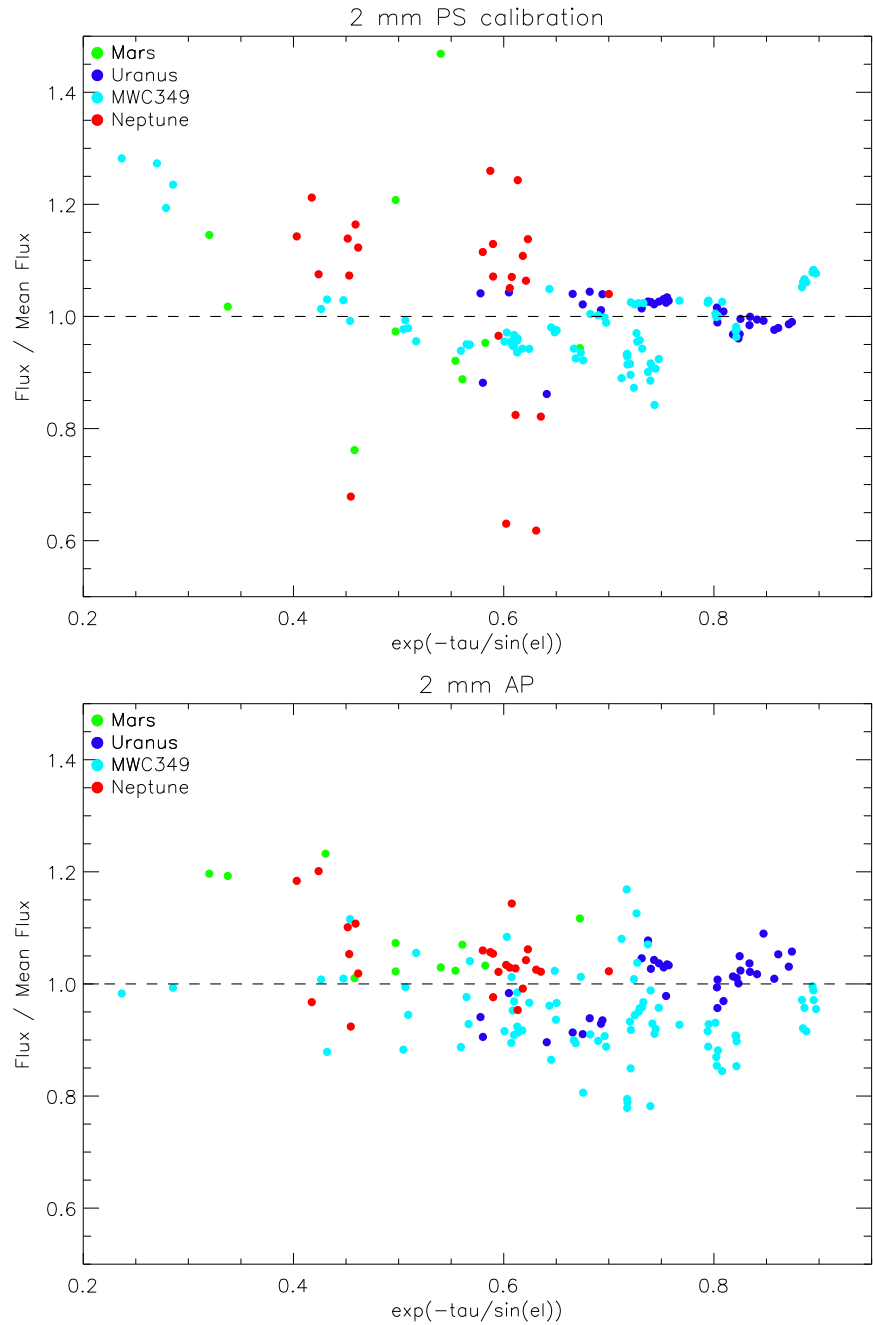


Figure 48: Ratio between the measured flux per scan and the averaged flux for all sources observed in N2R9 and N2R10. We considered both fixed FWHM (top) and aperture photometry fluxes for the 2 mm channel

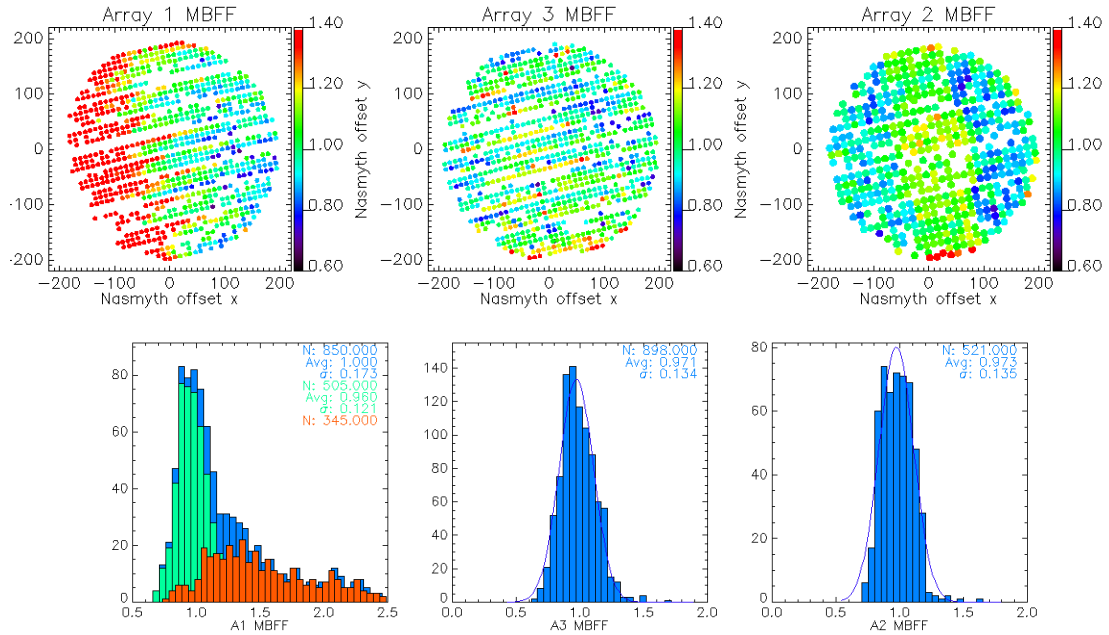


Figure 49: Average main beam flat field for array 1, 3 and 2

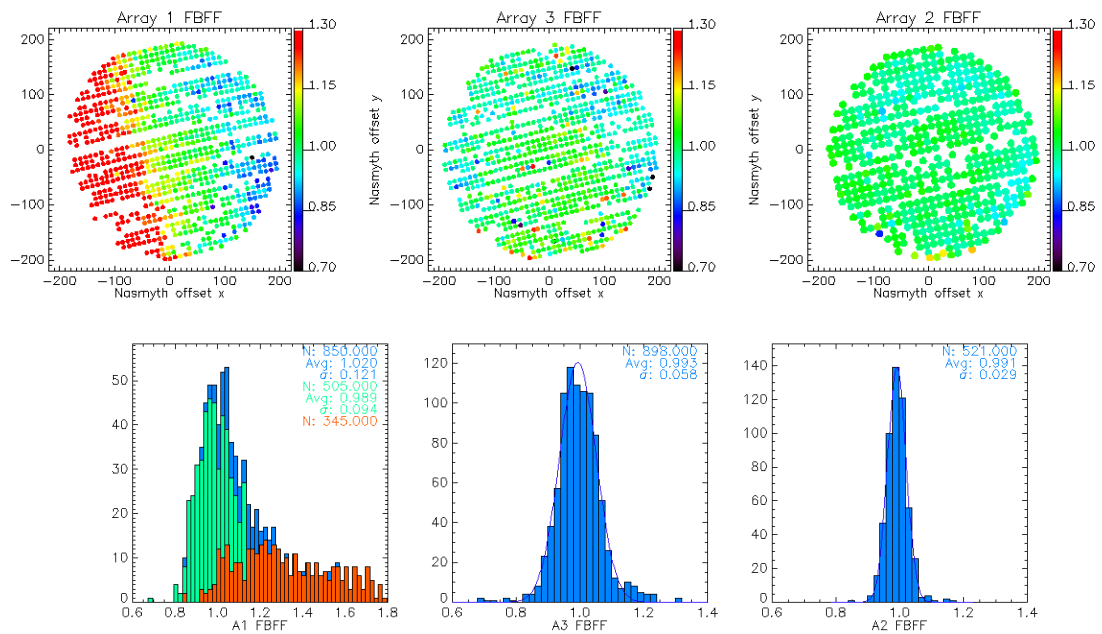


Figure 50: Average forward efficiency flat field for array 1, 3 and 2

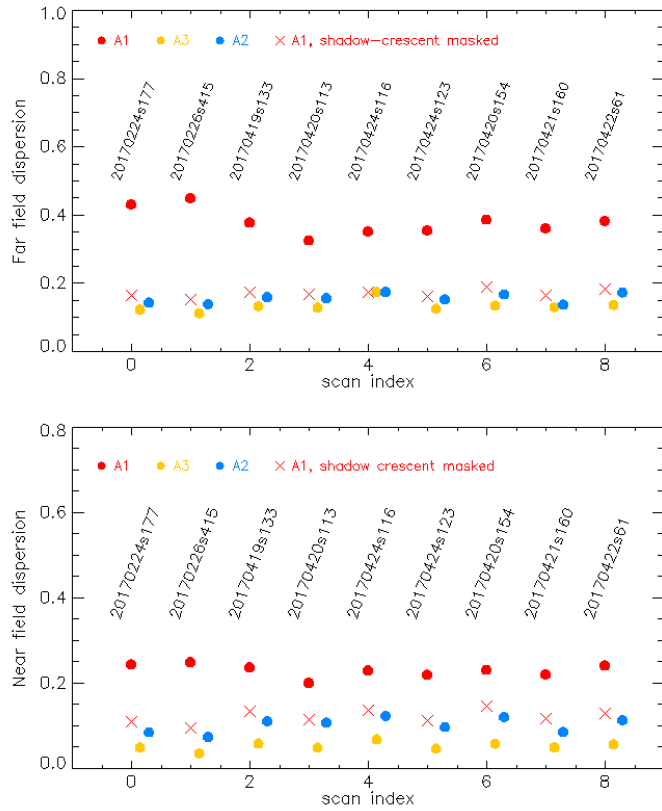


Figure 51: Dispersion of the flat field for nine *beammap* scans. The RMS dispersion of the main beam flat field (upper panel) and forward beam flat field (lower panel) are shown using all valid KIDs of Array 1 (red circles), Array 3 (orange circles) and Array 2 (blue circles), and using the KIDs located outside the Array 1 "shadow area", which was discarded using a left crescent-shaped mask (red crosses).

## **8 Noise description: TOI and maps**

### **8.1 Dark detectors at 1 mm**

## 8.2 Dark tests

# 9 Detector-Detector correlation matrix

For this work we have used several decorrelation methods trying to identify possible multiple components in the noise. Notice that in the following the atmospheric signal will be considered simply as correlated sky noise. The main decorrelation methods used are:

- CM **Common mode decorrelation.** We search for a common mode template using all detectors of the same array. To avoid bias from bad detectors we consider the median common mode.
- PCA **Principal Component Analysis.** For each NIKA2 array independently we decompose the covariance matrix in principal components. From those we derive up to 10 independent templates corresponding to the largest eigenvalue values.
- BC **Best correlated pixels.** For each detector in a given array we identify those detectors which are more correlated to it (a minimum of 14). Using those detectors we compute a common mode as in method CM.
- ALL **All detectors.** For each detector of a given array we use all other detectors of the same array as templates and perform a linear fit.

We present in Figure 52 the detector noise correlation matrices computed for the N2R7 dark scan 20161211s299 for the three arrays (A1, A2, and A3 from left to right). From top to bottom we present the correlation matrices for the raw data (no decorrelation), and for the CM, PCA, and BC decorrelated data. For each array the extent and name (from letter A to T) of the electronic boxes is indicated on the left of the figure. Notice that each electronic box consists of 5 subbands.

In the case of the raw data we observe very different structures for the three arrays. In arrays A1 and A2, we observe significant structure going from very correlated detectors to fully uncorrelated ones. This is observed even within a given electronic box or even between detectors from the same electronic subband. By contrast in A3 the detectors seems to be fully correlated. After CM decorrelation we observe that there is still significant correlation and anti-correlation for some detectors. In particular we observe a very clear pattern in A2 for electronic box A. In the case of the PCA decorrelated data the correlation matrix becomes much more diagonal although still shows significant level correlation within electronic subbands. We also notice that using the BC decorrelation improves with respect to the CM decorrelation but it is worse than the PCA case. These results tends indicate various electronic or detector related noise components.

In Figure 53 we show the noise correlation matrices for the N2R7 faint source scan 20161213s72. As expected the raw data noise correlation is dominated by atmospheric noise and we observe full correlation between detectors. After decorrelation the results are very similar to those found for N2R7 dark scan 20161211s299. There is residual significant correlation and anti-correlation after CM decorrelation. PCA decorrelation leads to a more diagonal correlation matrices. For the BC decorrelation the results are worse (more residual correlation and anti-correlation) and close to those of the CM decorrelation. As before there are good indications of multiple electronic-

detector noise components. It is interesting to note that the detector-electronic noise correlation patterns seems to be the same for dark tests and for sky data.

We have repeated the same analysis on scans of the N2R4 both for dark tests, scan 20160504s97, and faint sources, scan 20160313s87. We find few significant differences with respect to previous results. In the case of the dark test and for the raw data, the A1 and A2 detectors seems to be more correlated. Furthermore A2 show more significant correlation after CM decorrelation for electronic boxes B and D. Array A1 show also significant residual correlation and anti-correlation after CM et BC decorrelations. For the faint source N2R4 scan 20160313s87 we observe similar behavior but the pattern of the correlation matrices are not the same that for the dark test scan.

## 9.1 RMS of the noise

We present in Figure 56 the rms, in Hz, of the raw (dark blue) and decorrelated (CM, blue; PCA, red; and BC, cyan), data for the N2R7 dark test scan 21612101s299. We also show for comparison the rms of the data by extrapolating the median high frequency noise (PS, violet). For the three arrays we observe that decorrelation reduces significantly the rms noise. The most efficient method is PCA as one would expect from previous results in the noise correlation matrix.

For each array the detectors are ordered by electronic box (separated by vertical black lines in the figure) and within each electronic box by increasing resonant frequency. We observe that median high frequency noise increases with increasing resonant frequency. A similar effect is observed for the PCA and BC rms noise but for some pathological detectors or electronic boxes. While in A2 the rms noise increases monotonously with resonant frequency in arrays A1 and A3 we observe also observe fine structure within each electronic box. For array A2, electronic box A, shows significantly larger raw rms. For array A1 box K seems to have a larger number of anomalous detectors than the other boxes. In array A3 all boxes seem to be equivalent to first order. Both in A1 and A3 we find complex structure within each box, which are not present in A2.

Similar results are found for scan 20161213s72 as shown in Figure 57. However, we stress that the atmospheric emission shows significant contribution at high frequency (see PS) that is significantly reduced after decorrelation.

We have also computed the noise rms for the scans of N2R4 20160504s97 and 20160313s87. For arrays A1 and A3 the results are very similar to those for the N2R7 scans. However, we clearly observe that A2 is significantly worse in terms of misbehaving pixels.

## 9.2 Discussion

Using dark test measurements we have identified several noise components that require using complex decorrelation methods. Event in the case of multiple template decorrelation we find residual correlation between detectors that seems to be related to electronic subbands. Similar results are found when analyzing faint source scans. We find significant differences between N2R4 and N2R7 scans.

After decorralation using multiple template procedures we reduce significantly the rms of the noise. In the case of dark test it becomes of the level of the high frequency noise. For

faint source scans we also diminish the high frequency noise, which is probably dominated by atmospheric emission. We find significant differences between the noise levels in A1 and A3, which might be explained by gain differences (to be verified). For some electronic boxes in A2 the rms noise is significantly larger than for the others. For the three arrays we find increasing noise with increasing resonant frequency withing each electronic box. This is probably related to the difference of gains between subbands in the electronics. Furthermore, we find in A1 and A3 extra low frequency structures in the rms which are not identified yet.

## 10 Sensitivities

HLS J0918+5142 is moderately faint source, expected to be below 100 mJy at 1mm and XX mJy at 2mm **check values in NIKA1 paper + use SED for predictions in NIKA2's bands**. This source was chosen for its flux and its availability during Run9 for long integration. It has been observed for XX hours in total over three nights.

### 10.1 Observations

As part of the NIKA2 Science Verification that took place in February 2017, we observed an area of 185 arcmin<sup>2</sup>, centered on HLS J0918+5142, (a lensed dusty galaxy at z=5.24 [21]) during about 9 hours. The scans were 8x5 arcmin<sup>2</sup>, alternatively oriented in (ra,dec), (dec,ra), (az,el), (el,az).

The MoU defines the NEFD: *The Noise Equivalent Flux Density (NEFD) is the 1 $\sigma$  sensitivity in one second of effective on-source telescope integration time after the absolute calibration has been performed (i.e. after beam efficiency and opacity corrections). It is appropriate for 2 mm of precipitable water vapor (pwv) content in the atmosphere and 60 degrees elevation source. It refers to the inverse variance of the noise on the flux measurement of a point-source, averaged over the valid receiver pixels.*

IRAM has its own time estimator that will compute the “effective NEFD”, provided we give the “detector NEFD” and a fraction of valid KIDs. We must be careful not to mix both, which has been the case in several ways. We must not mix the intuitive definition of the NEFD and that of the mapping speed as well : in short, NIKA2’s NEFD must be the same as NIKA’s NEFD, but NIKA2’s larger FOV improves the mapping speed. All this was hidden in the definition of  $\eta$  in the previous version of this doc that I hope to clarify here.

To compute the instrumental NEFD (hereafter NEFD), we must compute the integration time on the source. This time is the total time spent by detectors measuring the source, *not* by the matrix footprint. Let’s be more specific: if the source is in the focal plane, but on a place where no KID is valid, the integration time is zero. There are 3 ways to estimate the time of integration. We introduce them in the following 3 subsections and compare them on Fig. 60.

#### 10.1.1 Time of integration from the density of samples

Let’s take a map of resolution  $r$ . The number of hits in the central pixel on the source  $N_h(r)$  leads to:

$$t_{int} = \frac{N_h(r)}{\nu} \frac{1}{N_{kids\ per\ pixel}} \quad (46)$$

Suppose we stay fixed on the source (no movement at all) during a time  $t_{obs}$ , and  $r$  is such that there is only one KID staring at the source, then

$$t_{int} = \frac{1}{\nu} t_{obs} \times \nu = t_{obs} \quad (47)$$

Suppose there are two kids per pixels, then the number of hits is twice as large while  $t_{obs}$  remains the same. In practice, this factor  $N_{kids \text{ per pixel}}$  is difficult to estimate exactly because it depends on the scanning strategy and the repartition of KIDs accross the FOV. In practice, we are bound to compute averages and thus to estimate the average number of KIDs per map pixel which is

$$N_{kids \text{ per pixel}}^{avg} = r^2 / g^2 \quad (48)$$

where  $g$  is the grid step of a matrix. Indeed, the total surface covered by  $N_{kids}$  detectors is  $S = N_{kids}g^2$  and there are  $S/r^2$  map pixels in this surface. So, the integration time on the source is finally

$$t_{int} = \frac{N_h(r)}{\nu} \frac{g^2}{r^2}. \quad (49)$$

Another justification of this formula is that  $N_h(r)/r^2$  is the density of samples in hits/arcsec<sup>2</sup> and  $g^2$  is the inverse of the number of KIDs per arcsec<sup>2</sup>. For the combined 1mm, we must divide by 2 because both matrices observe the same area at the same time:

$$t_{int}^{1mm} = \frac{1}{2} \frac{N_h(r)}{\nu} \frac{g^2}{r^2}. \quad (50)$$

So finally:

$$NEFD = \sigma \sqrt{t_{int}} \quad (51)$$

With this definition in hand, assuming we have only  $N_{valid}$  kids in a focal plane of  $N_{full}$  KIDs in theory, we can, as a rule of thumb, estimate the required time of integration required to reach a sensitivity  $\sigma_{target}$ . Let's call  $\eta = N_{valid}/N_{full}$  the fraction of valid KIDs of the matrix. To reach the same number of hits per map pixels, with the same scanning strategy, the total integration time must be  $1/\eta$  time larger, hence :

$$t_{astronomer} = \left( \frac{NEFD}{\sigma_{target}} \right)^2 \frac{1}{\eta} \quad (52)$$

### 10.1.2 Time of integration from the matrix footprint

One can also think of the “time spent on the source”, for a full matrix (ie. all valid KIDs), as the time when the source is inside the circular footprint of the matrix. During a scan, it's easy to count how much time the source is at a distance from the FOV center that is larger than the FOV radius. Let's call this time  $t_{geom}$ . However, because the map is produced with only a fraction  $\eta$  of valid KIDs, the effective integration time on the source is  $\eta$  times smaller than  $t_{geom}$ . Hence:

$$NEFD = \sigma \sqrt{t_{geom}\eta} \quad (53)$$

### 10.1.3 Time of integration from the flux estimator

The NEFD is defined as the noise “per beam”, the uncertainty on the estimation of the flux of a point source. The estimation of a point source flux is given by the fit of a gaussian profile, that in the case of white noise reduces to:

$$\hat{\phi} = \frac{1}{\sum_p g_p^2} \sum_p g_p m_p, \quad (54)$$

and whose variance is

$$\sigma_\phi^2 = \left( \frac{1}{\sum_p g_p^2} \right)^2 \sum_p g_p^2 \sigma_p^2. \quad (55)$$

In the case of white noise and considering the equivalent of the uniform full matrix of the NEFD definition:  $\sigma_p = \sigma / \sqrt{N_p}$ , where  $\sigma$  is the standard deviation of 1 sample and  $N_p$  is the number of hits in pixel  $p$ . Accounting for the sampling frequency, it reads

$$\begin{aligned} \sigma_\phi^2 &= \frac{\sigma}{v} \left( \frac{1}{\sum_p g_p^2} \right)^2 \sum_p \frac{g_p^2}{t_p}, \\ &= \frac{\sigma}{v} \frac{1}{t_{beam}} \end{aligned} \quad (56)$$

where  $t_{beam}$  is homogeneous to a time and is such that  $\sigma_\phi$  goes like  $1/\sqrt{t_{beam}}$ .

## 10.2 History and confusions

In the past few days, we have re-examined these definitions, and several mistakes were made:

- at some point, the `nk_map_photometry.pro` that is supposed to give the correct “time”, rather than giving  $t_{int}$  as defined in Eq. (49) was giving  $\eta t_{int}$ .
- When questioning this relation, we confused  $t_{int}$  and  $t_{obs} = t_{int}/\eta$ . While the dependence on the grid step and the map resolution was accounted for in average, it was not the correct time to consider to compute the NEFD as defined in the MoU (a.k.a detector NEFD, letting  $\eta$  as another parameter in IRAM’s time estimator).
- In the end, the final NEFD we must give to IRAM are those that we published but increased by a factor  $1/\sqrt{\eta}$ .

## 10.3 Data processing

The data were decorrelated using the common-monde-one-block method (cf. ??), masking a disk of 60 arcsec radius centered HLSJ0918+5142. The scans have been combined with standard inverse noise weighting. The noise in each map pixel is derived from the rms of the background corrected by the square root of the number of observations per pixel (N1). If the noise was perfectly gaussian, the distribution of the map signal over this noise estimate (far from the source) would be a normalized gaussian. In practice, this leads to gaussians that 1.6 and 1.5

larger. We therefore increase our noise estimate (N1) by these factors to derive our final estimates. Should the extra sources that pop up in the field contribute to this estimate, they would only make our estimate more conservative.

#### 10.4 NEFD Methods 1 and 2: deep integration

These data can be used to derive the NEFD in several ways. One is to fit the evolution of the uncertainty on the flux of the source  $\sigma_\phi$  with the integration time. Another one is to produce jackknife maps with the data and to measure the uncertainty on the flux in the end, while estimating the time of integration. Depending on what definition of the time of integration we take, we might get slightly varying answers, we'll come back to this later one. However, we must note right now that the assumption that the sensitivity should go like  $1/\sqrt{t}$  needs clarification. This can only be true if scans are co-added with equal noise weights and are observed under the same conditions of opacity and elevation. Otherwise, corrections must be taken into account. Indeed,

$$\sigma = NEFD_0 e^{\tau / \sin \delta} \sqrt{t} \quad (57)$$

and scans are coadded with inverse variance weighting, so the combined flux is:

$$\phi = \frac{1}{\sum_n 1/\sigma_n^2} \sum_n \frac{\phi_n}{\sigma_n^2} \quad (58)$$

whose variance is

$$\sigma^2 = \frac{1}{\sum_n 1/\sigma_n^2} \quad (59)$$

which, according to Eq. (57) becomes

$$\sigma^2 = \frac{NEFD_0^2}{\sum_n t_n e^{-2\tau_n / \sin \delta_n}}. \quad (60)$$

If the opacity and the elevations are the same for all scans, we recover the integration like  $\sqrt{t}$ . In general, if the observing conditions vary, we must fit the integrated sensitivity vs the effective time  $\sum_n t_n e^{-2\tau_n / \sin \delta_n}$  in order to recover an unbiased estimate of  $NEFD_0$ . Luckily enough, we have observations of Pluto in very stable atmospheric conditions and at quasi constant elevation. This will allow us to check this formalism against more intuitive and direct definitions. We can also extract from the scans on HLSJ0918+5142 those that were under stable opacity conditions and at high and quasi-constant elevation as a confirmation of our final estimates. The other regimes will help us derive uncertainties our estimates.

**Pluto.** We have 28 scans of Pluto, for a total integration time of XX at 1mm and XX at 2mm. Fig. 61 shows how the  $1\sigma$  sensitivity decreases with  $t_{int}$ . Considering the small variations of opacity and elevation during these observations of Pluto (Fig. 62), we can derive an average correction  $\exp(-\tau / \sin \delta) = \exp(-0.07 / \sin(30^\circ)) = 0.87$ . This leads to zenith  $NEFD_0^{1mm} = 38.8$  and  $NEFD_0^{2mm} = 9.2 \text{ mJy.s}^{-1/2}$ . Using the jackknife maps and applying the same opacity-elevation correction, one gets  $NEFD_0^{1mm} = 38.0$  and  $NEFD_0^{2mm} = 8.96$ .

$NEFD_0^{1mm}$ mJy.s $^{1/2}$	Pluto		HLS J0918+5142	
Red. method	CMB	CMB+poly5	CMB	CMB+poly5
$\sim 1/\sqrt{t}$	38.8	34.3	41.7	38.2
JK	35.9	<b>34.7</b>	33.8	<b>33.6</b>
$\sim 1/\sqrt{t_{eff}}$	38.5	<b>32.8</b>	37.5	<b>34.4</b>

Table 17: Zenith NEFD's in stable elevation and atmospheric conditions on Pluto and HLS J0918+5142 at 1mm.

$NEFD_0^{2mm}$ mJy.s $^{1/2}$	Pluto		HLS J0918+5142	
Red. method	CMB	CMB+poly5	CMB	CMB+poly5
$\sim 1/\sqrt{t}$	9.3	8.0	9.8	8.5
JK	8.8	<b>7.7</b>	8.3	<b>7.6</b>
$\sim 1/\sqrt{t_{eff}}$	9.2	<b>8.2</b>	9.4	<b>8.2</b>

Table 18: Zenith NEFD's in stable elevation and atmospheric conditions on Pluto and HLS J0918+5142 at 2mm.

In light what is discussed in the previous paragraph, if we fit the sensitivity vs  $\sum_n t_n e^{-2\tau_n / \sin \delta_n}$ , we obtain  $NEFD_0^{1mm} = 38.5$  and  $NEFD_0^{2mm} = 9.2$ . These value are summarized in tables 17 and 18. All these numbers are obtained with the standard reduction method, a. k. a. `common_mode_one_block`, (CMB). If we further subtract a polynomial of order 5 per subscan after this decorrelation (still masking the source), we improve the results as reported in the tables, while not changing the measured fluxes of Pluto and HLS (tab. 19). We therefore do not change the calibration with this extra filtering, so the gain in sensitivity does come from better noise subtraction.

**HLS J0918+5142.** While we have an overall longer integration on HLS J0918+5142, it was acquired during distinct periods, over varying elevation and different (albeit almost constant by plateau) opacities (Fig. ??). Still, performing the same analyses, we obtains the results presented in tables 17 and 18. The values obtained from the fit vs  $1/\sqrt{t}$  are recalled to illustrate the impact of the opacity-elevation correction on this estimator on HLS J0918+5142 data. One should focus on the values derived from the Jackknife maps and thoses including the opacity-elevation correction  $1/\sqrt{t_{eff}}$ : these values are in very good agreement when derived from the same reduction method, and in good agreement between Pluto and HLS J0918+5142.

**Conclusion:** while uncertainties on these values should be further investigated, the good agreement between alternative estimates and at the same time their differences indicate that they should be valid at about  $\pm 1$  mJy.s $^{1/2}$ . **With these two estimators (fit vs time of integration and Jackknife), we find zenith NEFDs below 35 and 9 mJy.s $^{1/2}$  at 1 and 2 mm respectively.** While less intuitive, the more rigourous definition of the integration time that enters the estimation of the flux,  $t_{beam}$ , leads to slightly different values. It improves by 5% at 1 mm, i.e. puts the upper limit at 33.4, but degrades the 2 mm value by the same amount and raise the upper limit to 9.3.

Fluxes (mJy)	Pluto		HLS J0918+5142	
Red. method	CMB	CMB+poly5	CMB	CMB+poly5
1 mm	$15.0 \pm 1.1$	$13.6 \pm 0.9$	$85.2 \pm 0.4$	$85.4 \pm 0.4$
2 mm	$5.0 \pm 0.2$	$5.0 \pm 0.2$	$14.9 \pm 0.1$	$14.9 \pm 0.1$

Table 19: Measured fluxes of Pluto and HLS J0918+5142 with two data reduction methods. The extra subtraction of polynomial of order 5 per subscan while masking the source does not subtract power to the source, hence the derived sensitivities with this methods do not need to be recalibrated.

## 11 Total effective error budget

We here list the main sources of uncertainties (other than pure noise) on our flux measurements and estimate their respective values. We model them as a sum of quadratures:

$$\sigma_{\text{syst}}^2 = (k_{NL} + k_{beam} + k_{cc} + k_{\tau})\phi^2 \quad (61)$$

We first summarize the meaning and typical values of these terms, then detail the derivations in the following subsections when needed.

- $k_{NL}$ . This term accounts for the Non-Linearity of the detector response. When the incoming flux is too high, the detector responds in a non linear way. On the brightest sources such as Mars (several hundreds of Jy), we have seen biased estimations of the flux by  $\Delta\phi/\phi$  of a few %. We'll thus take  $k_{NL} = 10^{-4}$ .
- $k_{beam}$ . Anomalous refraction and focus imperfections act together to broaden the nominal resolution into an effective  $FWHM_1 \simeq 2.35\sigma_1$  while we perform photometry with a fixed  $FWHM \simeq 2.35\sigma$ . For standard observing conditions and uncertainties, this term is about  $4 \times 10^{-3}$  (see sect. 11.1).
- $k_{\tau}$ . Imperfect knowledge of the opacity induces errors on the flux measurement. Typically, this term reaches 1% (see sect. 11.2).
- $k_{cc}$ . Accounts for the error induced when we perform color corrections. XXX TBD XXX

### 11.1 Systematic impact of effective beam corrections

If  $m$  is the signal map and  $g$  is a gaussian weight (of width  $\sigma$ ), then our flux estimate is equivalent to

$$\phi_{\text{est}} = \frac{1}{\sum_i g_i^2} \sum_i g_i m_i \quad (62)$$

Indeed, in the case of a point source and no error on the FWHM,  $m_i = \phi g_i = \phi e^{-x_i^2/2\sigma^2}$ . Now, accounting for the effective  $\sigma_1$ , our estimate becomes

$$\begin{aligned} \phi_{\text{est}} &= \frac{1}{\sum_i g_i^2} \sum_i m_i e^{-x_i^2/2\sigma^2} \\ &= \frac{1}{\sum_i g_i^2} \sum_i \phi e^{-x_i^2/2\sigma_1^2} e^{-x_i^2/2\sigma^2}, \end{aligned}$$

$$= \phi \frac{1}{\sum_i g_i^2} \sum_i e^{-\frac{x_i^2}{2} \frac{\sigma^2 + \sigma_1^2}{\sigma_1^2 \sigma^2}}, \quad (63)$$

We thus adapt our flux estimator like so:

$$\phi'_{est} = \phi_{est} \frac{\sum_i g_i^2}{\sum_i e^{-\frac{x_i^2}{2} \frac{\sigma^2 + \sigma_1^2}{\sigma_1^2 \sigma^2}}} \quad (64)$$

However, our estimate of  $\sigma_1$  suffers from uncertainties. Let's call  $\sigma_2 = \sigma_1 + \delta$  our estimate of  $\sigma_1$ , we thus have

$$\begin{aligned} \phi'_{est} &= \phi_{est} \frac{\sum_i g_i^2}{\sum_i e^{-\frac{x_i^2}{2} \frac{\sigma^2 + \sigma_2^2}{\sigma_2^2 \sigma^2}}} \\ &= \phi \frac{\sum_i e^{-\frac{x_i^2}{2} \frac{\sigma^2 + \sigma_1^2}{\sigma_1^2 \sigma^2}}}{\sum_i e^{-\frac{x_i^2}{2} \frac{\sigma^2 + \sigma_2^2}{\sigma_2^2 \sigma^2}}} \\ &= \phi \frac{2\pi\sigma^2\sigma_1^2}{\sigma^2 + \sigma_1^2} \frac{\sigma^2 + \sigma_2^2}{2\pi\sigma^2\sigma_2^2} \\ &\approx \phi \frac{\sigma^2\sigma_1^2(\sigma^2 + \sigma_1^2 + 2\delta\sigma_1 + \delta^2)}{\sigma^2\sigma_1^2(\sigma^2 + \sigma_1^2)(1 + 2\delta/\sigma_1 + \delta^2/\sigma_1^2)} \\ &\approx \phi \frac{\sigma^2 + \sigma_1^2 + 2\delta\sigma_1}{\sigma^2 + \sigma_1^2} (1 - 2\delta/\sigma_1) \\ &\approx \phi \frac{2\delta}{\sigma_1} \frac{\sigma^2}{\sigma_1^2 + \sigma^2} \end{aligned} \quad (65)$$

## 11.2 Systematic impact of opacity correction

The derivation of opacity comes from the monitoring of the KID frequency vs air mass:

$$f = C_0 + T_0 C_1 (1 - e^{\tau / \sin \delta}) \quad (66)$$

where  $\delta$  is the elevation,  $T_0$  is the atmosphere equivalent temperature and  $C_0$  and  $C_1$  the KIDs' coefficients that are determined via skydips. In the following, we neglect any uncertainty on the elevation and on  $f$ . Let's parameterize the errors on the KIDs' coefficients like  $\hat{C}_0 = C_0(1 + \alpha)$  and  $\hat{C}_1 = C_1(1 + \beta)$ . From eq. (66), we thus derive an approximate opacity:

$$\begin{aligned} \hat{\tau} &= \sin \delta \ln \left( 1 - \frac{f - \hat{C}_0}{T_0 \hat{C}_1} \right) \\ &= \sin \delta \ln \left( 1 - \frac{f - C_0(1 + \alpha)}{T_0 C_1(1 + \beta)} \right) \\ &\approx \sin \delta \ln \left( 1 - \frac{f - C_0(1 + \alpha)}{T_0 C_1} (1 - \beta) \right) \end{aligned}$$

$$\begin{aligned}
&\simeq \sin \delta \ln \left( 1 - \frac{f - C_0}{T_0 C_1} + \frac{\alpha C_0}{T_0 C_1} + \beta \frac{f - C_0}{T_0 C_1} \right) \\
&\simeq \sin \delta \ln \left( \frac{T_0 C_1 - f + C_0}{T_0 C_1} \left( 1 + \frac{\alpha C_0}{T_0 C_1 - f + C_0} + \frac{\beta(f - C_0)}{T_0 C_1 - f + C_0} \right) \right)
\end{aligned}$$

Now, given that  $C_0$  and  $f$  are about  $10^9$  whereas  $T_0 = 270$  and  $C_1$  is about  $10^3$ , the previous relation is approximately

$$\begin{aligned}
\hat{\tau} &\simeq \sin \delta \ln \left( \frac{T_0 C_1 - f + C_0}{T_0 C_1} (1 + \alpha + \beta) \right) \\
&\simeq \tau + \sin \delta \ln(1 + \alpha + \beta) \\
&\simeq \tau + \sin \delta \left( (\alpha + \beta) - \frac{(\alpha + \beta)^2}{2} + \frac{(\alpha + \beta)^3}{3} \right)
\end{aligned} \tag{67}$$

So, when we correct the estimated flux by  $e^{\tau / \sin \delta}$ , this leads to

$$\begin{aligned}
\hat{\phi} &= \phi_{measured} e^{\hat{\tau} / \sin \delta} \\
&= \phi e^{-\tau / \sin \delta} e^{\hat{\tau} / \sin \delta} \\
&\simeq \phi e^{\alpha + \beta - \frac{(\alpha + \beta)^2}{2}} \\
&\simeq \phi \left( 1 + \alpha + \beta - \frac{(\alpha + \beta)^2}{2} \right)
\end{aligned}$$

so

$$\Delta \phi / \phi = (\alpha + \beta) - \frac{(\alpha + \beta)^2}{2} \tag{68}$$

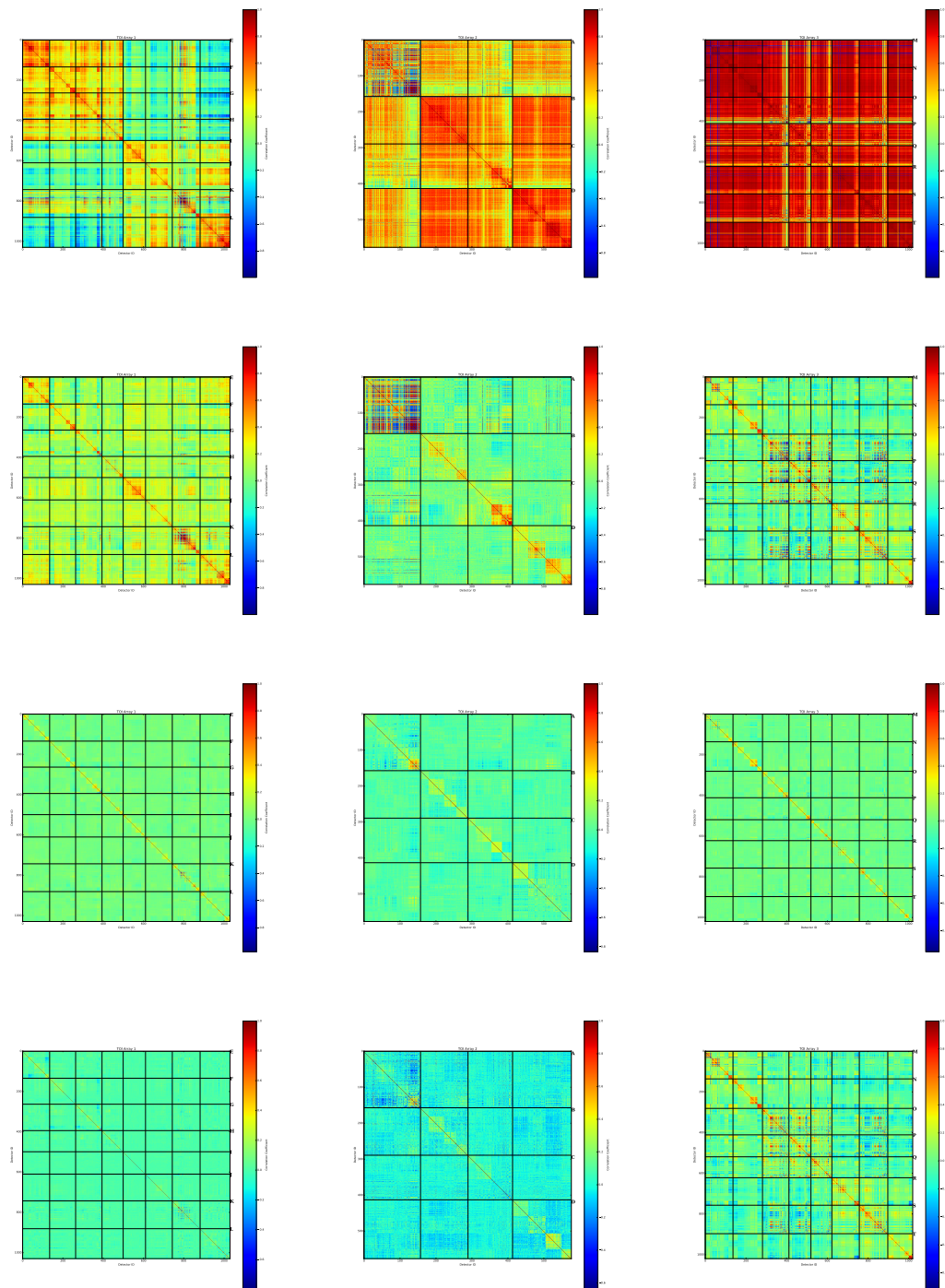


Figure 52: From left to right correlation matrices for the three NIKA2 arrays (A1, A2, and A3) for scan 20161211s299. From top to bottom we present the correlation of the raw data, after CM, PCA and BC decorrelations.

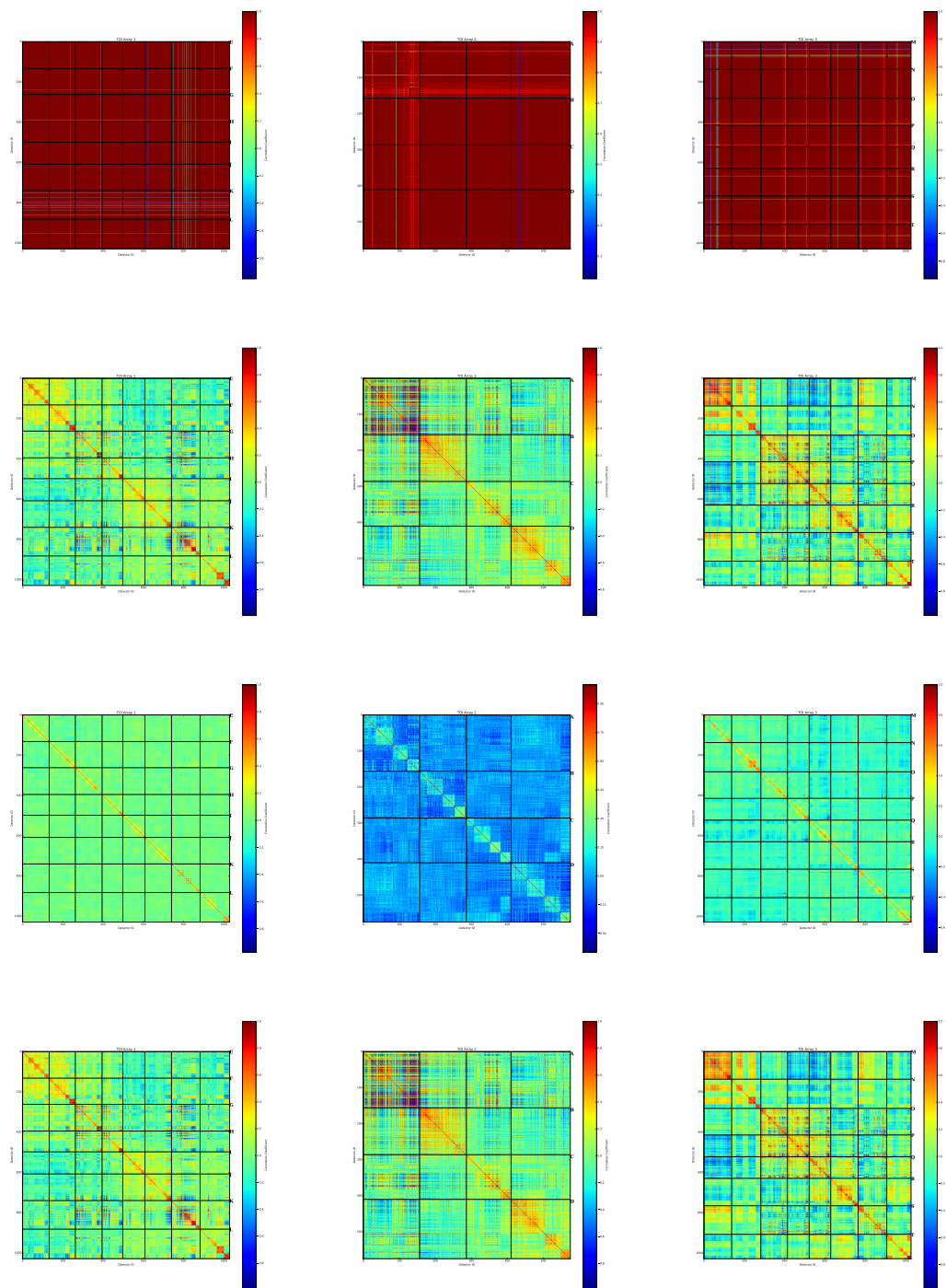


Figure 53: From left to right correlation matrices for the three NIKA2 arrays (A1, A2, and A3) for scan 20161213s72. From top to bottom we present the correlation of the raw data, after CM, PCA and BC decorrelations.

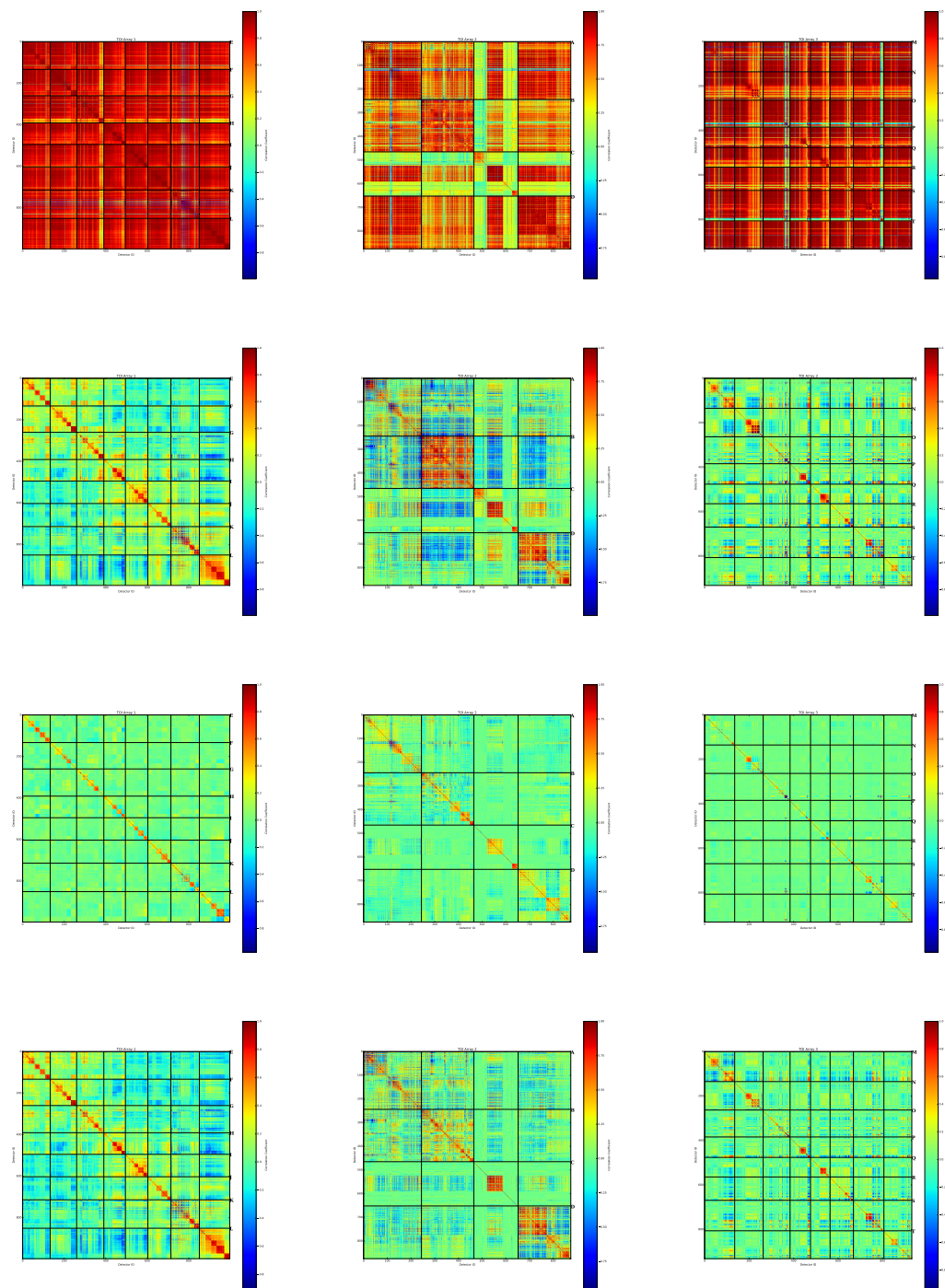


Figure 54: From left to right correlation matrices for the three NIKA2 arrays (A1, A2, and A3) for scan 20160504s97. From top to bottom we present the correlation of the raw data, after CM, PCA and BC decorrelations.

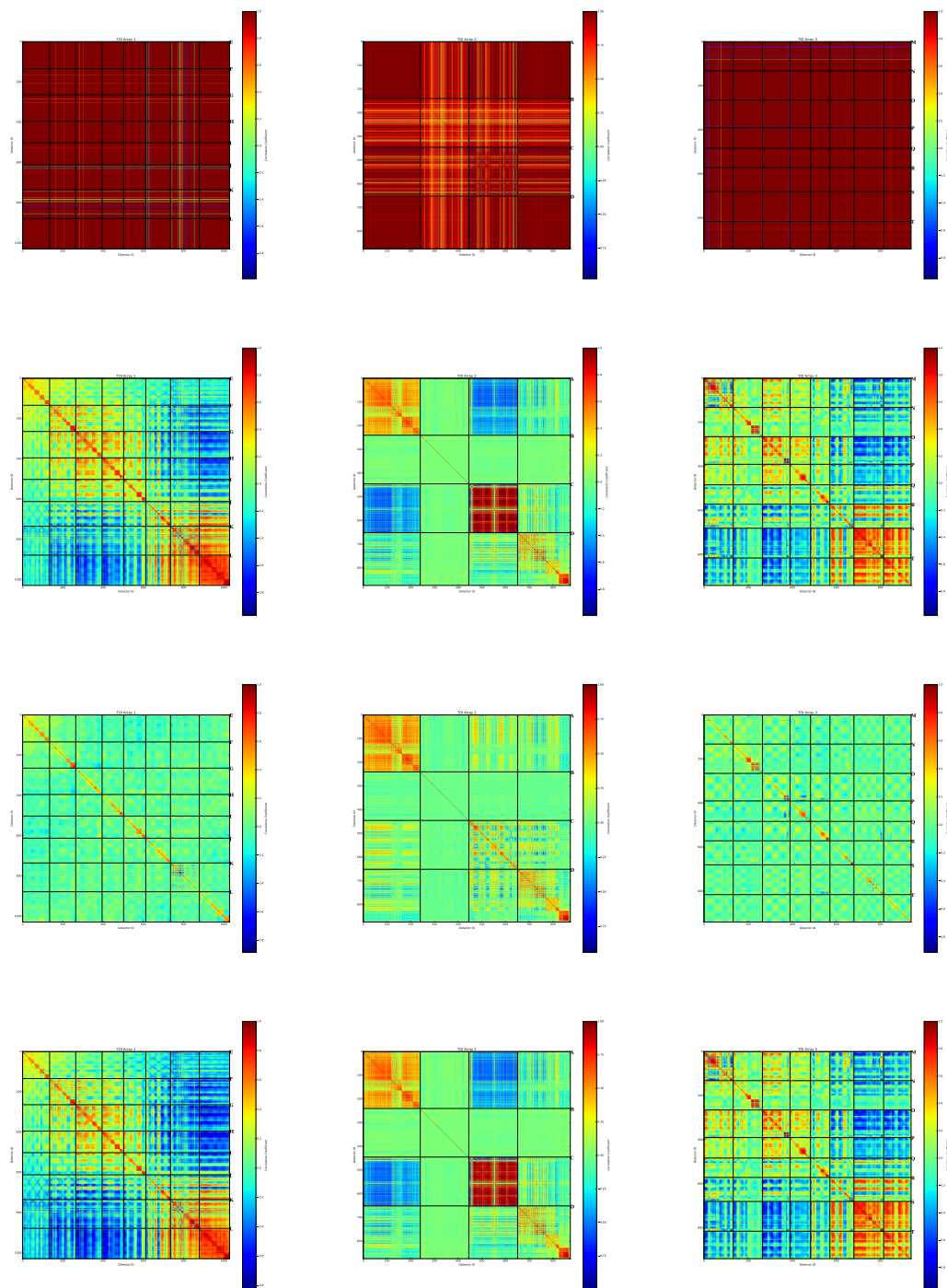


Figure 55: From left to right correlation matrices for the three NIKA2 arrays (A1, A2, and A3) for scan 20160313s87. From top to bottom we present the correlation of the raw data, after CM, PCA and BC decorrelations.

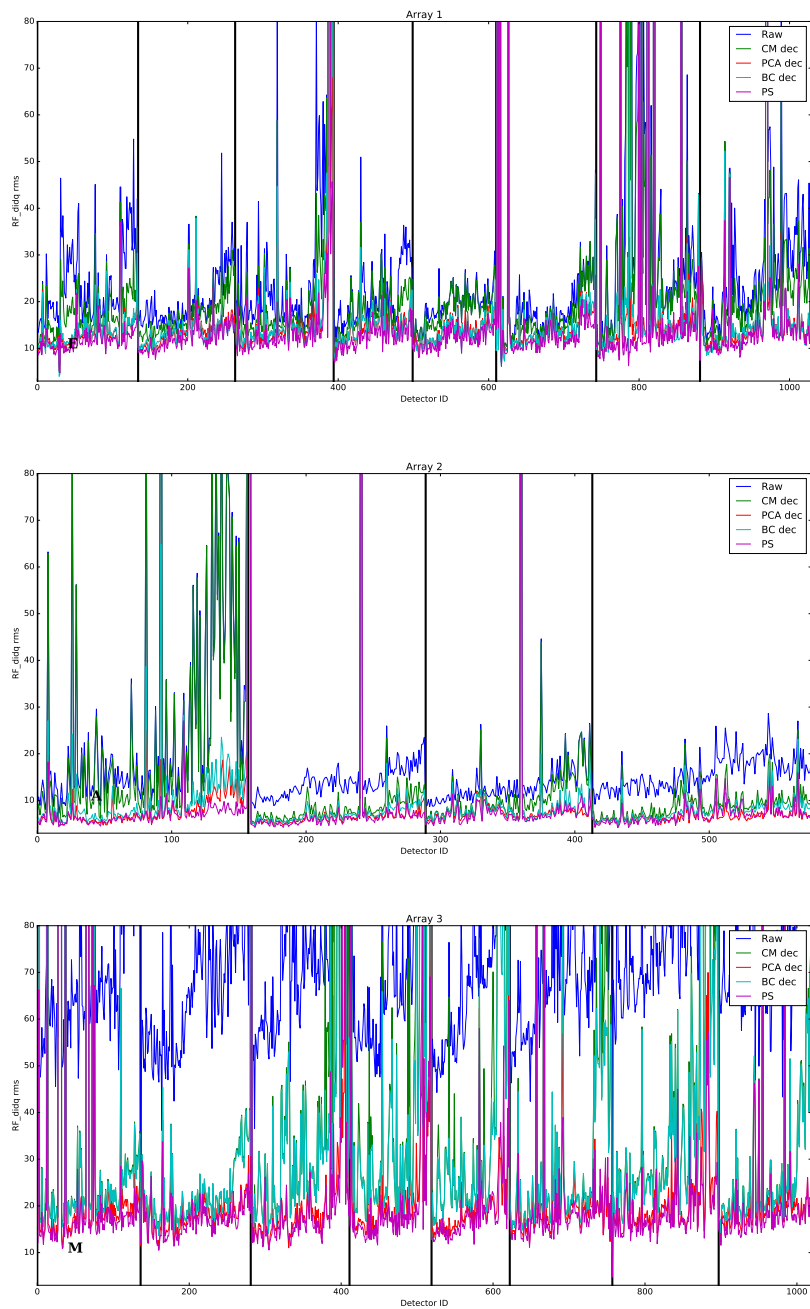


Figure 56: RMS noise for arrays 1,2, and 3 (top to bottom) for scan 20161211s299. The rms is computed for the raw data, and for the three decorrelation methods, CM, PCA and BC. The rms value for the level of white is also computed from the raw data power spectrum (PS).

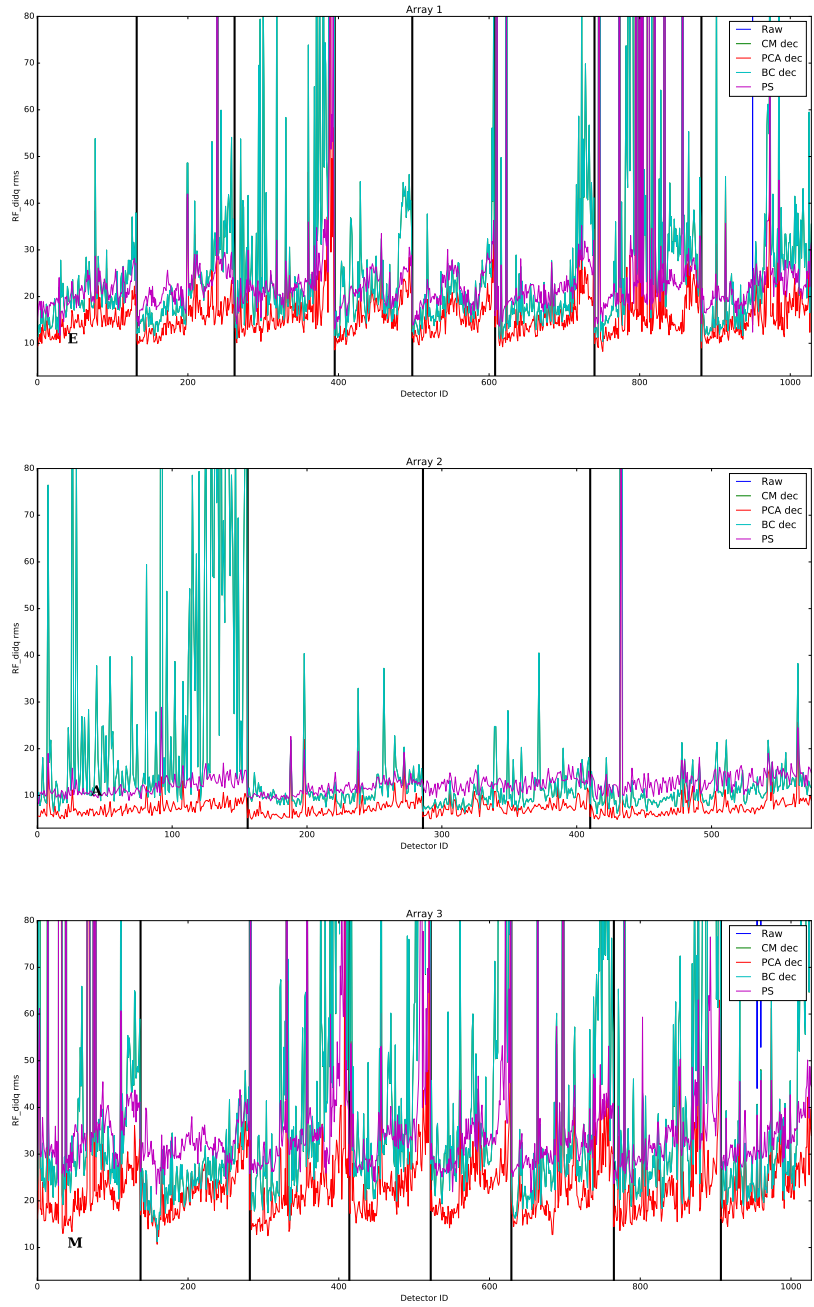


Figure 57: Same as Figure 56 but for scan 20161213s72.

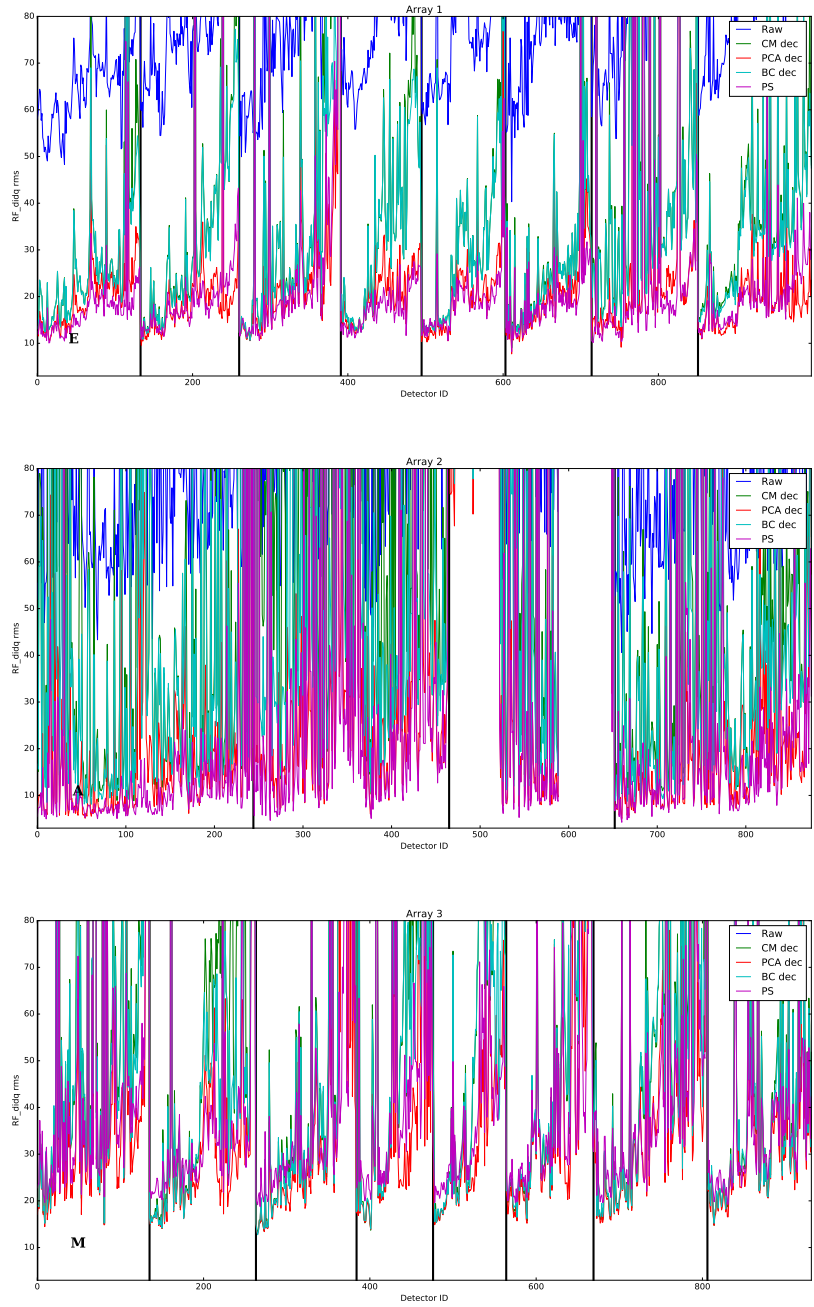


Figure 58: Same as Figure 56 but for scan 20160504s97.

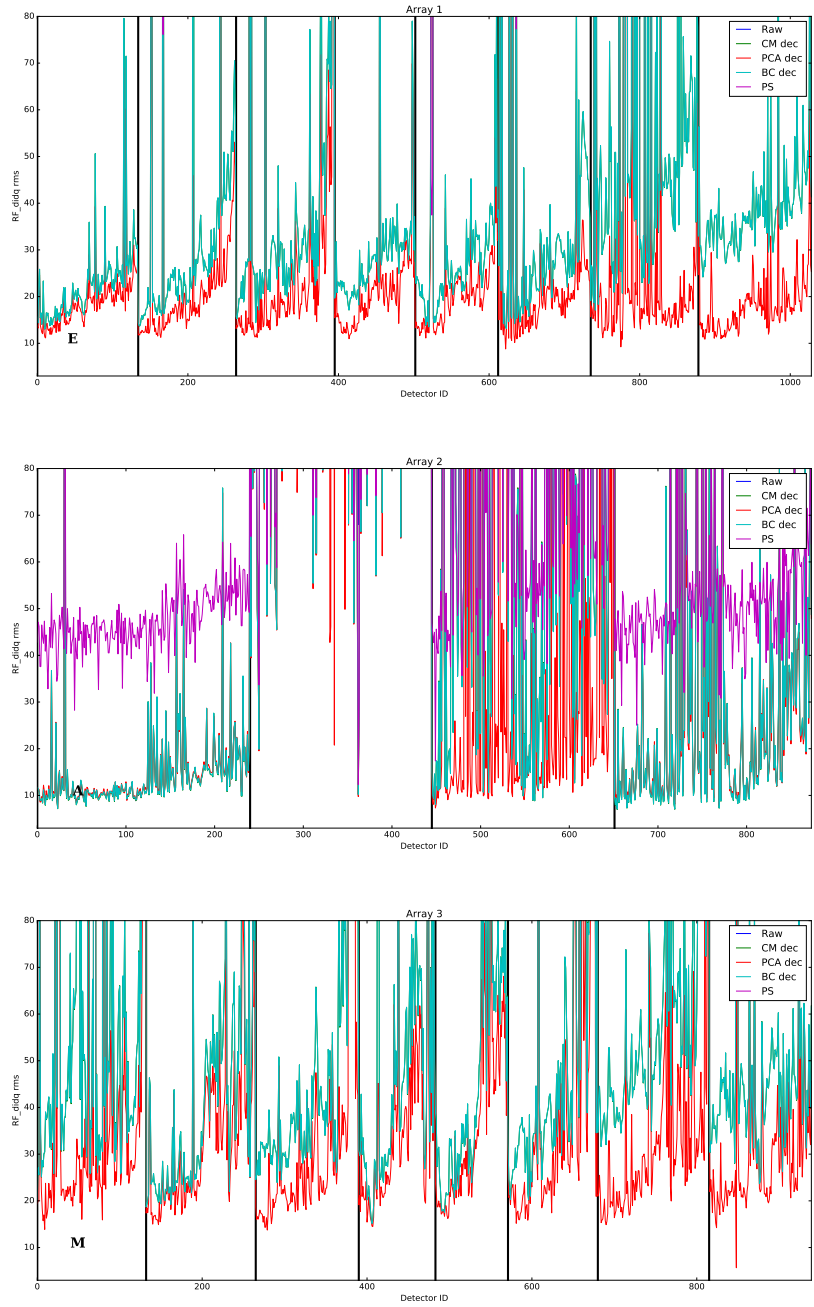


Figure 59: Same as Figure 56 but for scan 20160313s87.

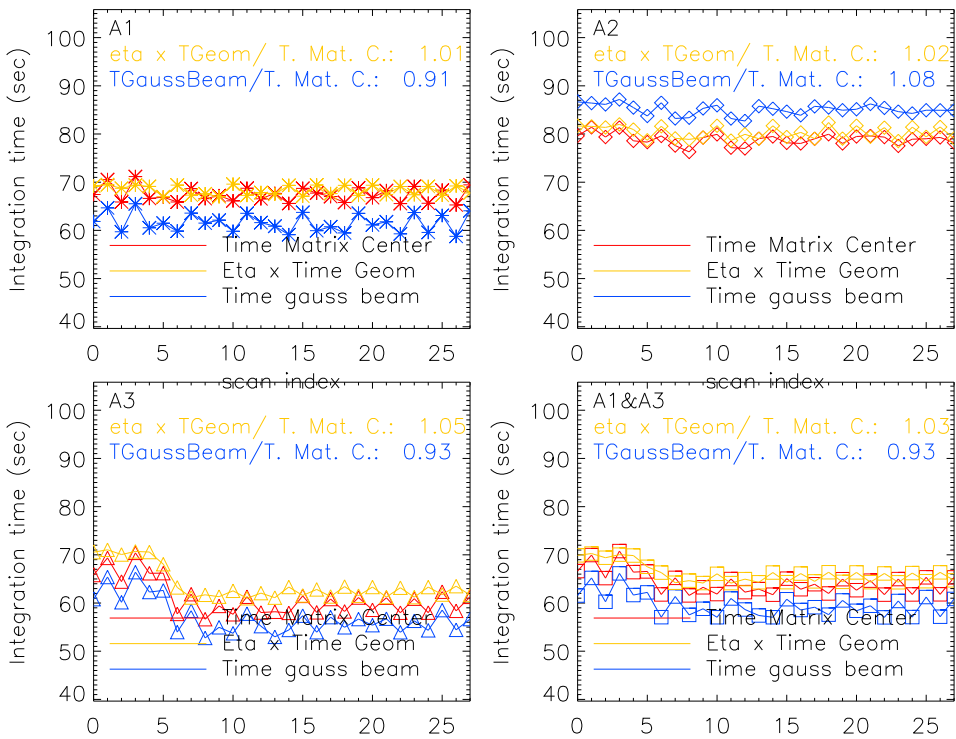


Figure 60: Comparison between three estimators of the time of integration on the source during Pluto's observation (Run9). To a few percent, the 3 estimators give compatible estimations.

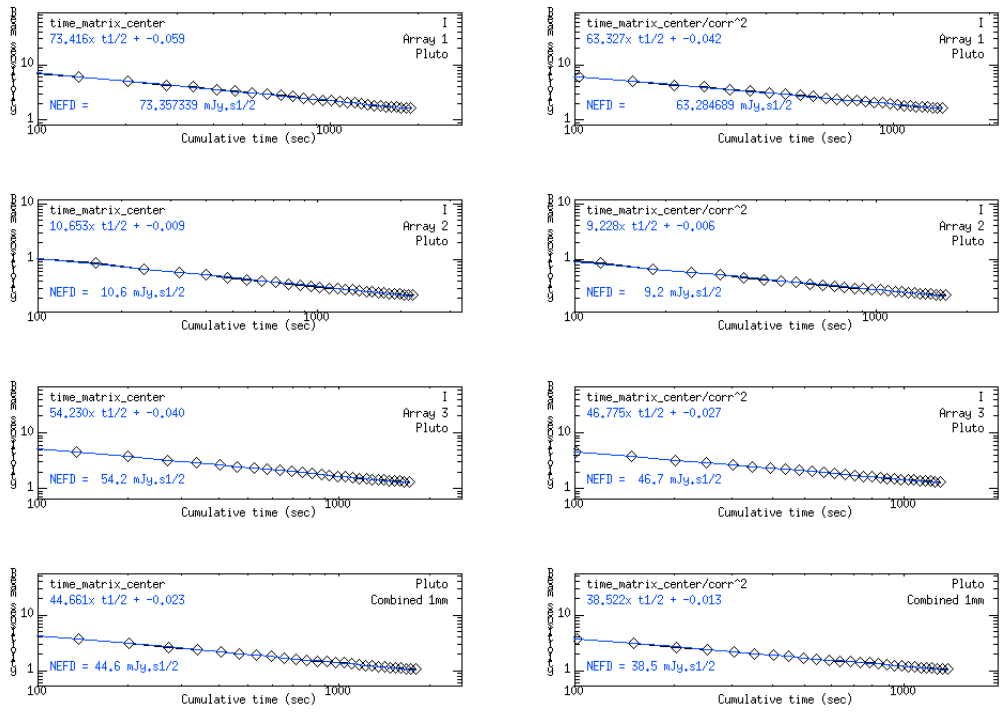


Figure 61: *Left:*  $1\sigma$  sensitivity vs  $t_{int}$  during observations of Pluto, **without correction for elevation or opacity**. *Right:* Same fit but this time considering the effective time, weighted by opacity and elevation as in Eq. (60).

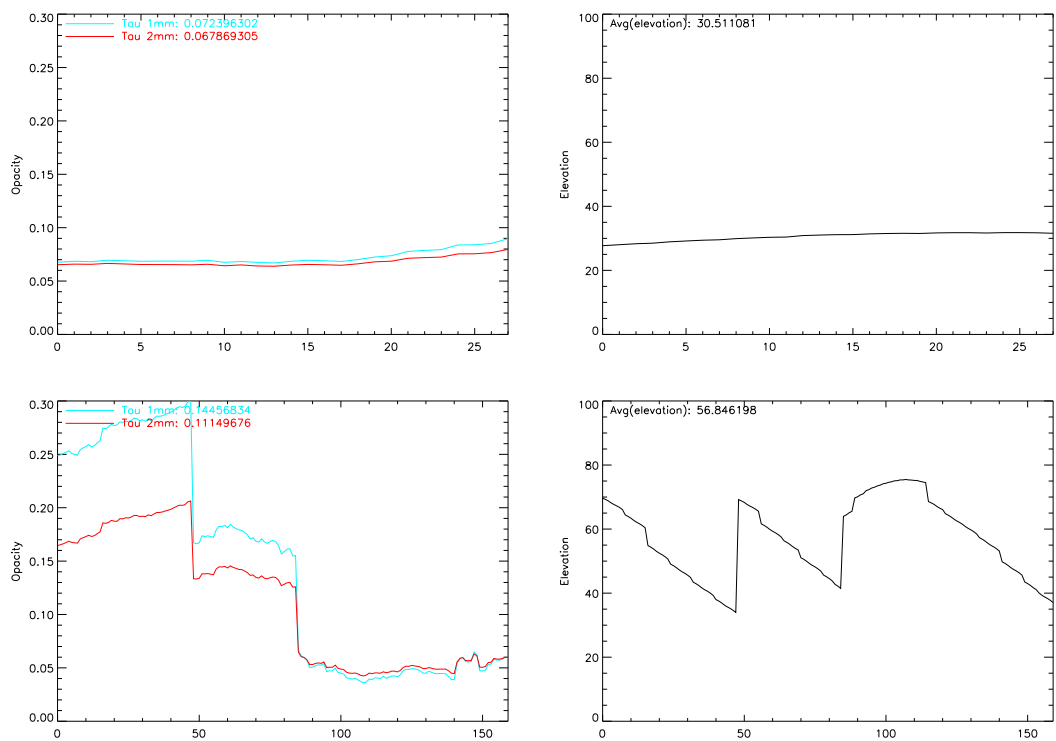


Figure 62: Opacities and elevations during observations of Pluto and HLS J0918+5142. While conditions were stable both in opacity and elevation for Pluto, it was not the case for HLS J0918+5142.

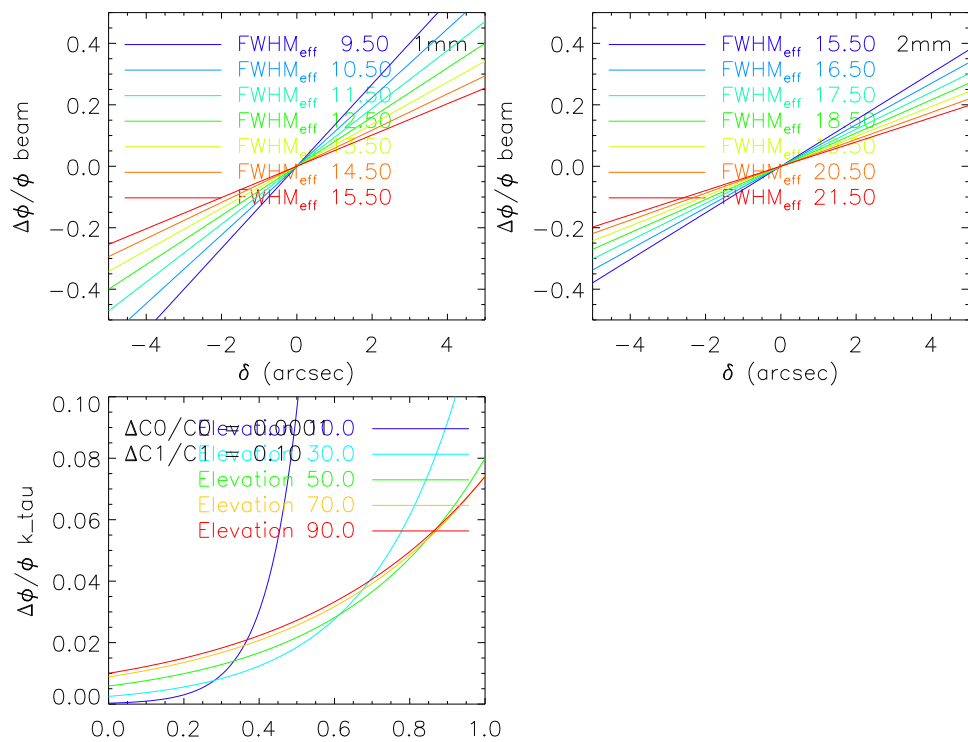


Figure 63: Top: Systematic error induced by anomalous refraction and imperfect focus at 1 and 2 mm. Bottom: systematic error induced by opacity correction.

## 12 Summary of performance

The main measured parameters that define the actual NIKA2 performances are gathered in Table ??.

	Array 1	Array 3	Array 1&3	Array 2
Reference Wavelength [mm]	1.2	1.2	1.2	2.0
Reference Frequency [GHz]	260	260	260	150
Central Frequency [GHz]	255.5	257.8		151.6
Bandwidth [GHz]	47.8	45.7		42.1
Number of designed detectors	1140	1140		616
Number of valid detectors	952	961		553
Fraction of valid detectors [%]				
Effective FOV <sup>a</sup> [arcmin]	5.39	5.61		4.9
Pixel size in beam sampling unit [F $\lambda$ ]				
FWHM <sup>b</sup> [arcsec]	$11.3 \pm 0.2$	$11.2 \pm 0.2$	$11.2 \pm 0.1$	$17.7 \pm 0.1$
Beam efficiency <sup>c</sup> [%]				
rms of the FWHM on the FOV [%]				
rms calibration error [%]	4.5	6.6		5
Absolute calibration uncertainty [%]			5	
$\alpha$ noise integration in time <sup>d</sup>				
rms pointing error [arcsec]			< 3	
NEFD <sup>e</sup> [mJy · s <sup>1/2</sup> /beam]	30 (15)	30 (15)	30 (15)	20 (10)
Mapping speed <sup>f</sup> [arcmin <sup>2</sup> /h/mJy <sup>2</sup> ]	302	454	775 (1184)	7542 (10861)

(a) Equivalent FOV covered by the valid detectors

(b) Full-width at half-maximum of the main beam modelled as a two-dimensional Gaussian fitted from sidelobe-masked beam maps.

(c) Ratio between the main beam power and the total beam power up to a radius of XXX arcsec

(d) Effective power law of noise reduction with integration time

(e) NEFD in typical IRAM good sky opacity condition: 2mm pwv, 60° elevation

(f) Average (best) mapping speed at zero opacity for the February 2017 observation campaign.

Table 20: Summary of the main characteristics describing the measured performances of NIKA2.  
**FM : 260 GHz is 1.15 mm.**

The performance parameters given in Table ?? are splitted in two different lists: first, the main characteristics, as defined in the MOU, are listed in Table 21, second, other parameters, which are derived from the instrument characteristics described in the MOU, and that need to be characterized to complete the commissioning phase are given in Table 22. Table 22 is constructed from the ‘secondary’ and ‘tertiary’ tables of Samuel’s summary document.

Table 21: Summary of the main characteristics describing the measured performances of NIKA2, as listed in MoU

	Array 1	Array 3	Array 1&3	Array 2
NEFD <sup>a</sup> [mJy · s <sup>1/2</sup> /beam]	30 (15)	30 (15)	30 (15)	20 (10)
Number of designed detectors	1140	1140		616
Number of valid detectors	952	961		553
Fraction of valid detectors [%]				
FWHM <sup>b</sup> [arcsec]	11.3 ± 0.2	11.2 ± 0.2	11.2 ± 0.1	17.7 ± 0.1
Effective FOV <sup>c</sup> [arcmin]	5.39	5.61		4.9
Pixel size in beam sampling unit [F $\lambda$ ]				

(a) NEFD in typical IRAM good sky opacity condition: 2mm pwv, 60° elevation

(b) Full-width at half-maximum of the main beam modelled as a two-dimensional Gaussian fitted from sidelobe-masked beam maps.

(c) Equivalent FOV covered by the valid detectors

Table 22: Summary of other NIKA2 performance characteristics either defined in the MoU or extracted from SL's summary document

	Array 1	Array 3	Array 1&3	Array 2
Reference Wavelength [mm]	1.2	1.2	1.2	2.0
Reference Frequency [GHz]	260	260	260	150
Central Frequency [GHz]	255.5	257.8		151.6
Bandwidth [GHz]	47.8	45.7		42.1
Beam efficiency <sup>a</sup> [% ]				
rms of the FWHM on the FOV [%]				
rms calibration error [%]	4.5	6.6		5
Absolute calibration uncertainty [%]			5	
$\alpha$ noise integration in time <sup>d</sup>				
rms pointing error [arcsec]			< 3	
Mapping speed <sup>b</sup> [arcmin <sup>2</sup> /h/mJy <sup>2</sup> ]	302	454	775 (1184)	7542 (10861)

(a) Ratio between the main beam power and the total beam power up to a radius of XXX arcsec

(b) Average (best) mapping speed at zero opacity for the February 2017 observation campaign.

## A Synchronization with the telescope

**NIKA2 synchronization scheme** NIKA2 reference clock is the *pulse per second* (pps) [TO BE DEVELOPED A BIT]

**Synchronization between instrument and scan information** A list of network specifications has been provided to IRAM by the NIKA2 consortium. A thorough characterization of the delay in receiving the telescope messages will be led by Francesco P.

**Synchronization between instrument and telescope coordinates** Albrecht S. to lead the characterization.

A final characterization of the accuracy of the dating of each sample will be undergone using zigzag scans acquired in excellent weather conditions.

## B Reference to technical documentation

This paragraph reviews the status of the technical documentation that should be delivered to the collaboration by the NIKA2 consortium and the IRAM, as defined in the MOU.

### B.1 Consortium-lead documentation

- Plan of the cryostat: 3D model (e.g. STEP, Solid Works, etc.) and plans as built (e.g. PDF)
- List of hardware components (per module)
- Optics filtering components. [Consortium].
- Cryogenics system characteristics with basic and standard operating procedures (see section 6.3).
- Cryogenics monitoring and diagnostic tools plus procedure to contact a cryogenist from the consortium who is mandated to help IRAM in case of problem with the cryostat.
- Electronics cards characteristics, implantation plans, and operating procedures.
- Programmable electronics.
- Network needs (architecture, data rates, speed, memory, synchronization accuracy, internet access, storage, backup, archiving, etc).
- Software for instrument control and data acquisition (Camadria), aimed at general users.

### B.2 IRAM-lead documentation

- Optics imaging system characteristics and calculations
- Observers interface: PaKo functions specific to NIKA2, plus useful scripts
- Automated on line data processing tools. [IRAM lead, consortium input].
- Off line data processing software. [IRAM lead, consortium input].

- Cook book (for external users: including a short description of NIKA2 setup, check list and procedure to use the instrument at the telescope). Can be provided at the end of instrument commissioning. [IRAM, consortium input].

## References

- [1] Petit J., Bardeau S., Reynier E., "Comparison of ATM versions: Impact on the calibration of IRAM instruments", IRAM memo 2009-5, <http://www.iram-institute.org/EN/content-page-161-7-66-161-0-0.html>
- [Pardo et al. 2002] Pardo, J. R., Cernicharo, J. & Serabyn, E., 2002, IEEE Transactions on Antennas and Propagation 49, 1683
- [2] (Dempsey et al 2013)
- [3] (Knapp et al 1994)
- [4] (Tafoya et al 2004)
- [5] <http://www.lesia.obspm.fr/perso/emmanuel-lellouch/mars/index.php>
- [6] [https://github.com/haussel/photometry/blob/master/notebooks/planet\\_fluxes.ipynb](https://github.com/haussel/photometry/blob/master/notebooks/planet_fluxes.ipynb)
- [7] (Planck intermediate results LII, Planck Collaboration in press)
- [8] [https://github.com/haussel/photometry.](https://github.com/haussel/photometry)
- [9] <https://ssd.jpl.nasa.gov/horizons.cgi>
- [10] <https://www.cosmos.esa.int/web/herschel/calibrator-models>
- [11] M. Krips, talk at the 8th IRAM Millimeter Interferometry School, Grenoble (France), October 2012, and privae communication.  
<http://www.iram.fr/IRAMFR/IS/IS2012/presentations/krips-fluxcalibration.pdf>
- [12] M.G. Hoare, et al., 1992, MNRAS, 258, 257
- [13] Durand's PhD Thesis at Université Grenoble Alpes, 2008
- [14] M. Calvo *et al.*, Journal of Low Temperature Physics 184 (2016) 816-823
- [15] R. Adam *et al.*, arXiv:1707.00908
- [16] A. Monfardini *et al.*, The Astrophysical Journal Supplement 194 (2011) 24
- [17] O. Bourrion *et al.*, JINST 11 (2016) P11001
- [18] M. Calvo *et al.*, Astron. Astrophys. 551 (2013) L12
- [19] A. Monfardini *et al.*, JLTP 176 (2014) 787
- [20] A. Catalano *et al.*, Astron. Astrophys. 569 (2014) A9.
- [21] Combes F. et al., A&A 538, 4, 2012
- [22] A. Ritacco *et al.*, Astron. Astrophys. 599 (2017) A34
- [23] A. Bracco *et al.*, Astron. Astrophys. 604 (2017) A52
- [24] R. Adam *et al.*, Astron. Astrophys. 569 (2014) A66
- [25] R. Adam *et al.*, Astron. Astrophys. 576 (2015) A12
- [26] R. Adam *et al.*, Astron. Astrophys. 586 (2016) A122
- [27] R. Adam *et al.*, Astron. Astrophys. 598 (2017) A115
- [28] F. Ruppin *et al.*, Astron. Astrophys. 597 (2017) A110

- [29] R. Adam *et al.*, arXiv:1706.10230 [astro-ph.CO].
- [30] C. Romero *et al.*, arXiv:1707.06113 [astro-ph.CO].
- [31] B. Comis *et al.*, arXiv:1605.09549 [astro-ph.CO].